Doctoral Dissertation (Shinshu University)

Study of Sb doped SnS thin film and its heterojunctions

Sb 添加 SnS 薄膜及びそのヘテロ接合に関する研究

Graduate school of Medicine, Science, and Technology

Department of Science and Technology

Division of Energy and Systems Engineering

Ashenafi Abadi Elyas

March 2022

Acknowledgments

Completing my thesis amidst the pandemic and the ongoing war back home in Tigray, Ethiopia, was very challenging. It was a collective effort of many remarkable individuals who I wish to acknowledge here.

First and foremost, I am incredibly grateful to my supervisors, Dr. Myo Than Htay and Prof. Yoshio Hashimoto, for their invaluable advice, continuous support, and patience during my Ph.D. study. I am very grateful for their constant encouragement, insightful discussions, and immeasurable support ever since I joined the research team as an MSc student 5+ years ago. Their understanding and help, especially in the challenging and traumatic past year, were beyond what my words could express here. I also would like to thank and appreciate members of my Ph.D. examination committee, Prof. Toshinori Taishi and Dr. Shaibal Mukherjee (Indian Institute of Technology-IIT), for their invaluable inputs to shape my work & make the dissertation better.

I am grateful to Prof. Kentaro Ito and Dr. Noritaka Momose for their support during my study. I am also thankful to Dr. Noriyuki Urakami and all other members of Shinshu University. Their kind help and support have made my study and life in Japan a wonderful time.

I wish to thank my colleagues in the laboratory for a cherished time spent together in the lab and social settings. I also would like to thank Mr. Isamu Minemura for his assistance in glassworks, maintenance of laboratory equipment, and other technical matters.

A special thanks go to the Japanese government (Monbukagakusho - MEXT) for granting me a full scholarship during my period of study.

Finally, I would like to express my gratitude to my family and my wife (Mulu Assefa) for encouraging and supporting me throughout my life/study period and being a constant presence during my many times of stress, excitement, frustration, and celebration. Without their tremendous understanding and encouragement in the past few years, it would be impossible to complete my study.

Abstract

SnS is a binary compound semiconductor material with suitable optical properties which can be applied as absorber material of thin-film solar cells. However, SnS-based heterojunction solar cells have achieved efficiency lower than 5%. This could be due to the formations of secondary phases or lack of proper band alignment at the SnS/buffer heterojunctions. This research aims to study the effect of Sb doping and post-annealing treatments on the material properties of the SnS absorber layer and its SnS/CdS heterojunction. The SnS thin film was prepared by closed-tube sulfurization of RF-sputtered Sn precursor at 200 - 400 ˚C. Sb doping was conducted by thermal diffusion method where SnS was heated at Sb ambience at different temperatures. The vacuum annealing of the as-grown SnS thin films was carried out in the evacuated and sealed ampoule. Post-air-annealing (vacuum annealing followed by air annealing) was conducted under atmospheric pressure. The influence of both vacuum annealing and Sb doping on SnS thin films grown at 250 ˚C (single-phase) and 300 ˚C (mixed-phase) were studied. Decomposition of secondary phases was observed after vacuum annealing of the as-grown SnS thin film at 300 ˚C. The existence of secondary phases in the as-grown SnS thin film at 300 ˚C hinders the recrystallization process, and no significant grain growth was observed after vacuum annealing. However, vacuum annealing of a single-phase SnS thin film (SnS grown at 250 ˚C) has dramatically improved the crystalline quality of SnS, and an average grain size of 1.6 μm with a maximum hole mobility of 17 $cm^2V^{-1}s^{-1}$ was achieved. No significant change in grain size was observed when the as-grown sample was vacuum annealed, followed by air annealing. It was observed that the crystalline quality of host SnS thin film has dramatically affected the process of Sb doping. A low level (0.55%) of Sb doping under a controlled S/Sn ratio effectively fabricating Sb doped SnS thin films. However, the conductivity of SnS was remained *p*-type for all Sb doped samples. A "spike-type" SnS/CdS heterojunction was obtained for the device based on the as-grown, vacuum annealed, and Sb doped SnS absorber layer. The band alignment of SnS/CdS heterojunction could be adjusted between "spike" type and "cliff" type by post-annealing treatments.

Table of Contents

List of publications and conference presentations

Peer-reviewed papers

1. A. Abadi, M. T. Htay, Y. Hashimoto, K. Ito, and N. Momose, *"Effect of Sb doping in pure phase SnS thin films",* Japanese Journal of Applied Physics **59**, SCCB11 (2020).
2. A. Abadi, M. T. Htay, Y. Hashimoto, K. Ito, and N. Momose, *"Annealing effect of absorber layer on SnS/CdS heterojunction band alignments",* Japanese Journal of Applied Physics (accepted).

Orally presented papers

1. A. Abadi, M. T. Htay, Y. Hashimoto, K. Ito, and N. Momose, "*Synthesis and characterization of Antimony doped SnS_2 (SnS_2: Sb) Thin films",* The Eighth International Conference on Science and Engineering (8^{th} ICSE), (2017. Dec 9-10), YTU, Yangon, Myanmar.
2. A. Abadi, M. T. Htay, Y. Hashimoto, K. Ito, and N. Momose, *"Controlling carrier concentration of SnS by Sb doping",* The 79^{th} Japanese Society of Applied Physics Autumn meeting, 19a-136-11 (2018. Sep 19-21).
3. A. Abadi, M. T. Htay, Y. Hashimoto, K. Ito, and N. Momose, *"Effect of Sb doping in pure phase SnS thin films",* The 7^{th} International Symposium on Organic and

Inorganic Electronic Materials and Related Nanotechnologies (EM-NANO 2019), SA-6 (2019. Jun 19-22).

4. A. Abadi, M. T. Htay, Y. Hashimoto, K. Ito, and N. Momose*, "Effect of vacuum annealing on pure phase SnS thin films",* The Japan Society of Applied Physics, Hokuriku / Shinetsu branch, C06 (2020. 12).
5. A. Abadi, M. T. Htay, Y. Hashimoto, K. Ito, and N. Momose, *"Annealing effect of absorber layer on SnS/CdS heterojunction band alignments",* The 8th International Symposium on Organic and Inorganic Electronic Materials and Related Nanotechnologies (EM-NANO 2021), A2-3-3 (2021. Jun 1-3).

Chapter 1

Motivation

Developing environmentally friendly and alternative energy sources has become a global concern to supplement the fast-dwindling fossil fuels. Several categories of these alternative or renewable energy technologies exist, such as solar, biomass, hydropower, geothermal, tidal, and wind. Solar energy from the sun, which is effectively inexhaustible, is the most useful among all forms of renewable energy, and it is the potential to contribute to electrical energy. Solar cells are semiconductor devices that directly convert solar radiation into electricity. The crucial integral part of any solar cell device is the solar absorbing material, which absorbs sunlight and transports the resulting charge carriers to the electrical contacts via other supporting components. Crystalline silicon (c-Si) is the most crucial photovoltaic material and is widely used for large-scale solar energy production up to date. However, the c-Si requires a thick layer of material about 100 μm to absorb most of the incident light, whereas the use of thin-film solar cells (TFSCs) requires ~ 2.0 μm to absorb most of the incident photon.[1-5)] The considerable reduction in the active material requirement with TFSCs allows a significant decrease in device costs. Moreover, the large versatility in the device design and fabrication, due to the wide choice of different substrates (rigid, flexible) and deposition techniques for the different device layers, allows engineering and optimizing the solar cell structure to enhance the device performance.

Therefore, thin film PV has been recognized as a promising strategy to obtain high efficiency and low-cost devices, thus fulfilling the actual requirements for the increased electrical

demand. TFSCs based on chalcogenide, such as Cu(In, Ga)(S, $Se)_2$ and CdTe, have significantly improved device efficiency in the last 30 years and have currently reached mass production. Recently, the laboratory (small area) efficiency of CIGS and CdTe have reached a record value of 23.4% and 22.1%, respectively (Fig. 1-1**)**.[6, 7] Despite the significant development of the actual chalcogenide-based PV, these technologies suffer from using toxic (Cd) and rare elements, such as In, Ga, and Te, which their critical supply could be of the primary limits for the sustainability of these technologies in the years to come.

Therefore, the development of new abundant, environmentally friendly, and low-cost material as a possible alternative to CIGS and CdTe TFSCs is still a challenge to fulfill PV massive production requirements. Our lab (Hashimoto-Myo Lab.) generally works on environmentally friendly materials for solar cell, battery, and other related device applications.[8-11] As part of the research, I am working on SnS thin-film solar cell material, a compound semiconductor-based on earth-abundant elements of Sn and S. before I discussed SnS thin films in Chapter-2, I briefly introduced the general properties of compound semiconductors for photovoltaics application in the following section (section 1.1.)

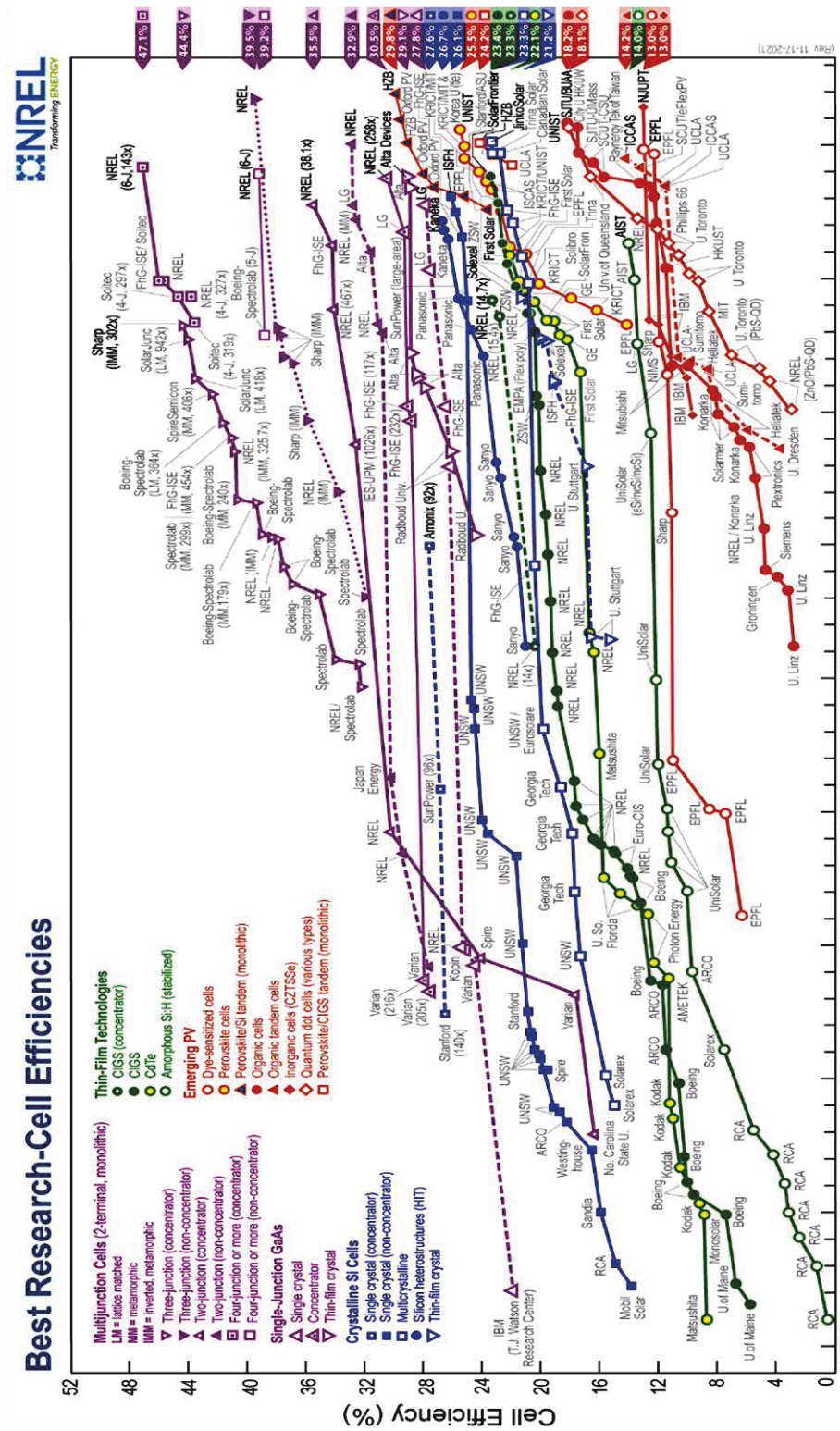

Figure 1-1 Best research solar cell efficiency (National Renewable Energy Laboratory (NREL).[6]

1.1 Optical, electrical, and physical requirements of semiconductors for solar cell application

There are certain material and device properties of semiconductors for PV applications. For theoretical conversion efficiencies under AM1.5 ($\geq$ 30%) solar spectrum, the bandgap should be in the range of 1-1.6 eV (Fig. 1-2).[12] For an acceptable photocurrent level, the quantum efficiency should be high over a broad range of wavelengths. That means that the diffusion lengths must be long compared to the absorption depth, which demands crystal quality. Limiting surfacing recombination by improving the crystallinity of a material, for example, can lessen the rate at which minority carriers are depleted; thereby, their diffusion length could be increased (collection of photo-generated carriers could be increased). These requirements limit the range of materials that can be used for photovoltaic applications. Fig. 1-2 shows the bandgaps of some common semiconductor materials compared to the limiting efficiency in a standard solar spectrum. Several II-VI and I-III-V semiconductors are strong optical absorbers with suitable band gaps for photovoltaic applications. Charge-separation contacts can be realized by a hetero-junction between the absorber and buffer layers (a semiconductor with a wider band gap). Band gaps of materials used as buffer layers are 2.4 eV (CdS), 1.9-2.5 eV (In_2S), and 2.6 ~ 3.4 eV ($ZnO_{1-x}S_x$).[13-15] The choice of a semiconductor for absorber or buffer layers could also be achieved by changing the composition of the constituent elements in the semiconductors or by adopting an external impurity (dopants).

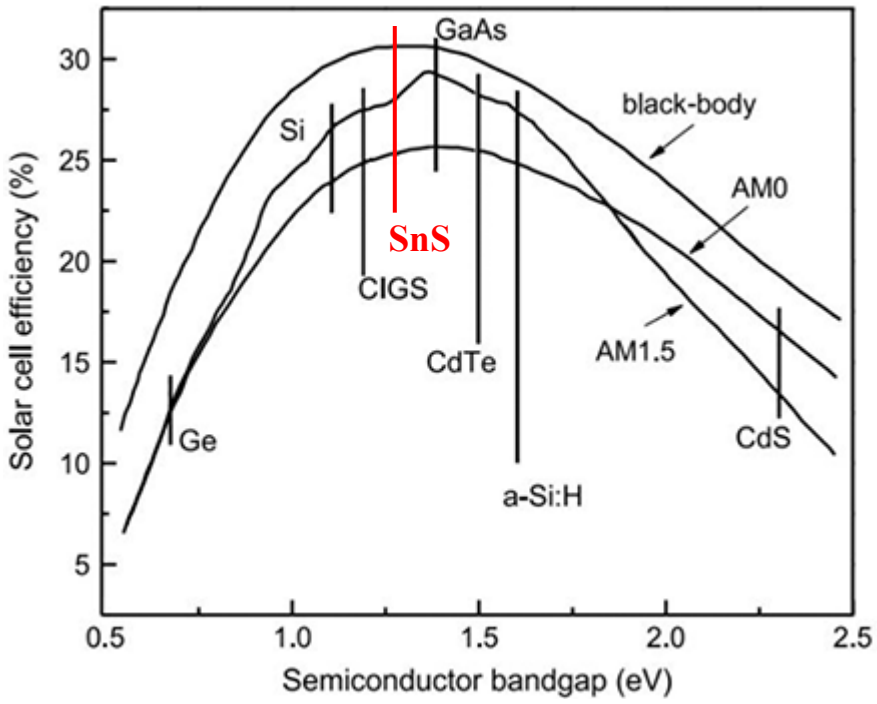

Figure 1-2 Theoretical maximum achievable efficiency versus absorber material band gap.[12)]

In principle, photovoltaic energy conversion consists of two essential steps: i) absorption of light to create electron-hole pairs and ii) separation (and collection) of those electron-hole pairs by the device structure before they recombine. Undoubtedly, the quality of the absorber film itself is the most critical factor in determining the efficacy of these two steps. The existence of secondary phases with undesirable optoelectrical properties, various electrically active intrinsic/extrinsic defects, and grain boundary recombination is a well-known technical issue related to the absorber film's quality.[16-18)] Most of the time, post-treatment and doping techniques are employed to improve the absorber and/or buffer thin-film material. This is aimed to find a single phase of the desired material (by decomposing the secondary

phases), improve the surface and bulk morphology (improve grain size), optical properties (tuning band gap), and control electrical properties (electron/hole carrier density, mobility, and resistivity) of the as-deposited films and thereby improve the overall performance of the solar cell. [19-27)]

Another critical factor is the p-n junction characteristics in the device structure. The lattice mismatch between the absorber and junction partner materials may cause the formation of interfacial defects at a considerably high density, resulting in significant interfacial recombination of the carriers injected from the absorber layer.[18)] Homojunction solar cells are generally preferable over heterojunction structures to effectively collect electron-hole pairs with reduced carrier recombination losses. Homojunction solar cell is achieved by utilizing *n*-type and *p*-type of the same material with potential dopants.[28-30)] The primary advantages of these homojunction-based solar cell structures can be attributed to the excellent lattice and electron affinity matches between the layers.

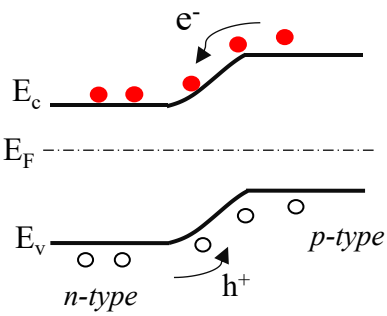

Figure 1-3 Schematic energy band diagrams of absorber and buffer layers showing carrier transport the transport of carriers in the p-n homojunction solar cells.

In the case of heterojunction structure, unfavorable energy band alignment at the junction impedes the separation and collection of the carriers, either by blocking the carrier flow or enhancing the interfacial recombination.[31-33] Depending on the position of the conduction band minimum of these materials, different types of band alignments can form at the p-n junction, as shown in Fig. 1-4, which has a significant impact on the nature of the interfacial recombination of the device. Here, the main concern is the difference between the conduction band minimum of the absorber and buffer layers, which is defined as the conduction band offset, CBO. A CBO in the range of $0\ eV < CBO < 0.4\ eV$ is acceptable in the heterojunction interface without significant effects on the efficiency.[34] If CBO is less than 0 eV, interfacial recombination will be prominent Fig. 1-4(a), while too large a positive CBO value (a large "spike," i.e., $CBO > 0.4\ eV$) impedes the electron transport from the absorber to the buffer Fig. 1.4 (b).[31, 32, 34, 35]

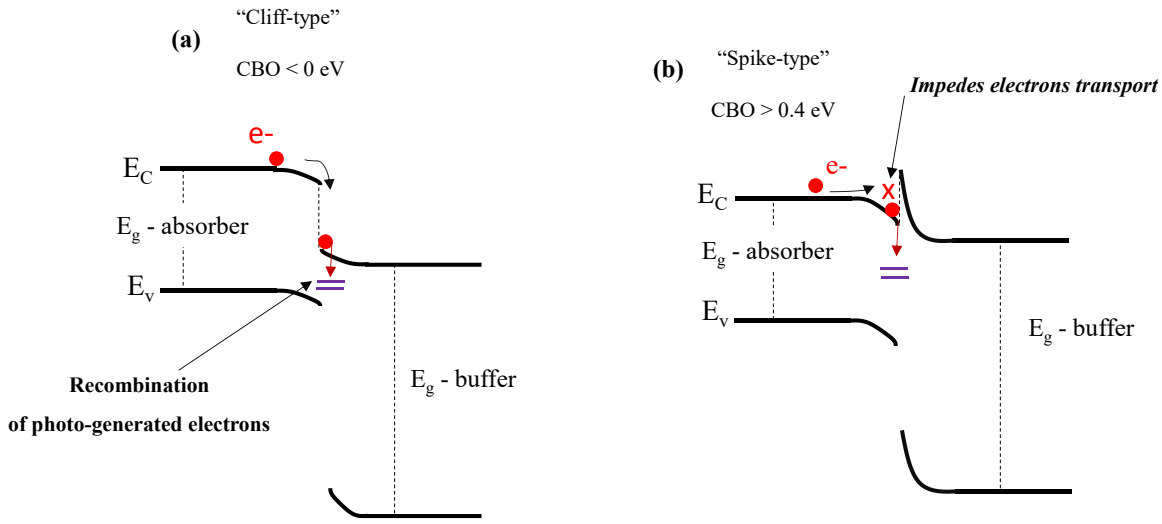

Figure 1-4 Schematic energy band diagrams showing the effects of conduction band offset (CBO), between the absorber and buffer layers on the transport of carriers in the heterojunction solar cells for (a) CBO < 0 eV and (b) CBO > 0.4 eV.

1.2 Objectives of the thesis

The main objective of this thesis is to study the effect of post-treatment conditions on the crystallinity of the SnS thin film's absorber layer and its SnS/buffer heterojunctions. SnS thin films are grown at different sulfurization temperatures, and the effect of vacuum annealing on the crystalline quality of SnS absorber material is studied. The effect of Sb doping on SnS thin films grown at different temperatures is also studied to investigate the possibilities of finding *n*-type SnS thin films (for SnS based homojunction solar cells). Then the effect of post-deposition treatment (vacuum annealing, post-annealing, and Sb doping) of the SnS absorber layer on the SnS/CdS junction band alignment is studied. The band alignment of SnS/TiO_2 is also analyzed to investigate the alternative potential buffer layers for SnS based solar cells.

In general, the objectives of the thesis include the following,

- Optimizing the growth conditions of SnS thin films.
- Studying the effect of vacuum annealing on pure and mixed-phase SnS
- Investigating the effect of Sb doping on the electrical and physical properties of SnS thin films.
- Assessing the influence of vacuum and air annealing on grain growth of SnS thin films.
- Studying the effect of absorber layer annealing on the SnS/CdS band alignment and its effect on the *I-V* characteristics of SnS/CdS devices.
- Studying the band alignment between SnS and TiO_2

1.3 Contribution to the knowledge of the thesis

The state of research on SnS is still underdeveloped despite SnS being a promising absorber material. The thesis aims to exploit this loophole and fill many gaps in the knowledge of SnS based thin-film solar cells. This study has investigated the effect of Sb doping, vacuum annealing, and post-air-annealing (vacuum annealing followed by air annealing) on the material properties of SnS and SnS/buffer band alignments. The vacuum annealing process brings significant grain growth and recrystallization while maintaining good thin film quality. The effect of Sb doping on the electrical properties of SnS was also studied, which could be a possible way to get *n*-type SnS for homojunction solar cell applications in the future. The influence of SnS absorber layer treatment (vacuum and air annealing) on band alignment of the SnS/CdS heterojunctions have been investigated for the first time. The band alignment of SnS/CdS heterojunction could be adjusted between "spike" type to "cliff" type via vacuum annealing followed by post-air-annealing.

1.4 Thesis structure

This thesis is divided into seven (7) chapters. Following this introduction to thin-film photovoltaic technology and fundamental semiconductors (chapter 1), the review of the history of SnS thin film development, material properties, and technologies are presented in chapter 2. Specifically, the SnS absorber treatment and different doping techniques are described in detail. This is followed by the experimental and characterization methods used throughout this work (chapter 3). The experimental results are analyzed and discussed in the following four chapters. Chapter 4 discussed the optimization of growth parameters and the effect of vacuum annealing on mixed-phase SnS grown. The effect of Sb doping on crystallinity and electrical properties of mixed and single-phase SnS thin films is presented in chapter 5, while chapter 6 discusses the heterojunctions of SnS/TiO_2 and SnS/CdS followed by the effect of absorber annealing (vacuum and post-air-annealing) on SnS/CdS band alignment. Finally, the conclusions from the research work and suggestions for future work are presented in chapter 7.

Reference

1. T. Dittrich, *"Materials Concepts for Solar Cells (Energy Futures)",* (Imperial college press, United Kingdom, 2014).
2. J. Nelson, *"The physics of solar cells"* (Imperial college press, United Kingdom, 2003).
3. Y. Ren, J. J. S. Scragg, C. Frisk, J. K. Larsen, Shu-Yi Li, and C. Platzer-Bjorkman *"Influence of the Cu_2ZnSnS_4 absorber thickness on thin film solar cells",* Phys. Status Solidi A **212**, 2889–2896 (2015).
4. C.W.Lan, A.Lan, C.F.Yang, H.P.Hsu, M.Yang, A.Yu, B.Hsu, W.C.Hsu, and A.Yang, *"The emergence of high-performance multi-crystalline silicon in photovoltaics",* J. Cryst. **468**, 17-23(2017).
5. H. Movla, "Optimization of the CIGS based thin film solar cells: Numerical simulation and analysis", Optic 125, 67-70 (2014).
6. National Renewable Energy Laboratory (NREL), https://www.nrel.gov/pv/cell efficiency.html, Best Research-Cell Efficiency Chart (2021).
7. A. Bosio, S. Pasini, and N. Romeo, "*The History of Photovoltaics with Emphasis on CdTe Solar Cells and Modules*", Coatings **10**, 344 (2020).
8. M.T. Htay, T. Mandokoro, H. Seki, T. Sakaizawa, N. Momose, T. Taishi, Y. Hashimoto, K. Ito, *"Influence of Ge composition in the $Cu_2Sn_{1-x}Ge_xS_3$ thin-film*

photovoltaic absorber prepared by sulfurization of laminated metallic precursor", Sol. energy mater. sol. cells **140**, 312–319313 (2015).

9. M. T. Htay, M. Okamura, R. Yoshizawa, Y. Hashimoto, K. Ito *"Synthesis of a cuprite thin film by oxidation of a Cu metal precursor utilizing ultrasonically generated water vapor",* Thin Solid Films **556**, 211–215 (2014).
10. M. T. Htay, Y. Hashimoto, *"Field emission property of ZnO nanowires prepared by ultrasonic spray pyrolysis",* Superlattice Microst. **84**, 144–153 (2015).
11. M. T. Htay, Y. Hashimoto, N. Momose, K. Sasaki, H. Ishiguchi, S. Igarashi, K. Sakurai and K. Ito, *"A Cadmium-Free Cu_2ZnSnS_4/ZnO Hetrojunction Solar Cell Prepared by Practicable Processes",* Jpn. J. Appl. Phys. **50**, 032301 (2011).
12. L. L. Kazmerski, *"Solar photovoltaics R&D at the tipping point: A 2005 technology overview",* J. Electron Spectrosc. Relat. Phenom. **150**, 105–135 (2006).
13. Y. J. Shin, S. K. Kim, B. H. Park, T. S. Jeong, H. K. Shin, and T. S. Kim, *"Photocurrent study on the splitting of the valence band for a CdS single-crystal platelet",* Physical Review B. **44**, 11 (1991).
14. R. Yoosuf, M.K. Jayaraj, *"Optical and photoelectrical properties of β -In_2S_3 thin films prepared by two-stage process",* Sol. Energy Mater Sol. Cells **89**, 85–94 (2005).
15. A. Polity, B. K. Meyer, T. Krämer, C. Wang, U. Haboeck, and A. Hoffmann, *"ZnO based ternary transparent conductors",* Phys. stat. sol. **11**, 2867–2872 (2006).
16. J. Just, C.M. Sutter-Fella, D. Lützenkirchen-Hecht, R. Frahm, S. Schorr, T. Unold *"Secondary phases and their influence on the composition of the kesterite phase in CZTS and CZTSe thin films",* Phys. Chem. Chem. Phys., **18**, 15988-15994 (2016).

17. J.S. Park, S. Kim, Z. Xie, A. Walsh, *"Point defect engineering in thin-film solar cells",* Nat. Rev. Mater., **3**, 194–210 (2018).

18. L.L. Kazmerski, *"The effects of grain boundary and interface recombination on the performance of thin-film solar cells"* Solid State Electron., **21**, 1545-1550 (1978).

19. S. Chander, M.S.Dhaka, *"Impact of thermal annealing on physical properties of vacuum evaporated polycrystalline CdTe thin films for solar cell applications",* Physica E **80**, 62–68 (2016).

20. Jae-Hyung Lee, Ho-Yeol textscLee, Yong-Kwan Park, Sung-Ho Shin, and Kwang-Ja Park, *"Effects of the Annealing Temperature and $CdCl_2$ Treatment on the Photovoltaic Properties of the CdS/CdTe Solar Cell",* Jpn. J. Appl. Phys. **37**, 3357 (1998).

21. N. Ali, S.T. Hussain, Y. Khan, N. Ahmad, M.A. lqbal, S. M. Abbas, *"Effect of air annealing on the band gap and optical properties of $SnSb_2S_4$ thin films for solar cell application",* Materials Letters **100**, 148–151 (2013).

22. S.A. Vanalakar, S.W. Shin, G.L. Agawane, M.P. Suryawanshi, K.V. Gurav, P.S. Patil, J.H. Kim, *"Effect of post-annealing atmosphere on the grain-size and surface morphological properties of pulsed laser deposited CZTS thin films",* Ceramics International **40**, 15097–15103 (2014).

23. S. Temgoua, R. Bodeux, N. Naghavi, S. Delbos, *"Effects of $SnSe_2$ secondary phases on the efficiency of $Cu_2ZnSn(S_x,Se_{1-x})_4$ based solar cells",* Thin Solid Films **582**, 215–219 (2015).

24. Y. Zhao, L. Chang, Xiao-Fei Dong, Hui-Xi Zhang, Y. Li, Jian-Biao Chen, *"Effect of Ag doping on the performance of Cu_2SnS_3 thin-film solar cells",* Sol Energy **201**, 190-194 (2020).

25. S M Al-Shomar, *"Investigation the effect of doping concentration in Ruthenium-doped TiO_2 thin films for solar cells and sensors applications",* Mater. Res. Express **7**, 036409 (2020).

26. Y. Min, S. Dong, H. Shin, J. Hye, K. Byung, T. Ahn, *"Effect of Na doping using Na_2S on the structure and photovoltaic properties of CIGS solar cells",* Curr Appl Phys. **11**, S59-S6 (2011).

27. A. Bag, R. Radhakrishnan, R. Nekovei, R. Jeyakumar, *"Effect of absorber layer, hole transport layer thicknesses, and its doping density on the performance of perovskite solar cells by device simulation",* Sol Energy **196**, 177–182178 (2020).

28. L. Yu, L. Xiong, and Ying Yu, *"Cu_2O Homojunction Solar Cells: F-Doped n-type Thin Film and Highly Improved Efficiency",* J. Phys. Chem. C **119**, 22803−22811 (2015).

29. A. Yamamoto, M. Yamaguchi, and C. Uemura, *"High efficiency homojunction InP solar cells",* Appl. Phys. Lett. **47**, 975 (1985).

30. T. Sugiyama, S. Chaisitsak, A.Yamada, M. Konagai, Y. Kudriavtsev, A. Godines A.Villegas , and R. Asomoza, *"Formation of pn Homojunction in Cu(InGa)Se_2 Thin Film Solar Cells by Zn Doping",* Jpn. J. Appl. Phys. **39**, 4816 (2000).

31. R. Scheer, H.W. Schock, *"Chalcogenide Photovoltaics: Physics, Technologies, and Thin Film Devices",* (John Wiley & Sons, Germany, 2011).

32. K. Ito, *"Copper Zinc Tin Sulfide-Based Thin-Film Solar Cells",* (Wiley, United Kingdom, 2015).

33. D. Abou-Ras, T. Kirchartz, U. Rau, *"Advanced Characterization Techniques for Thin Film Solar Cells",* (John Wiley & Sons, Germany, 2011).

34. T. Minemoto, T. Matsui, H. Takakura, Y. Hamakawa, T. Negami, Y. Hashimoto, T. Uenoyama, M.Kitagawa, *"Theoretical analysis of the effect of conduction band offset of window/CIS layers on performance of CIS solar cells using device simulation,* "Sol. Energy Mater Sol., **67**, 83-88 (2001).

35. C. Ding, Y. Zhang, F. Liu, Y. Kitabatake, S. Hayase, T. Toyoda, K. Yoshino, T. Minemoto, K. Katayama, Q. Shen, *"Effect of the conduction band offset on interfacial recombination behavior ofthe planar perovskite solar cells",* Nano Energy **53**, 17–2618 (2018).

Chapter 2

General properties of tin (II) monosulfide (SnS): a brief overview

Introduction

In recent years, considerable attention has been directed towards studying tin mono-sulfide (SnS) as a possible earth-abundant with low toxic constituents (Sn, S) absorber material for thin-film solar cells. SnS exhibits *p*-type conductivity and is reported to have appropriate bandgap energy of 1.3 eV and a high optical absorption coefficient of > 10^4 cm^{-1}.[1-5]. Several research groups have grown SnS thin films and fabricated SnS solar cells. However, the highest conversion efficiency of such a cell is as low as 4.36%.[6-22] The significant challenges that are yet to be adequately addressed are the existence of secondary phases such as SnS_2 and Sn_2S_3, small grain sizes, and poor band alignments with *n*-buffer layers. These have limited the application of SnS thin films in solar cell devices. Reviewing the SnS phase, intrinsic defects, crystallinity, and optoelectronic properties is vital to understanding SnS films' properties to improve device performance.

2.1 Phases, phase diagrams, and stability

SnS is composed of tin and sulfur, with Sn having dual valency (Sn^{2+} and Sn^{4+}), leading to various phases dependent on the atomic composition.[29] SnS and SnS_2 contain Sn in Sn2+ and Sn4+ oxidation states, respectively, while Sn_2S_3 adopts a mixed oxidation state of Sn^{2+} and Sn^{4+}.[29] Some of the basic properties for the most intensively studied tin sulfide (SnS, Sn_2S_3, and SnS_2) semiconductor materials are presented in table 2-1.

Table 2-1. Basic properties of tin sulfide phases.

Material	Structure	a (Å)	b (Å)	c (Å)	E_g (eV)	Type of conductivity
SnS (tin monosulfide)	Cubic	11.60			1.68	p [23, 24]
SnS (tin monosulfide)	Orthorhombic	4.33	11.21	3.99	1.35	p [6, 25, 26]
SnS_2 (tin disulfide)	Hexagonal	3.64	3.64	5.90	2.22	n [27]
Sn_2S_3(tin sesquisulfide)	Orthorhombic	8.84	14.02	3.74	2.05	n [28]

In order to synthesize pure phase SnS crystals, it is important to know the phase diagram (see Fig. 2-1). This shows secondary phases such as SnS_2 and Sn_2S_3 exist to the sulfur-rich side, whereas SnS is limited only to a very narrow stoichiometric compositional region in the Sn–S phase diagram. The presence of secondary phases (SnS_2 and Sn_2S_3) in SnS thin films acts as a recombination center for holes and negatively affects the power conversion efficiency of SnS-based PV devices.[29] Therefore, a good understanding of the SnS phase formation would be helpful to guide the deposition processes that can lead to obtaining a pure SnS layer with suitable properties for photovoltaic application. Fig. 2-1 also show that the

orthorhombic SnS thin film is existed in either α-SnS or β-SnS phases which are stable at room and high temperatures, respectively.[30-34)]

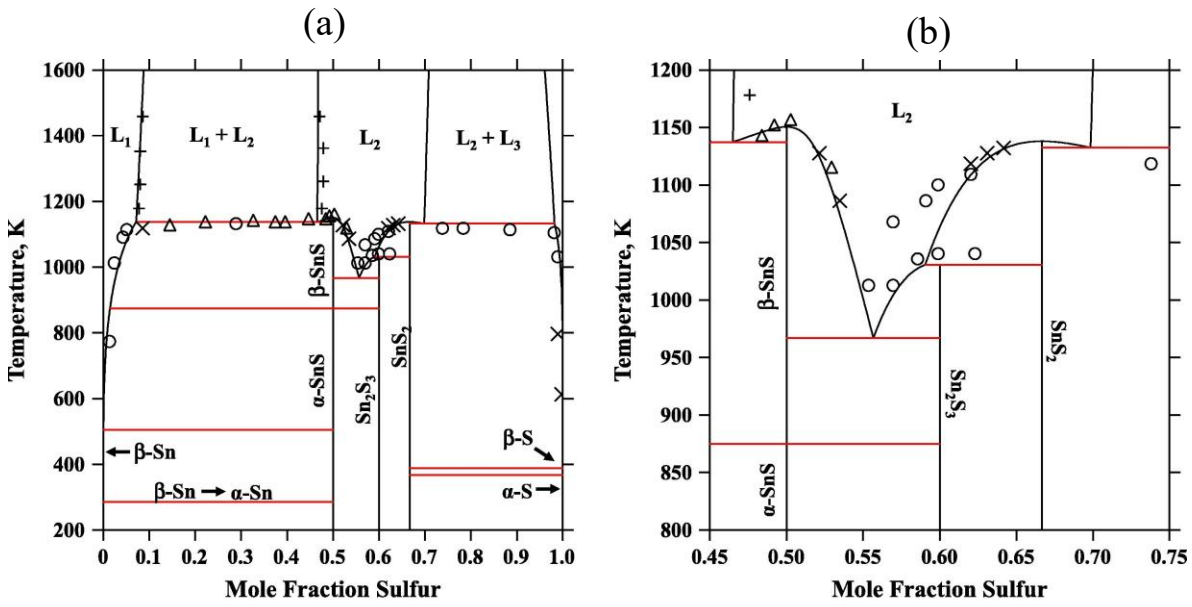

Figure 2-1 Calculated phase diagram for the S–Sn system compared to experimental data; ○, +, Δ, and ×. The phase diagram is calculated at the pressure 1 bar. (b) is an enlargement of the central part of the phase diagram (a), and the letter L indicates liquid. Red solid lines represent invariant transformation temperatures.[35)]

A challenge for SnS studies is that the vapor pressure of sulfur is much larger than that of tin. For thermal methods or annealing of SnS, sulfur volatilizes more quickly, so maintaining a 1:1 ratio of Sn:S becomes an issue. For slightly sulfur deficient films, V_{Sn} will still form quickly due to their low formation energy.[36] However, a sulfur-deficient film will result in excess tin accumulation due to the high V_{Sn} concentration. The formation energy of S and Sn vacancies in S- rich (Fig. 2-2(a)) and Sn-rich (Fig. 2-2(b)) conditions are shown in Fig. 2-2. V_S has lower formation energy in an Sn-rich lattice than an S-rich lattice. The reverse is also true for V_{Sn}, but the formation energy of the two vacancy types is closer in value for the Sn-rich system.

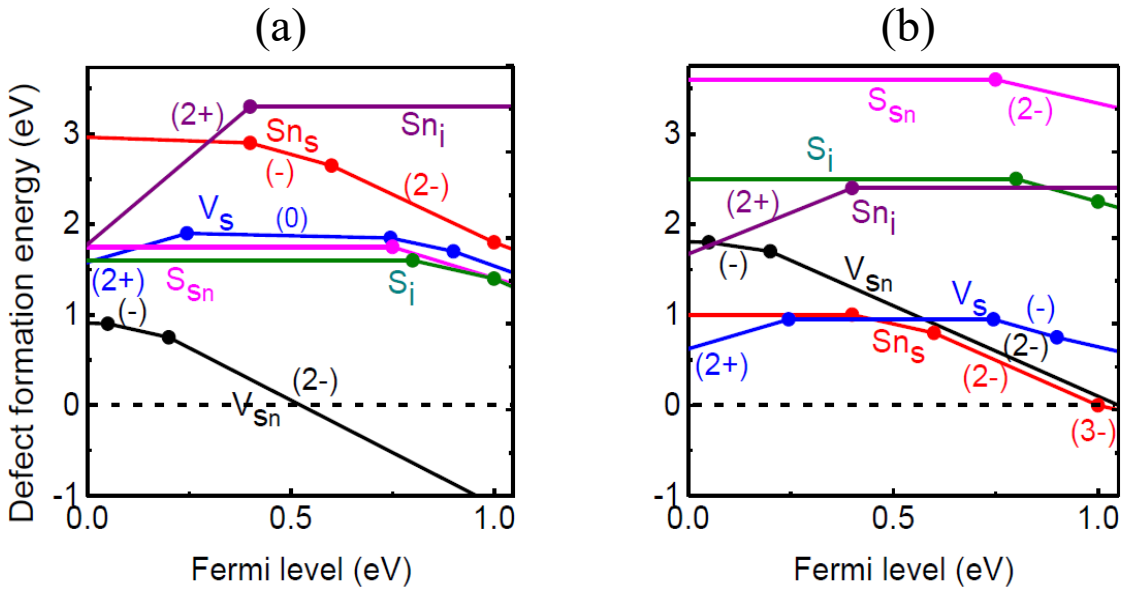

Figure 2-2 Calculated defect formation enthalpies for intrinsic defects in S-rich (a) and Sn-rich (b) limits in SnS.[36]

2.2 Post deposition annealing and doping

To realize single-phase SnS and thereby improve the quality of SnS thin films solar cell, thermal annealing of as-grown SnS films at different ambience has been commonly used. Revathi *et al.* studied the effect of thermal annealing on SnS thin films in hydrogen sulfide (H_2S) and argon for different durations.[37] They demonstrated that annealing in H_2S at 400 ˚C changes the stoichiometry of the as-deposited SnS films, and a dominant SnS_2 phase was formed. However, the composition of as-deposited SnS was not changed by annealing it in argon ambience for 1 h. Vacuum annealing significantly improved the crystalline structure, surface morphology, and optical properties of the SnS. Devika *et al.* have studied rapid thermal annealing (RTA) for the thermally evaporated SnS thin films in nitrogen ambience at different temperatures from 100 ˚C to 550 ˚C for 1 min.[38] The as-grown and annealed SnS films exhibited a strong peak that belongs to (111) orientation of the orthorhombic structured SnS crystal. They also reported that SnS films annealed at 300 °C showed a low electrical resistivity, mobility, and carrier concentration of ~ 36 Ω cm, 41 $cm^2V^{-1}s^{-1}$, and 4.2×10^{15} cm^{-3}, respectively. Upon increasing the annealing temperature to 500 ˚C, the electrical resistivity was dramatically increased while hole mobility was decreased. Annealing in nitrogen at 260 ˚C of SnS:Ag films with a duration of 60-180 min were reported by Jia *et al.*[39] As a result of annealing, they obtained polycrystalline orthorhombic SnS films with (111) preferred plane, carrier concentration up to 1.1×10^{17} cm^{-3}, and resistivity of about 3.1 Ω cm. They also reported the improvement in the uniformity and crystallization of the films, the rise and drop in carrier concentration and mobility of the films (first rise and then drop) within the annealing time in the range of 60-180 min, whereas their resistivity and direct bandgap

energy E_g show the contrary trend.

Post-annealing of as-purchased sulfur powder is also an alternative to finding a phase pure SnS thin films by Steinmann et al.40). They found that the purchased SnS powder (purity of 99.5%) contains a significant amount of sulfur-rich phases, i.e., Sn_2S_3 and SnS_2. To grow a pure phase SnS, they post-annealed the as-purchased SnS powder and then they evaporated a SnS thin film (as-purchased = > post-annealing = > thin-film evaporation). The following equations show the decomposition process of secondary phases and the possible formation of pure phase SnS at the higher annealing temperature.[40, 41)]

$$SnS_2(s) => {}^1/_2\, Sn_2S_3(s) + {}^1/_4\, S_2(g) \quad (2\text{-}1)$$

$$Sn_2S_3(s) => 2SnS\,(s) + {}^1/_2\, S_2(g) \quad (2\text{-}2)$$

$$SnS\,(s) => SnS\,(g) \quad (2\text{-}3)$$

Accordingly, Steinmann *et al.* have annealed the as purchased SnS powder at 500 ˚C, and sulfur-rich secondary phases have decomposed into single-phase SnS. The SnS thin film was then deposited on a soda-lime glass substrate by evaporating the post-annealed pure phase SnS powder.

2.3 SnS doping

Besides the annealing process of SnS thin films, researchers in the field are employing extrinsic doping to control the carrier concentration and to realize *n*-type conductive SnS-based homojunction solar cell application.

Direct vapor transport (DVT) technique was used by Chaki *et al.* for depositing In (Indium) and Sb (Antimony) doped SnS single crystals, with In and Sb shots as dopant

sources in the quartz ampoule.[42] They reported a noticeable shift in XRD peaks, and the crystallite size decreases significantly in both In and Sb doped SnS single crystal samples compared to pure SnS. The grown single crystal samples were all (doped and undoped) *p*-type semiconductors. For doping concentration (both In and Sb) < 5%, the resistivity decreased while carrier concentration increased. However, they observed an increase in resistivity and a decrease in carrier concentration as doping concentration was increased from 5% to 15% for both In and Sb doped SnS. The report also showed that the optical bandgap decreases with doping concentration.

Dussan *et al.* has grown a SnS:Bi thin films through a chemical reaction of a metallic precursor with elemental sulfur in a two-stage process.[43] In the first stage, a thin film (Sn:Bi alloy) was deposited on a glass substrate by evaporating a mixture of Sn and Bi. In the second stage, the grown Sn:Bi alloy was annealed in sulfur (S) ambience at the temperature range of 350 - 450 ˚C for 40 min. Depending upon the concentration of Bi in the evaporated Sn:Bi alloy, the formation of different phases was observed after sulfurization. For Bi concentration greater than 50%, Bi_2S_3, SnS_2, and SnS phases were observed while a mixture of Bi_2S_3, SnS, and Sn_2S_3 phases was observed for Bi concentration less than 50%. SnS:Bi thin films showed *n*- and *p*-type conductivity for Bi concentration greater than and less than 50%, respectively.

Kafashan has reported Se doped SnS thin films by Electrochemical technique.[44] The crystalline quality of doped SnS films was improved up to 2.32% of Se doping due to the creation of new nucleation centers having sizes up to 79.57 nm. Further, above, crystalline quality was decreased due to saturation of nucleation centers & lattice mismatch. They also reported that the morphology of the films was also changed through doping. Undoped SnS

thin films had two morphology types cubic and plate shape grains with dimensions 200-400 nm which tend to convert into rectangular based plates and planar shape grains (30-80 nm and 60-100 nm) up to 2.32% of Se doping.

Zhang *et al*. have grown Cu-doped SnS films by thermal evaporation technique under vacuum at a temperature of 250 ˚C for 90 minutes.[45] The grain size becomes more prominent, and the surface becomes smoother as the doping concentration increases from 0 to 23%. The energy band gap of doped films first decreases from 1.54 eV to 1.38 eV, and the crystallinity deteriorates as Cu doping concentration increases from 0 to 15%. According to their report, the replacement of Sn ions by Cu could be the reason for the structural deformation and the decrease in the band gap energy of SnS thin films. However, band gap energy was increased to 1.71 eV for Cu doping concentration at 23%, and the formation of SnS_2, which could be the reason for the increase in the band gap, was observed. The carrier concentration of the films gradually increases (1.53×10^{15} cm^{-3} to 8.51×10^{19} cm^{-3}) with increasing Cu doping while resistivity decreases from 8.99×10^{2} Ω cm to 2.33×10^{-1} Ω cm. All the Cu-doped SnS thin films show *p*-type conductivity.

Sb doped SnS thin films with $SbCl_3$ (2 to10 at %) as dopant source was reported by Kumar *et al.* using spray pyrolysis technique.[46] XRD results showed the polycrystalline nature of doped and undoped films with an orthorhombic crystal structure. The crystallinity of SnS thin films improved up to 6% of Sb doping, and the average roughness was increased from 9.8 nm to 15.18 nm. The optical properties of SnS thin films were also affected by Sb doping. The band gap of SnS thin films decreased from 1.60 eV (undoped) to 1.15 eV (doped) with

6% Sb doping. The resistivity of the films was also found to reduce from 7.9×10^2 Ω cm to 2.5×10^{-2} Ω cm. At the same time, carrier concentration and mobility increased from 5.9 $\times 10^{15}$ to 3.9×10^{19} cm^{-3} and 133.54 to 688.43 $cm^2V^{-1}s^{-1,}$ respectively, as doping concentration was increased.

Cl-doped single-crystalline SnS was synthesized via a self-flux method by Iguchi *et al.*[47]**.** A mixture of Sn grains, S powder, and $SnCl_2$ powder was placed in a silica glass tube. The silica tubes were then heated to 520 ˚C for 12 h and maintained at this temperature for 24 h. They subsequently cooled to 240 ˚C for 36 h and cooled to room temperature for 12 h. They achieved *n*-type single-crystalline SnS at 0.14% Cl concentration. The crystal size was similar to that of *single p-typ*e crystals, and the lattice parameters were not affected by doping.

However, the difficulty in controlling the carrier concentration and the presence of secondary impurity phases still remained to be addressed. Among the dopants discussed above, Sb (1.36 Å) is one of the promising *n*-type dopants because of its similarity in ionic radius with Sn (1.37 Å).[48, 49]

2.4 SnS based-solar cells: PV performance history and limitations

As discussed in the introduction part of this chapter, the efficiency of SnS-based solar is still below 5%. Finding one adequate buffer material is one of the greatest challenges for SnS based solar cells. Investigation of the valence band offset (VBO) and conduction band offset (CBO) is essential for device design and development because these values determine the junction transport and other interface-related properties. There were few experimental and

theoretical reports available in the literature on the band discontinuities between SnS and other buffer materials used for solar cells.[50-54] This section reviews the SnS-based solar cell efficiency reported using different buffer layers and band alignment techniques.

In 1994, Noguchi *et al.* reported a short circuit current density (*Jsc*) of 7 mA/cm^2, an open-circuit voltage (V_{OC}) of 0.12 V, a fill factor (*FF*) of 0.35, and a conversion efficiency (η) of 0.29% using CdS as a buffer layer.[6] Avellandea *et al.* have reported a solar cell (CdS/ π-SnS/SnS(OR)/metal) using cubic SnS (π-SnS) and orthorhombic SnS (OR) thin films which have different optical band gaps and crystal structures.[55] The reported solar cell exhibited V_{OC} = 370 mV, *J*sc = 1.23 mA/cm^2, *FF* = 0.44, and η = 0.2%. They reported the light-generated current density improvement when the two types of SnS absorber films were used. One year later, Malaquias *et al.* reported a solar cell with V_{OC} = 183 mV, *Jsc* = 2.7 mA/cm^2, *FF* = 0.34, and η = 0.17% using the SLG/Mo/Sn_xS_y/CdS/ZnO:Ga structure.[13] They have grown Sn_xS_y thin films by sulfurizing metallic precursors in a temperature range of 300 - 520 ˚C. They obtained solid mixtures of SnS, SnS_2, and Sn_2S_3 for all grown samples. Bashkirov *et al* have reported a Mo/p-SnS/n-CdS/i-ZnO/Al-doped ZnO solar cell in 2012.[15] The fabricated solar cell was exhibited V_{OC} = 132 mV, *Jsc* = 3.6 mA/ cm^2, *FF* = 0.29, and η = 0.5%. In 2013, Ikuno *et al.* reported an SnS-based solar cell using $Zn_{1-x}Mg_xO$ as a buffer layer.[16] They carried out a band alignment at the SnS/ $Zn_{1-x}Mg_xO$ by varying the Mg content of the buffer layer. They reported the optimum value of CBO for an improved solar cell in a range of -0.1 to 0 eV. The *Voc, Jsc, FF*, and η values for the best performance of the $Zn_{0.83}Mg_{0.17}O$/SnS cell (CBO = 0 eV were 0.27 V, 12.1 mA/cm^2, and 0.64, and 2.1%, respectively. A record efficiency was achieved for SnS-based thin-film solar cells by varying

the oxygen-to-sulfur ratio in Zn(O, S) by Prasert *et al.*.[19] The SnS/Zn(O,S) solar cell with S/Zn ratio of 0.37 exhibited *Jsc* = 19.4 mA/cm^2, *Voc* = 0.244 V, *FF* = 0.43, and η = 2.46 %. In 2014, this efficiency value was further improved by adding a SnO_2 layer of a few nanometers at SnS/Zn(O,S) interface, reaching a new record efficiency of 4.36 %.[22] Despite the initial success in applying the Zn-based buffer as the junction partner of SnS, the lower photovoltage (photovoltage below 0.4 eV) still remains a major limiting factor for achieving high-efficiency SnS-based solar cells. Therefore, it is necessary to find a more appropriate junction material that can further mitigate the interfacial recombination in SnS devices. Wang *at al.* reported a SnS/TiO_2 structure with *Voc* = 471 mV, *J*sc = 0.3 mA/cm^2, and η = 0.1% under 1 sun illumination.[12] This indicates the considerable potential of TiO_2 as an alternative buffer layer for SnS-based solar cells.

Even though encouraging efficiency progress for SnS-based thin-film solar cells was achieved by applying Zn-based buffer layers and the highest open-circuit voltage with TiO_2 buffer layer, no further improvement in efficiency is observed. Therefore, it is necessary to conduct a thorough study of both SnS absorber material and the selection of buffer layers to know which of these two significantly impact the performance of SnS-based solar cells. In this thesis, we studied the band alignment between the SnS absorber layer and buffer layers (SnS/CdS and SnS/TiO_2) to investigate the potential use and the limiting factors of these buffer layers in SnS-based solar cells. We detail the influence of post-annealing treatment on both SnS absorber material property and on the band alignment of the SnS/CdS heterojunctions. We studied the effect of vacuum annealing, Sb doping, and post-air-annealing (vacuum annealing followed by air annealing) on SnS absorber thin films' material

properties and on the band offset at SnS/CdS hetero-interface. We have evaluated the conduction band offset (CBO) and valence band offset (VBO) of the hetero-interface consisting of the SnS thin film, which was annealed under various conditions.

Reference

1) H.K. Park, J. Jo, H.K. Hong, G.Y. Song, and J. Heo, *"Structural, optical, and electrical properties of tin sulfide thin films grown with electron-beam evaporation",* Curr. Appl. Phys. **15**, 964–969 (2015).

2) M. M. El-Nahass, H. M. Zeyada, M. S. Aziz, and N. A. El-Ghamaz, *"Optical properties of thermally evaporated SnS thin films",* Opt. Mater. **20**, 159-170, (2002).

3) A. E. Abdelrahman, W. M. M. Yunus, and A. K. Arof, *"Optical properties of tin sulphide (SnS) thin film estimated from transmission spectra",* J. Non-Cryst. Solids **358**, 1447-1451 (2012).

4) S. S. Hegde, A. G. Kunjomana, P. Murahari, B. K. Prasad, and K. Ramesh, *"Vacuum annealed tin sulfide (SnS) thin films for solar cell applications",* Surf. Interfaces **10**, 78-84 (2018).

5) A. Jakhar, A. Jamdagni, A. Bakshi, T. Verma, V. Shukla, P. Jain, N. Sinha, and P. Arun, *"Refractive index of SnS thin nano-crystalline films",* Solid State Commun.**168**, 31-35 (2013).

6) H. Noguchi, A. Setiyadi, H. Tanamura, T. Nagatomo, and O. Omoto, *"Characterization of vacuum-evaporated tin sulfide film for solar cell materials",* Sol. Energy Mater. Sol. Cells **35**, 325-331 (1994).

7) A. Sanchez-Juarez, A. Tiburcio-Silver, and A. Ortiz, *"Fabrication of SnS_2/SnS heterojunction thin film diodes by plasma-enhanced chemical vapor deposition",* Thin Solid Films **480–481**, 452 – 456 (2005).

8) K.T. R. Reddy, N.K. Reddy, and R.W. Miles, *"Photovoltaic properties of SnS based solar cells",* Sol. Energy Mater. Sol. Cells **90**, 3041–3046 (2006).

9) M. Gunasekaran and M. Ichimura, *"Photovoltaic cells based on pulsed electrochemically deposited SnS and photochemically deposited CdS and $Cd_{1-x}Zn_xS$",* Sol. Energy Mater. Sol. Cells **91**, 774–778 (2007).

10) D. Avellaneda, G. Delgado, M.T.S. Nair, and P.K. Nair, *"Structural and chemical transformations in SnS thin films used in chemically deposited photovoltaic cells",* Thin Solid Films **515,** 5771–5776 (2007).

11) B. Ghosh, M. Das, P. Banerjee, and S. Das, *"Fabrication of vacuum-evaporated SnS/CdS heterojunction for PV applications",* Sol. Energy Mater. Sol. Cells **92**, 1099– 1104 (2008).

12) Y. Wang, H. Gong, B. Fan, and G. Hu, *"Photovoltaic Behavior of Nanocrystalline SnS/TiO_2",* J. Phys. Chem. **C114**, 3256–3259 (2010).

13) J. Malaquias, P.A. Fernandes, P.M.P. Salome, and A.F. da Cunha, *"Assessment of the potential of tin sulphide thin films prepared by sulphurization of metallic precursors as cell absorbers",* Thin Solid Films **519**, 7416-7420 (2011).

14) G. Yue, Y. Lin, X. Wen, L. Wang, and D. Peng, *"SnS homojunction nanowire-based solar cells",* J. Mater. Chem. **22**, 16437-16441 (2012).

15) S.A. Bashkirov, V.F. Gremenok, V.A. Ivanov, V.V. Lazenka, and K. Bente, *"Tin sulfide thin films and Mo/p-SnS/n-CdS/ZnO heterojunctions for photovoltaic applications",* Thin Solid Films **520**, 5807–5810 (2012).

16) T. Ikuno, R. Suzuki, K. Kitazumi, N. Takahashi, N. Kato, and K. Higuchi, *"SnS thin film solar cells with $Zn_{1-x}Mg_xOZn_{1-x}Mg_xO$ buffer layers",* Appl. Phys. Lett. **102**, 193901 (2013).

17) A. Schneikart, H.-J. Schimper, A. Klein, and W. Jaegermann*, "Efficiency limitations of thermally evaporated thin-film SnS solar cells",* J. Phys. D Appl. Phys. **46**, 305109 (2013).

18) S.S. Hegde, A.G. Kunjomana, M. Prashantha, C. Kumar, and K. Ramesh, *"Photovoltaic structures using thermally evaporated SnS and CdS thin films",* Thin Solid Films **545**, 543–547 (2013).

19) P. Sinsermsuksakul, K. Hartman, S.B. Kim, J. Heo, L. Sun, H.H. Park, R. Chakraborty, T. Buonassisi, and R.G. Gordon, *"Enhancing the efficiency of SnS solar cells via band-offset engineering with a zinc oxysulfide buffer layer",* Appl. Phys. Lett. **102**, 053901 (2013).

20) H. H. Park, R. Heasley, L. Sun, V. Steinmann, R. Jaramillo, K. Hartman, R. Chakraborty, P. Sinsermsuksakul, D. Chua1, T. Buonassisi, and R. G. Gordon, *"Co-*

optimization of SnS absorber and Zn(O,S) buffer materials for improved solar cells", Prog. Photovolt: Res. Appl. **23**, 901–908 (2015).

21) A. Wangperawong, P.-C. Hsu, Y. Yee, S.M. Herron, B.M. Clemens, Y. Cui, and S.F. Bent, *"Bifacial solar cell with SnS absorber by vapor transport deposition",* Appl. Phys. Lett. **105**, 173904 (2014).

22) P. Sinsermsuksakul, L. Sun, S.W. Lee, H.H. Park, S.B. Kim, C. Yang, and R.G. Gordon, *"Overcoming Efficiency Limitations of SnS-Based Solar Cells",* Adv. Energy Mater. **4**, 1400496 (2014).

23) A. Javed, N. Khan, S. Bashir, M. Ahmad, M. Bashir, *"Thickness dependent structural, electrical and optical properties of cubic SnS thin films",* Mater. Chem. Phys. **246**, 122831 (2020).

24) U. Chalapathi, B.Poornaprakash, Si-Hyun Park, *"Chemically deposited cubic SnS thin films for solar cell applications",* Sol Energy **139**, 238-248 (2016).

25) M. Calixto-Rodriguez, H. Martinez, A. Sanchez-Juarez, J. Campos-Alvarez, A. Tiburcio-Silver, M.E. Calixto, *"Structural, optical, and electrical properties of tin sulfide thin films grown by spray pyrolysis",* Thin Solid Films **517**, 2497–2499 (2009).

26) M. Devika, K.T. Ramakrishna Reddy, N. Koteeswara Reddy, K. Ramesh, R. Ganesan, E.S.R. Gopal, K.R. Gunasekhar, *"Microstructure dependent physical properties of evaporated tin sulfide films",* J. Appl. Phys. **100**, 023518 (2006).

27) K. Kourtakis, J. DiCarlo, R. Kershaw, K. Dwight, A. Wold, *"Preparation and characterization of SnS_2",* J. Solid State Chem. **76**, 186–191 (1988).

28) H. B. H. Salah, H. Bouzouita, B. Rezig, *"Preparation and characterization of tin sulphide thin films by a spray pyrolysis technique",* Thin Solid Films **480–481**, 439–442 (2005).

29) T. Jiang and G. A. Ozin, "New *directions in tin sulfide materials chemistry*", J. Mater. Chem. **8**, 1099–1108 (1998).

30) J. M. Skelton, L. A. Burton, F. Oba, and A. Walsh, *"Lattice dynamics of the tin sulphides SnS_2, SnS and Sn_2S_3: vibrational spectra and thermal transport"*, J. Phys. Chem. C.**121**, 6446-6454 (2017).

31) L. A. Burton and A. Walsh, *"Phase Stability of the Earth-Abundant Tin Sulfides SnS, SnS_2, and Sn_2S_3",* J. Phys. Chem. C, **116**, 24262-24267 (2012).

32) E. C. Greyson, J. E. Barton, and T. W. Odom, *"Tetrahedral Zinc Blende Tin Sulfide Nano- and Microcrystals"*, Small, **2**, 368-371 (2006).

33) A. Walsh and G. W. Watson, *"Influence of the Anion on Lone Pair Formation in Sn(II) Monochalcogenides: A DFT Study",* J. Phys. Chem. **109**, 18868-18875 (2005).

34) J. M. Skelton, L. A. Burton, F. Oba, and A. Walsh, *"Lattice dynamics of the tin sulphides SnS_2, SnS and Sn_2S_3: vibrational spectra and thermal transport"*, J. Phys. Chem. C. **121**, 6446-6454 (2017).

35) G. Lindwall, S. Shang, N. R.Kelly, T. Anderson, and Zi-KuiLiu, *"Thermodynamics*

of the S–Sn system: Implication for synthesis of earth abundant photovoltaic absorber materials", Sol Energy **125**, 314–323 (2016).

36) J. Vidal, S. Lany, M. d'Avezac, A. Zunger, A. Zakutayev, J. Francis, and J. Tate, *"Band-structure, optical properties, and defect physics of the photovoltaic semiconductor SnS"* Appl. Phys. Lett. **100**, 032104 (2012).

37) N. Revathi, S. Bereznev, M. Loorits, J. Raudoja, J. Lehner, J. Gurevits, R. Traksmaa, V. Mikli, E. Mellikov, and O. Volobujeva, *"Annealing effect for SnS thin films prepared by high-vacuum evaporation",* Vac. Sci. Technol. A **32**, 061506 (2014).

38) M. Devika, N. koteswara Reddy, and K.R. Gunasekhar, *"Structural, electrical, and optical properties of as-grown and heat treated ultra-thin SnS films",* Thin Solid Films **520**, 628–632 (2011).

39) H. Jia, S. Cheng, and P. Lu, *"Effect of Anneal Time on Photoelectric Properties of SnS:Ag Thin Films",* Adv. Mater. Res. **152-153**, 752–755 (2011).

40) V. Steinmann, R. Jaramillo, K. Hartman, R. Chakraborty, R.E. Brandt, J.R. Poindexter, Y.S. Lee, L. Sun, A. Polizzotti, H.H. Park, R.G. Gordon, T. Buonassisi, *"3.88% efficient tin sulfide solar cells using congruent thermal evaporation",* Adv. Mater. **26**, 7488-7492 (2014).

41) D. G. Moon, S. Rehan, D. H. Yeon, S. M. Lee, S. J. Park, S. Ahn, Y. S. Cho, *"A review on binary metal sulfide heterojunction solar cells",* Solar Energy Materials and Solar Cells **200**, 109963 (2019).

42) S. H. Chaki, M. D. Chaudhary, and M.P. Deshpande, *"Effect of indium and antimony*

doping in SnS single crystals", Mater Res Bull. **63**, 173-180 (2015).

43) A. Dussan, F. Mesa, G. Gordillo, *"Effect of substitution of Sn for Bi on structural and electrical transport properties of SnS thin films",* J Mater Sci. **45**, 2403–2407 (2010).

44) H. Kafashan, *"X-ray Diffraction Line Profile Analysis of Undoped and Se Doped SnS Thin Films Using Scherrer's, Williamson–Hall and Size–Strain Plot Methods",* J. Electron. Mater. **48**, 1294–1309 (2019).

45) S. Zhang and S. Cheng, *"Thermally evaporated SnS:Cu thin films for solar cells",* Micro Nano Lett. **6**, 559 –562 (2011).

46) K. S. Kumar, C. Manoharan, S. Dhanapandian, and A. G. Manohari, *"Effect of Sb dopant on the structural, optical and electrical properties of SnS thin films by spray pyrolysis technique",* Spectrochim. Acta A Mol. Biomol. Spectrosc. **115**, 840–844 (2013).

47) Y. Iguchi, K. Inoue, T. Sugiyama, and H. Yanagi *"Single-Crystal Growth of Cl-Doped n-type SnS Using $SnCl_2$ Self-Flux"*, Inorg. Chem. **57**, 6769−6772 (2018).

48) A. Takeuchi and A. Inoue, *"Classification of Bulk Metallic Glasses by Atomic Size Difference, Heat of Mixing and Period of Constituent Elements and Its Application to Characterization of the Main Alloying Element",* Mater. Trans. **12**, 2817 (2005).

49) M. Fadel, *"The effect of the Sb content on the physical properties of amorphous $Se_{0.75}Ge_{0.25-y}$ thin films",* Vacuum **52**, 277 (1999).

50) M. Ichimura, *"Calculation of band offsets at the CdS/SnS heterojunction"* Sol. Energy Mater. Sol. Cells **93**, 375–378 (2009).

51) K.T. Ramakrishna Reddy, K. Ramya, G. Sreedevi, T. Shimizu, Y. Murata, M.

Sugiyama, *"Studies on the Energy Band Discontinuities in SnS/ZnMgO Thin Film Heterojunction",* Energy Procedia **10**, 172 – 176 (2011).

52) M. Sugiyama, K.T.R. Reddy, N. Revathi, Y.Shimamoto, and Y. Murata, *"Band offset of SnS solar cell structure measured by X-ray photoelectron spectroscopy",* Thin Solid Films **519**, 7429–7431 (2011).

53) L.A. Burton and A. Walsh, *"Band alignment in SnS thin-film solar cells: Possible origin of the low conversion efficiency",* Appl. Phys. Lett. **102**, 132111 (2013).

54) L. Sun, R. Haight, P. Sinsermsuksakul, S. B. Kim, H.H. Park, and R.G. Gordon, *"Band alignment of SnS/Zn(O,S) heterojunctions in SnS thin film solar cells",* Appl. Phys. Lett. **103**, 181904 (2013).

55) D. Avellaneda, M.T.S. Nair, and P.K. Nair, *"Photovoltaic structures using chemically deposited tin sulfide thin films",* Thin Solid Films **517**, 2500–2502 (2009).

Chapter 3

Fabrication procedure

Tin (II) monosulfide (SnS) thin films have been fabricated by a two-stage process. This involved the deposition of tin (Sn) onto soda-lime glass (SLG) substrates using RF sputtering followed by annealing in the presence of elemental sulfur. This chapter covers the detailed steps involved in preparing SnS thin films and their heterojunction. The process is outlined in Fig. 3-1.

3.1. Substrate preparation

Soda-lime glass (SLG) was used as a substrate. The glass was cut to 11 × 17 mm_2, cleaned with a neutral detergent followed by methanol, trichloroethylene, acetone, methanol, and isopropanol under ultrasonic agitation, and finally dried with N_2 gas before loading into RF sputtering equipment.

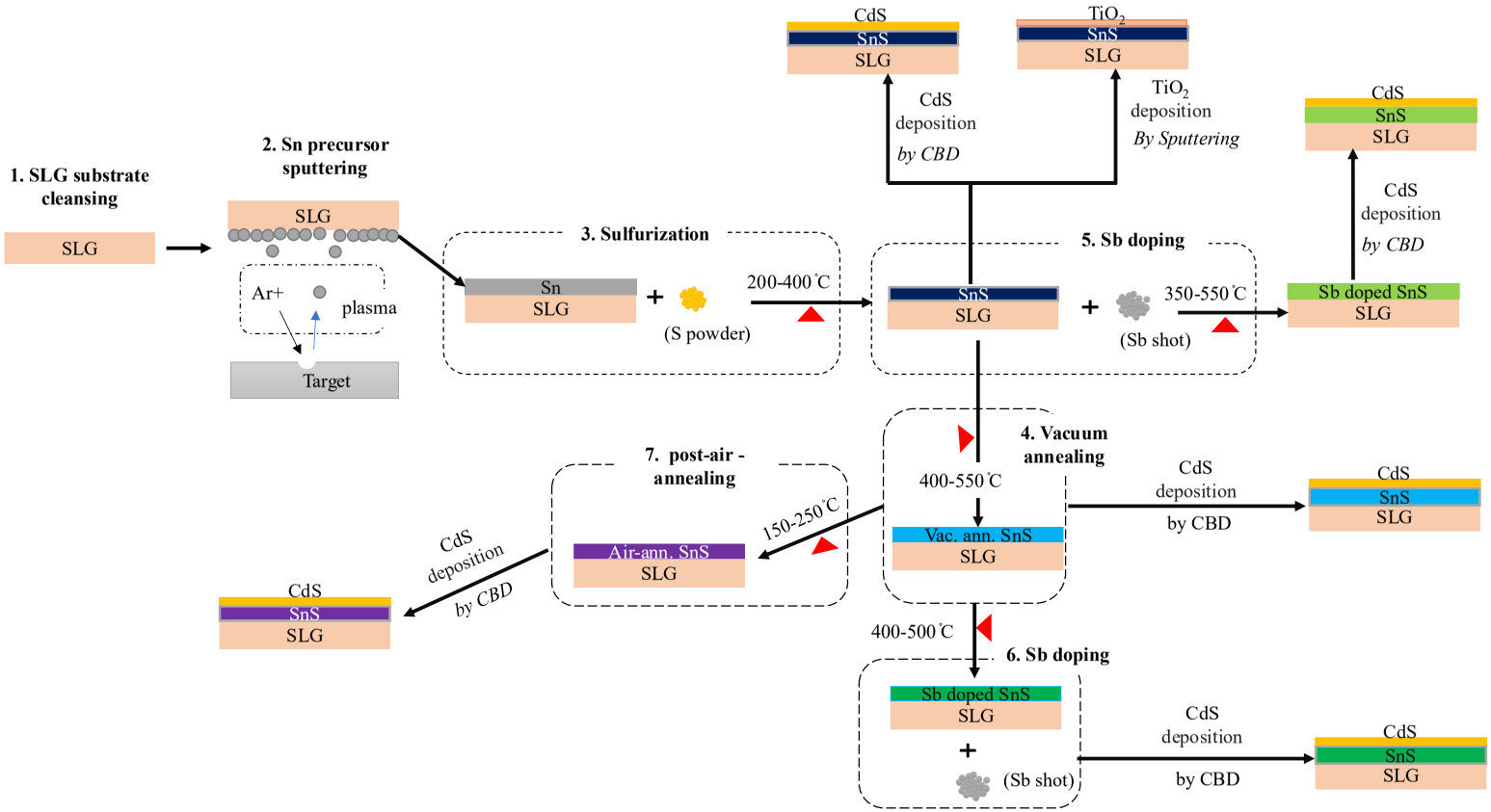

Figure 3-1 Fabrication process of SnS and its heterojunction with CdS and TiO_2 at different conditions.

3.2 Precursor sputtering

The cleaned substrates were fixed onto a substrate holder and loaded into RF magnetron sputtering apparatus (ULVAC: RFS-200). The vacuum chamber was evacuated first by an oil rotary pump and then by an oil diffusion pump and the rotary pump until the base pressure of 5×10^{-5} Pa was reached. Sn (purity:99.999%) was used as a metal target. RF sputtering was performed with an argon (Ar) plasma at a target to substrate distance of 20 cm and 100 W power. The sputtering rate was adjusted to 61 nm/min in 0.6 Pa of Ar atmosphere for a total sputtering duration of 14 min.

3.3 Precursor (Sn) sulfurization

The precursor was sulfurized with sulfur vapor inside an evacuated and sealed quartz ampoule. The sealed ampoule is illustrated in Fig. 3-3. The precursor (850 nm) and a measured quantity of sulfur powder were put inside a cleaned ampoule (inner diameter: 14 mm, length ≈ 10 cm). The amount of sulfur enclosed is in the ampoule is given in section 3.3.2 of Table 3-1.

3.3.1 Evacuation and sealing of ampoule

The glass ampoule with Sn precursor was evacuated from the open end with a diffusion pump is shown in Fig. 3-2. After evacuating it for about 30 minutes, the residual air pressure inside the ampoule was $\approx 3 \times 10^{-3}$ Pa. The glass ampoule was eventually sealed around the plug. The residual air inside a sealed ampoule is negligibly small and, therefore no apparent oxidation of the precursor.

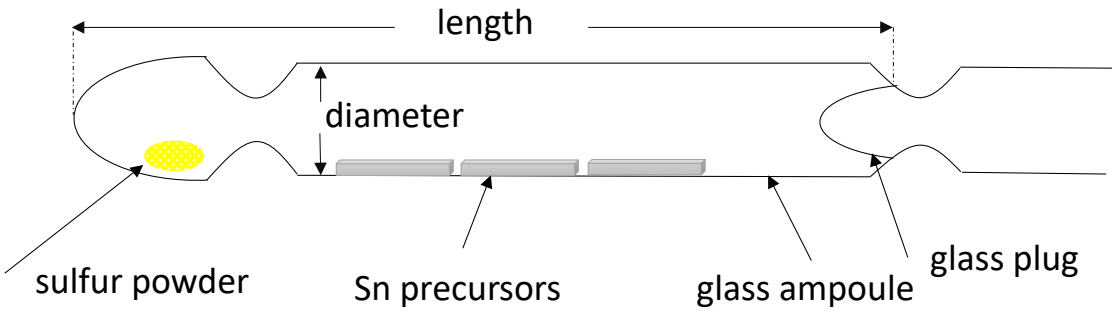

Figure 3-2 Evacuated and sealed glass ampoule containing a precursor and sulfur powder.

3.3.2 Calculation of quantity of Sulfur

The molar quantity of sulfur powder enclosed in the ampoule to control the vapor pressure during sulfurization was calculated from the ideal gas law:

$$n = \frac{PV}{RT} \tag{3-1}$$

where, P is the pressure in the ampoule, V is the ampoule volume in m^3, R is the universal gas constant, equal to 8.314 J/K-mol, and T the absolute temperature. The quantity of sulfur in grams (m_1) can be computed by multiplying the molar quantity by the molecular mass of sulfur vapor.

$$n = \frac{m_1}{M} \tag{3-1}$$

Here, m_1 is the mass (mg) of sulfur necessary to obtain a specific pressure P (Pa) in the ampoule, M is the molar mass (g/mol) of sulfur. Therefore, the final expression for the required mass of sulfur can be expressed as:

$$m_1 = \frac{PVM}{RT} \tag{3-2}$$

The amount of sulfur (m_2) required for the reaction is obtained from the Sn precursor thickness. The amount of sulfur ($m_1 + m_2$) necessary for growing SnS.

Table 3-1 The amount of sulfur ($m_1 + m_2$) enclosed in the ampoule at different sulfurization temperatures.

Sulfurization temperature (˚C)	Sulfur enclosed in the ampoule (mg)
200	12.59
250	12.52
300	10.64
400	9.27

3.3.3 Sn precursor sulfurization process and conditions

The ampoule was inserted into the carbon block and sulfurized by heating it in an infrared furnace, as shown in Fig. 3-3. The furnace consists of a heater connected to a ULVAC-1000 temperature controller. The controller was programmed with parameters (temperatures, reaction time, and PID values). Fig. 3-4 shows the sulfurization temperature versus sulfurization time of Sn precursor (Sn precursor thickness = 850 nm). The sulfurization

temperature is conducted in the range of 200 - 400 ˚C for the same annealing duration of 30 min.

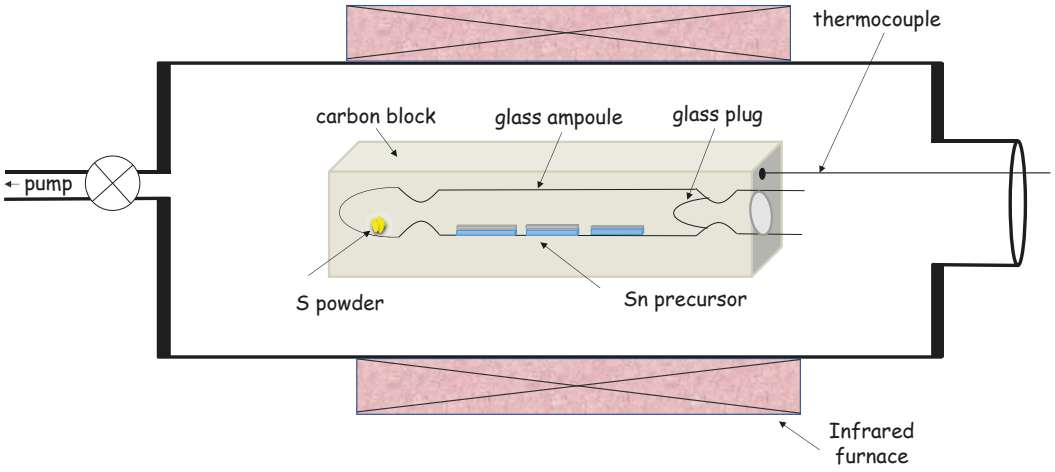

Figure 3-3 Schematics of the closed tube sulfurization process.

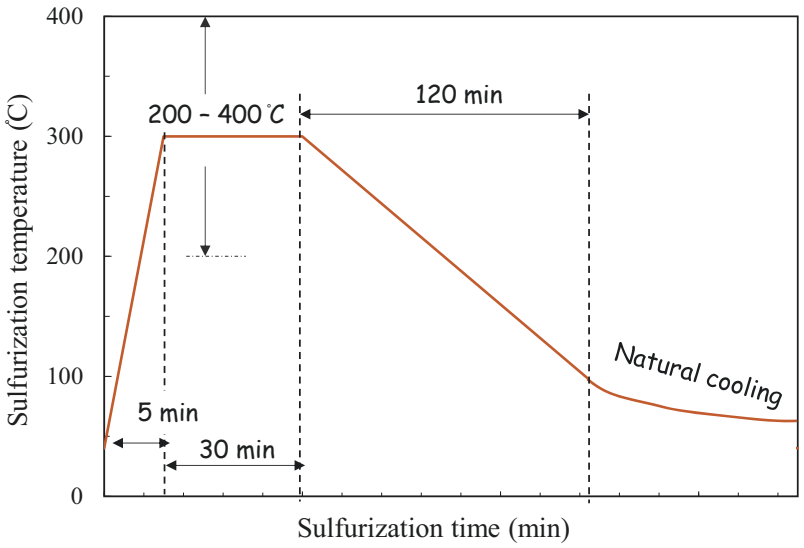

Figure 3-4 The temperature profile of sulfurization for SnS growth.

3.4 Vacuum annealing and post air annealing

In order to study the effect of vacuum annealing on SnS thin films grown at different sulfurization temperatures, vacuum annealing was carried out in the evacuated (3×10^{-3} Pa) and sealed ampoule. The vacuum annealing temperature was varied at the 400 - 550 ˚C for an annealing time of 30-120 min. Post-air-annealing (vacuum annealing followed by air annealing) was conducted at 150 - 250 ˚C for 30 min under atmospheric pressure.

3.5 Sb doping

Antimony ([Kr] $4d^{10}$ $5s^2$ $5p^3$) is a group V element in periodic table, and it is a potential *n*-dopant for SnS thin films. Sb can exist in trivalent (Sb^{3+}) and/or pentavalent (Sb^{5+}), expected to release electrons for *n*-type conductivity. And, as is introduced in chapter 1, both Sn and S in SnS have +2 and -2 oxidation states, respectively. Here, three possible Sb substitutional sites are possible, i.e., the Sn substitutional site (Sb_{Sn}), the antistites on S (Sb_S), and the interstitial site (Sb_i). Due to lower formation energy (ΔH) of Sb_{Sn} (~ 0.74 eV) than Sb_S (~ 1.5 eV), the incorporation of Sb into the Sn site is energetically favored.[1)] Fig. 3-5 shows the possible substitution of Sb at Sn sites as both Sb^{3+} and Sb^{5+} oxidation states are shown. When pentavalent Sb atom (Sb^{5+}) is replaced to bivalent Sn atom (Sn^{2+}), three electrons are released as a free electron to the SnS crystal lattice (Fig. 3-6 (a)). In the other case, when a bivalent Sn atom is replaced by a trivalent Sb atom (Sb^{+3}), one electron will be donated to the Sn lattice (Fig. 3-6. (b)). The maximum solubility of Sb in SnS lattice is reported in the range of 5-10%, depending on the growth conditions of SnS thin films.[2, 3)]

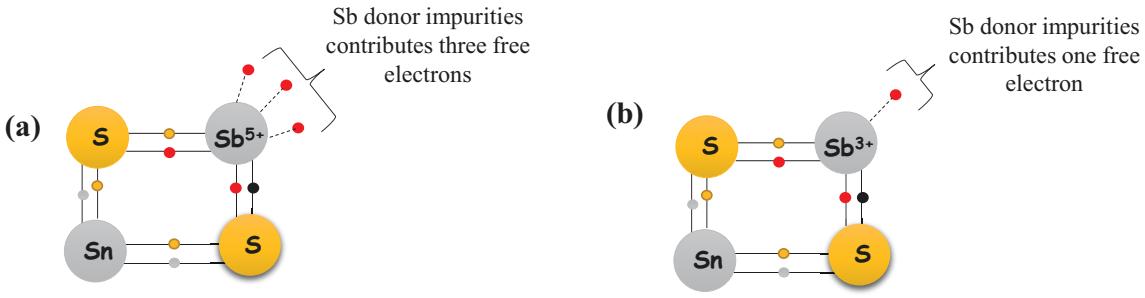

Figure 3-5 Schematic of Sb_{Sn} formation by (a) Sb^{5+} and (b) Sb^{3+} substitution in Sn^{2+}site.

Doping was done by the thermal diffusion method, where SnS thin films were heated under Sb ambience at the temperature range of 350 - 550 ˚C. This was done by enclosing 10 mg of Sb shot together with SnS thin films inside the ampoule, similar to that of sulfurization techniques discussed above in section 3.3.2. The ampoule was then set to a carbon block and then to the heating furnace. The amount of Sb diffused to the SnS thin films was then controlled by varying temperatures based on the Sb vapor pressure curve given in Fig 3-6. The vapor pressure is approximated for the shown pressure range according to:

$$P\ [mbar] = 10^{\left(A-\frac{B}{T[K]}\right)} \tag{3-3}$$

where, A = 11. 164 and B = 10510 are constants, T[k] is doping temperature.[4)] Using this equation, the vapor pressure of Sb at each doping temperature used in this work is calculated and listed in Table 3-2.

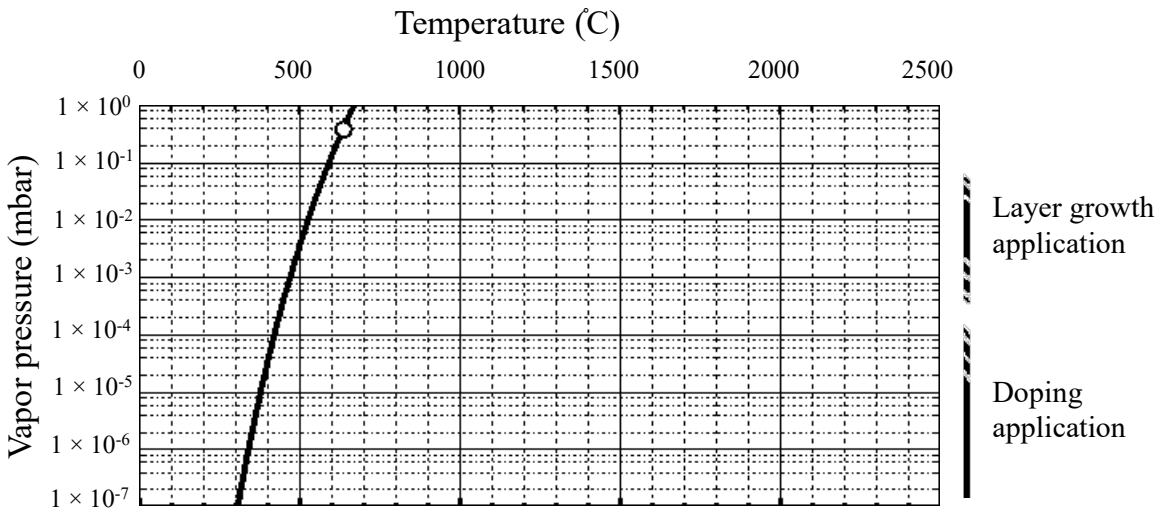

Figure 3-6 Vapor pressure curve of Sb.[4)]

Table 3-2 Doping temperature and the corresponding expected Sb vapor pressure

Doping temperature (˚C)	Expected vapor pressure (Pa)
350	6.71×10^{-6}
400	1.99×10^{-4}
500	8.88×10^{-4}
550	3.55×10^{-3}

3.6 Characterization techniques

3.6.1 Physical and compositional properties

The crystallinity of SnS thin films was characterized by X-ray diffraction (XRD, Rigaku RINT-2200, using the Cu Kα line wavelength λ = 1.54060 Å with Bragg-Brentano θ - 2θ geometry, current source of 20 mA, voltage source of 40 kV). Typically, the data was taken at 2θ intervals of 0.02° and a scanning speed of 4°/min. After that, the data extracted from the analysis were compared with the reference powder diffraction data to identify the films' appropriate crystal structure and orientation. The surface morphology of the SnS films was analyzed by field emission scanning electron microscope (FE-SEM, Hitachi, S-4100, 10 nA, and 15-kV). Raman spectroscopy analysis (COMET-3504, λ = 532 nm, a grid of 2400 cm^{-1}, slit width of 0.1 mm) was also used to identify secondary phases, which XRD did not clearly observe. An electron probe microanalyzer (EPMA, Shimadzu, EPMA-1610, beam current = 20 nA, acceleration voltage =20 kV, beam diameter =100 μm) was used to measure the bulk composition of SnS thin films. An X-ray photoelectron spectrometer (XPS, ULVAC-PHI, Quantra II, AlKα 1486.6 eV source) was used to evaluate the surface composition of grown samples and the energy band alignment of the SnS/CdS and SnS/TiO_2 heterojunctions. To determine the band alignments, the shallow buffer layers (~ 5 nm) of CdS and TiO_2 were grown on the SnS thin film by chemical bath deposition (CBD) and RF sputtering, respectively. The core level (CL) difference between the buffer layers (Cd $3d_{5/2}$ and Ti $2p_{3/2}$) and SnS thin films (Sn $3d_{5/2}$) were then determined from their simultaneously detected peaks at SnS/CdS and SnS/TiO_2 junctions, respectively.

3.6.2 Electrical properties

3.6.2.1 Resistivity and Van-der-Pauw method

In this thesis, the Van der Pauw technique was used to determine the resistivity of SnS thin films. Before directly proceeding to the resistivity measurement, the ohmic contact was confirmed by placing a Cu-metal four-point contact at the edges of the 5 mm × 5 mm size and ~ 1 μm thick SnS thin film. The characteristic resistances at the terminals of the SnS are determined from the applied dc currents and voltage across contacts, as depicted in Fig. 3-7. The bulk resistivity (ρ) is then determined from the sheet resistance (R_S) as:

$$\rho = R_S d \tag{3-4}$$

where d is the thickness of SnS thin film.

$R_{12,43} = V_{43}/I_{12}$

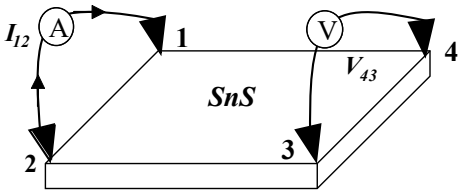

Figure 3-7 Schematics of a Van der Pauw experiment used to determine the characteristic resistances of SnS. This is a typical example to determination $R_{12,43}$ when a dc current I is applied across contact 1 and contact 2 and the voltage V_{43} across contact 4 and contact 3.

3.6.2.2 Hall measurement

In this work, TOYO corporation of 8403 series AC/DC Hall effect measurement system is used to determine electrical properties of SnS such as resistivity, hole concentration, mobility, and conductivity type.

Fig. 3-8 demonstrated how the Hall effect is created when a magnetic field (B_z) is applied perpendicular to a current (I_x) flowing in SnS thin film samples. Combining a magnetic field and a flowing current causes a separation of charges and accumulates at the opposite edge of the SnS sample. This build-up of the charges creates an electric field (E_y) perpendicular to both the current and the magnetic field. This leads to a potential difference across the material, which is known as Hall voltage (V_H)and can be determined as,

$$V_H = \frac{IB}{qnt} = R_H \frac{IB}{t} \tag{3-5}$$

where q is the elementary charge (1.602×10^{-19} coulombs), n is the carrier density, t is the thickness of the SnS sample, and R_H is the Hall coefficient. If the Hall voltage is positive/negative, the carriers in the material are holes/electrons. The Hall coefficient and resistivity are used to determine the carrier density (n) and mobility (μ) of a material by the following equations.

$$n = \frac{1}{qR_H} \tag{3-6}$$

$$\mu = \frac{R_H}{\rho} \tag{3-7}$$

The temperature-dependent electrical resistivity was also conducted at a 100-300K temperature range using the Model 84016 Closed Cycle Refrigerator (CCR) integrated into the Hall measurement system. The data were then fitted to the Arrhenius equation below to determine the activation energy of SnS.

$$\rho = \rho_0 e^{\left(\frac{-E_a}{KT}\right)} \tag{3-8}$$

Where $K = 8.617\ x\ 10^{-5}$ eV K^{-1} is Boltzmann's constant and E_a is the activation energy.[5)]

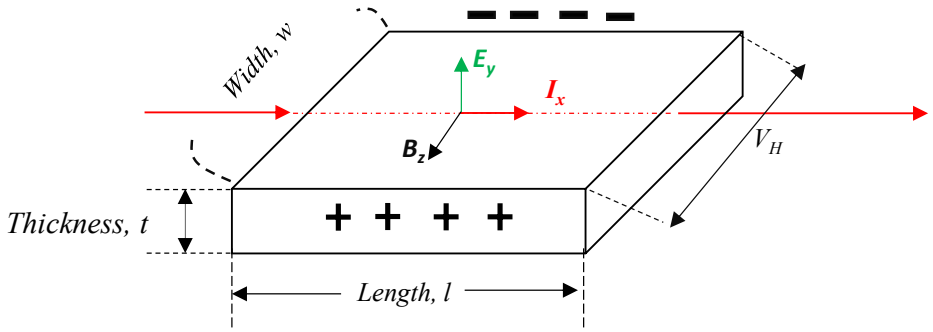

Figure 3-8 Geometry of the Hall effect in p-type SnS.

3.6.3 Optical properties

3.6.3.1 Transmittance, reflectance, and absorption coefficient

When a photon with an energy of hv (h = Planck's constant= 6.626 x 10^{-34} J-s, v the frequency) is incident on a semiconductor, an electron in the valence band may absorb the photon, gain the energy hv, and move to an unoccupied conduction band state if hv is larger than the band gap energy, E_g. In other words, the semiconductor appears to be transparent for photons of energies smaller than E_g and starts absorbing photons with larger energies.

Consequently, the transmission (or absorption) spectrum can be used to determine the band gap of the semiconductor.

Fig 3-9 illustrates the reflection, absorption, and transmission of an incident light beam of intensity I_0 by a thin film of width t. As the incoming light strikes the film surface, a portion of it (RI_0, R = reflection coefficient) gets reflected due to a mismatch between air's refractive indices and the film. The remaining light intensity ($(1-R)\ I_0$) gets exponentially attenuated inside the film due to absorption. On passing the distance t, its final intensity is equal to $(1-R)\ I_0 e^{-\alpha t}$, where α, known as the absorption coefficient, is the rate at which the beam gets attenuated inside the material. Considering the reflection at the rear interface also, the intensity of the transmitted beam is equal to $(1-R)^2\ I_0 e^{-\alpha t}$. Therefore, the transmission coefficient, T, which is the ratio of the intensity of the transmitted beam to that of the incident beam, is equal to $(1-R)^2 e^{-\alpha t}$. The transmittance (T) and reflectance (R) are directly measured using a thickness of a known sample, the thickness of SnS in this case (t), which is ~1 μm. Therefore, the absorption coefficient can be computed as,

$$\alpha = \frac{1}{t} ln \left[\frac{(1-R)^2}{T} \right] \tag{3-19}$$

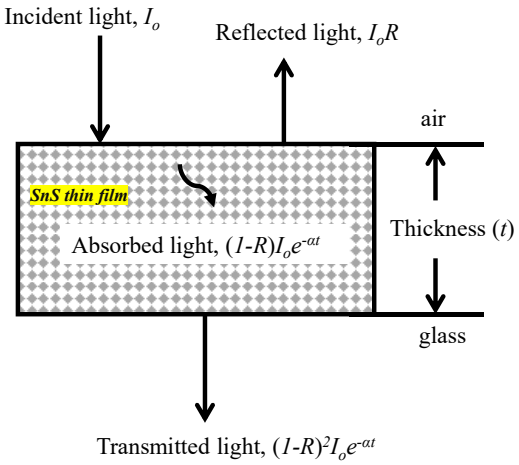

Figure 3-9 illustration of reflection, absorption, and transmission of incident light beam by a SnS thin film.

In this study, transmittance and reflectance spectra of SnS thin-film were obtained using a JASCO Corporation V-770 spectrophotometer. At first, bare soda-lime glass (SLG) substrates identical to that used as an SnS thin film sample substrate was placed in the monochromatic beam's path, and transmitted intensities over the whole measurement range (usually 200 – 2000 nm) were measured. This baseline correction step was necessary for the system calibration and to ensure accurate quantification of the measured data. The bare SLG substrate was replaced with the SnS thin film sample in the next step. Similarly, the procedure was repeated to measure reflectance. Once the reflectance and transmittance spectra were measured, a plot of $(\alpha hv)^2$ versus hv was prepared. The hv (in eV) for each wavelength λ (in nm) was computed from the relation,

$$hv = \frac{1240}{\lambda} \quad (3\text{-}10)$$

3.6.3.2 Estimation of band gap

Near the absorption edge, the absorption coefficient can be expressed as:

$$\alpha = (hv - E_g)^{1/2} \quad (3\text{-}11)$$

where hv and E_g are the photon energy and band gap energy, respectively. For direct band gap materials, transitions mainly occur between two bands of the same k value (Fig. 3-10 (a)). The $((\alpha hv)^2)$ vs. hv graph is a straight line near the absorption edge, and extrapolating the curve to the hv-axis gives us the band gap energy. For indirect transitions, Fig.3-10 (b) phonons are involved in order to conserve momentum. In these transitions, phonons (with energy E_p) are either absorbed or emitted, and the absorption coefficient is modified to:

$$\alpha = (hv - E_g \pm E_p)^2 \quad (3\text{-}12)$$

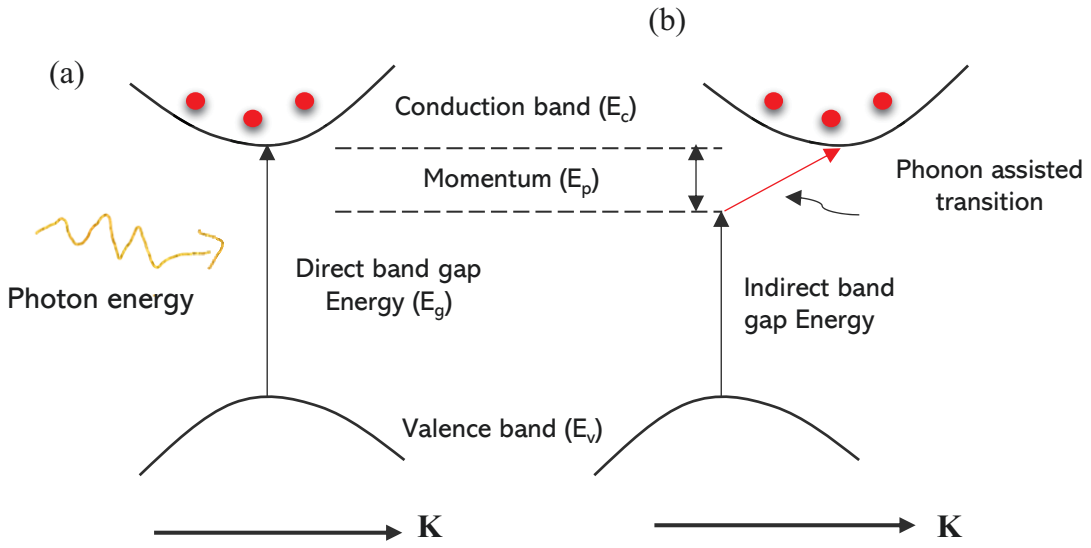

Figure 3-10 Optical transitions; (a) direct transitions and (b) indirect transition involving photon emission/absorption.

Reference

1. Z. Xiao, Fan-Yong Ran, H. Hosono, and T. Kamiya, *"Route to n-type doping in SnS",* Appl. Phys. Lett. **106**, 152103 (2015).
2. P. Sinsermsuksakul, R. Chakraborty, S. B. Kim, S. M. Heald, T. Buonassisi, and R. G. Gordon, *"Antimony-Doped Tin (II) Sulfide Thin Films",* Chem. Mater. **24**, 4556 −4562 (2012).
3. K. S. Kumar, C. Manoharan, S. Dhanapandian, and A. G. Manohari, *"Effect of Sb dopant on the structural, optical and electrical properties of SnS thin films by spray pyrolysis technique",* Spectrochim. Acta A Mol. Biomol. Spectrosc. **115**, 840–844 (2013).
4. https://www.mbe-komponenten.de/selection-guide/element/sb.php, Dr. Eberl, MBE komponenten (Dec. 2021).
5. K. J. Laidler, *"The development of Arrhenius equation"*, J Chem Educ. **61,** 495 (1984).

Chapter 4

Optimization of SnS growth parameters

Introduction

This chapter studies the effect of sulfurization temperature, vacuum annealing, and post-air-annealing on SnS thin films. Sulfurization temperature was varied in the 200 - 400 ˚C for the same reaction time of 30 mins. Both the as-grown SnS samples at 250 ˚C and 300 ˚C were vacuum annealed at 400 - 550 ˚C for an annealing time of 30-120 min. Post-air-annealing (vacuum annealing of as-grown SnS thin film followed by air annealing) was conducted under atmospheric pressure.

4.1 Effect of Sulfurization Temperature

SnS films were grown at the sulfurization temperature range of 200 - 400 ˚C for 30 min. The XRD patterns in Fig. 4-1 show that all the samples grown are in polycrystalline nature. The films grown at 200 ˚C showed both Sn and SnS peaks, indicating the incomplete sulfurization of the Sn precursor layer at this temperature. When the sulfurization temperature was increased to 250 ˚C, all peaks which are closely matched to orthorhombic SnS are formed. An intense and narrow peak at the (040) plane indicates the improvement in crystallinity of SnS. For sulfurization temperature greater than 300 ˚C, the intensity of SnS peak at (040) plan is decreased, and additional peaks which belong to the hexagonal SnS_2 are observed.

This shows that the formation of SnS_2 is preferable at a higher sulfurization temperature.[1, 2)] The decrease in intensity of (040) peak for sulfurization temperature greater than 300 ˚C could be due to the deterioration in crystallinity of orthorhombic SnS. From the results, we can conclude that 250 ˚C is an optimum temperature to form a pure phase orthorhombic SnS.

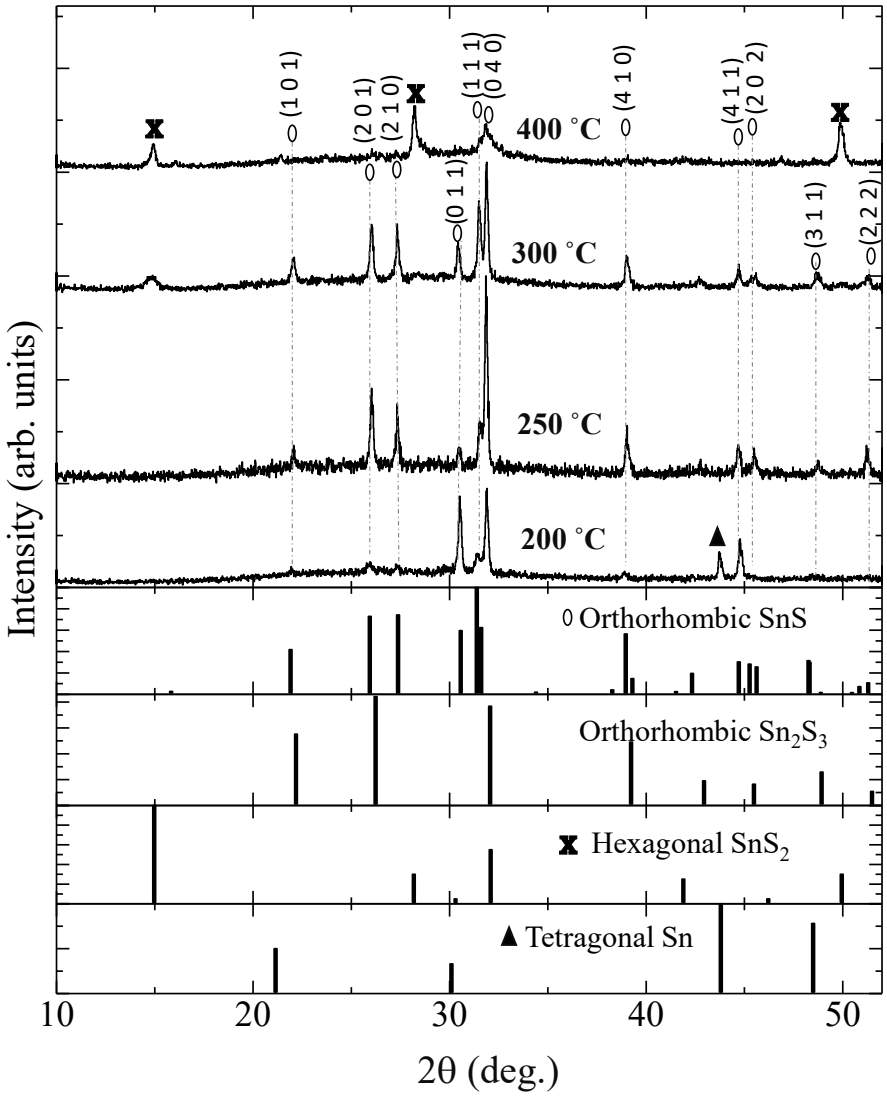

Figure 4-1 XRD patterns of SnS grown at 200 ˚C, 250 ˚C, 300 ˚C, and 400 ˚C.

From the Raman spectra in Fig. 4-2, SnS thin film grown at sulfurization temperature of 250 ˚C has Raman vibration modes at 96 cm^{-1}, 104 cm^{-1}, 171 cm^{-1}, 192 cm^{-1}, and 220 cm^{-1}, which belong to orthorhombic SnS phase.[3-6] Raman peaks for samples grown at 250 ˚C were found to be the most intense and sharpest among the other samples. This result indicates that the crystalline quality of the samples prepared at 250 ˚C is superior. However, the sample grown at 300 ˚C has vibration modes related to the secondary phases (Sn_2S_3 at 71 cm^{-1} and SnS_2 at 312 cm^{-1}).[7] When the temperature is raised to 400 ˚C, only the modes related to SnS2 were observed. This contradictory result from the XRD measurement could be due to the formation of the SnS_2 layer at the surface and can easily be detected within the penetration depth of Raman laser, whereas SnS is not.[1] It is generally observed that the optimum temperature for forming a pure phase SnS depends on different parameters such as temperature, reaction time, pressure, and deposition techniques. Reddy *et al.* have grown thin films orthorhombic SnS thin films by sulfurization of sputtered Sn precursor (300 nm) at a temperature range of 150 - 450 ˚C for a fixed sulfurization time of 120 min.[8] The XRD results of films grown at 150 - 200 ˚C showed the existence of SnS and Sn_2S_3 phases along with un-reacted Sn and S. As the sulfurization temperature was increased to 250 ˚C, only SnS and Sn_2S_3 phases were identified, while a pure phase SnS was observed at the sulfurization temperature range of 300 - 350 ˚C. For temperatures greater than 400 ˚C, the SnS_2 phase was obtained in addition to that of SnS.

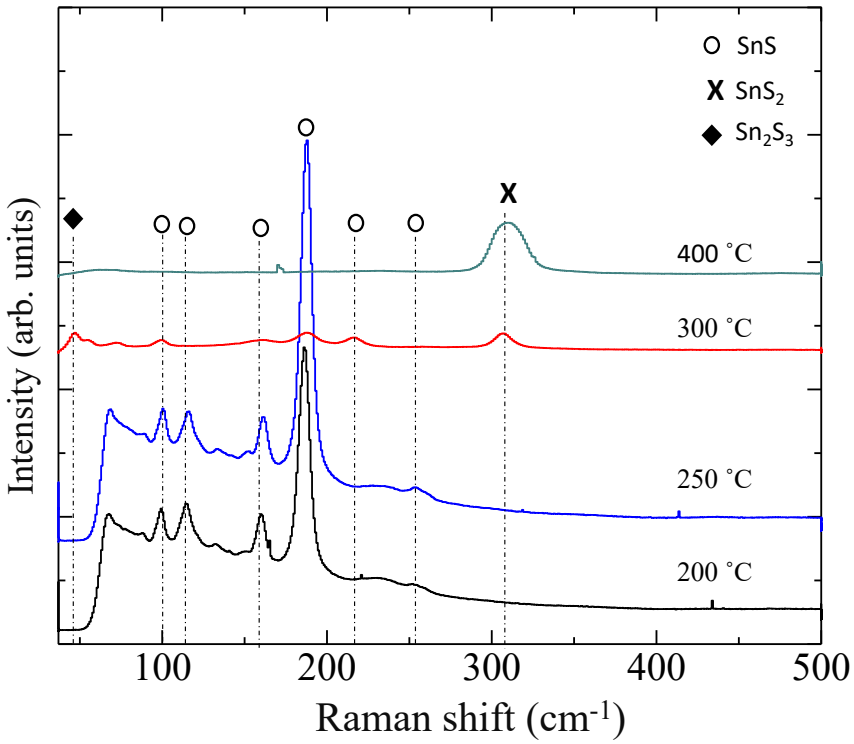

Figure 4-2 Raman spectra of SnS grown at 200 ℃, 250 ℃, 300 ℃, and 400 ℃.

Fig. 4.3 shows the surface morphology of the thin films sulfurized at different temperatures. The surface of the SnS film grown at 200 ˚C is composed of agglomerates of small grains (Fig. 4.3(a)). As sulfurization temperature is increased to 250 ˚C, a homogeneous surface with a slightly larger grain was obtained (Fig. 4.3(b)). The surface morphology of a sample grown at 300 ˚C is not significantly changed compared with that of 250 ˚C (Fig. 4.3(c)). However, as the sulfurization temperature was increased to 400 ˚C, the platelet like structure which is attributed to hexagonal type SnS_2 phase are formed shown in Fig. 4-3(d).[9, 10]

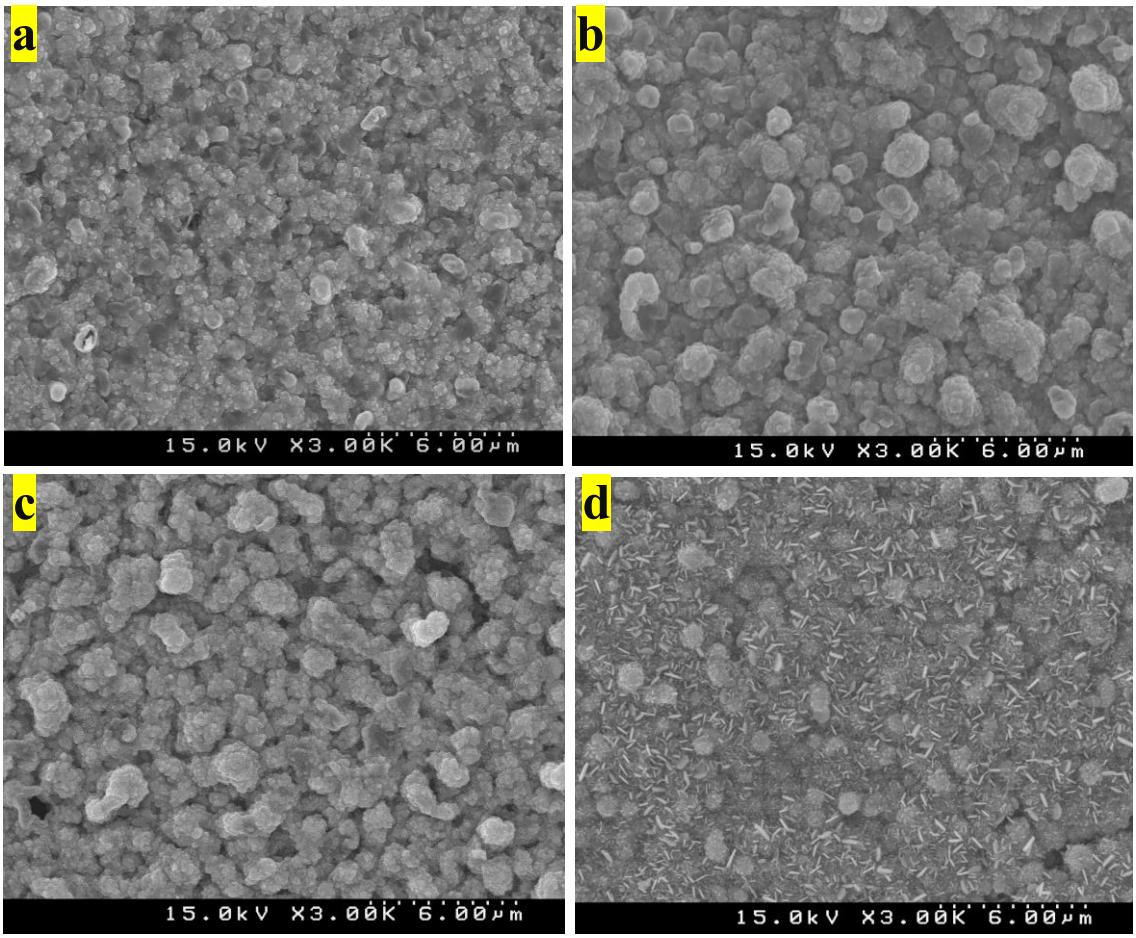

Figure 4-3 Surface morphology of samples grown at (a) 200 ˚C, (b) 250 ˚C, (c) 300 ˚C, and (d) 400 ˚C.

The S/Sn ratio based on the EPMA measurement of the thin films prepared at various temperatures is shown in Fig. 4-4. The S/Sn ratio of a sample grown at 200 ˚C is 0.82, which shows an Sn-rich composition. As the sulfurization temperature increases to 250 ˚C, an S/Sn ratio of 1.03 near stoichiometry is obtained. This indicates the formation of a pure phase SnS which is also in good agreement with the XRD and Raman results. At 300 ˚C, the S/Sn ratio increases to 1.28, indicating that more sulfur atoms diffuse to Sn precursor at higher sulfurization temperature, and the formation of sulfur-rich phases is preferable. However, as the sulfurization temperature was further increased to 400 ˚C, the S/Sn ratio of 2.0 was obtained, which indicates the formation of the SnS_2 phase.

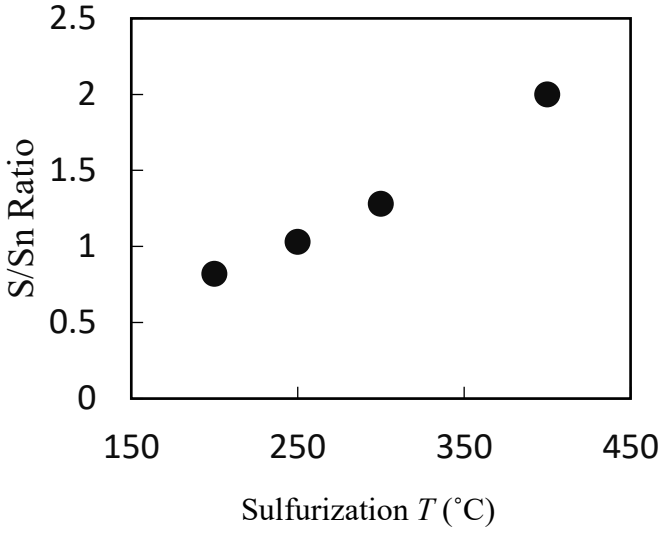

Figure 4-4 S/Sn ratio of samples grown at different temperature.

The electrical properties of samples grown at different sulfurization temperatures are given in Table 4-1. The electrical properties of a sample grown at 200 ˚C were not measured. The electrical resistivity and carrier concentration of a sample grown at 250 ˚C are 9.5×10^{1} Ω cm and 1.3×10^{16} cm^{-3}, respectively. These values are increased and decreased to 1.1×10^{2} Ω cm and 4.1×10^{15} cm^{-3}, respectively, for the sample grown at sulfurization temperature of 300 ˚C. The increase in resistivity and decrease in carrier concentration of a sample grown at 300 ˚C could be due to the existence of high resistive secondary phases (i.e., Sn_2S_3 and SnS_2). Hall measurements confirmed that the films were grown at 250 and 300 ˚C showed *p*-type conductivity. Since the electrical resistivity of the sample grown at 400 ˚C was too high, its electrical properties could not be determined.

Table 4-1 Electrical properties of samples grown at different sulfurization temperatures.

Parameters	Sulfurization temperature (˚C)			
	200	250	300	400
Carrier concentration [cm^{-3}]	Not measured	1.3×10^{16}	4.1×10^{15}	High resistance (Beyond the limit of measuring instrument)
Resistivity [Ω·cm]		9.5×10^{1}	1.1×10^{2}	
Mobility [$cm^2V^{-1}s^{-1}$]		5.01	13.9	

The plot of $(\alpha hv)^2$ *vs*. hv for SnS thin films prepared at 250 - 400 ˚C is shown in Fig. 4-5. The optical properties of a sample grown at 200 ˚C were not measured. The energy bandgap was determined by extrapolating the straight portion of the plot on the energy axis. The estimated bandgap for a film grown at 250 ˚C has a direct bandgap of 1.2 eV. At 300 ˚C, two absorption edges with a bandgap of 1.2 eV and 1.4 eV were observed. The wider bandgap might be due to the presence of the Sn_2S_3 phase.[11] The films grown at 400 ˚C have a wider energy bandgap of 2.3 eV, which indicates the formation of SnS_2 with an optical bandgap of 2.2 - 2.4 eV. [12, 13]

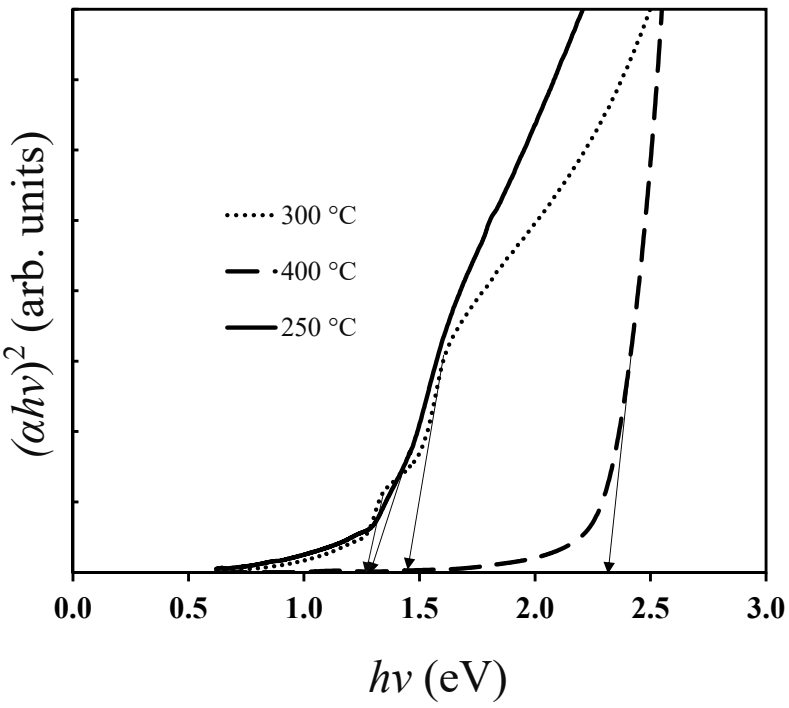

Figure 4-5 $(\alpha hv)^2$ versus hv plots of samples grown at 250 ˚C, 300 ˚C, and 400 ˚C.

4.2 Effect of vacuum annealing on SnS grown at different temperatures

This section discusses the effect of vacuum annealing on SnS thin films grown at a sulfurization temperature of 300 ˚C and 250 ˚C are discussed.

4.2.1 Effect of vacuum annealing on SnS grown at 300 ˚C

To understand the effect of annealing on mixed-phase SnS, a sample grown at 300 ˚C was annealed at a temperature range of 400-500 ˚C for 30 min, and its properties were examined. Fig. 4-6 depicts the X-ray diffraction patterns of as-grown and vacuum (3×10^{-3} Pa) annealed samples. From the XRD result, the diffraction peaks belonging to the hexagonal SnS_2 phase were observed along with orthorhombic SnS in the as-grown thin film and the one annealed at 400 ˚C. On the other hand, the impurity phases vanished for the thin films annealed at 500 ˚C. Raman spectra of as-grown and vacuum annealed thin films at different temperatures are shown in Fig. 4-7. From the Raman spectra, peaks that belong to Sn_2S_3 and SnS_2 were detected in the as-grown samples. After annealing at 400 ˚C, peaks due to Sn_2S_3 were not observed, but a peek at 312 cm^{-1} remains, which belongs to SnS_2. In the case of the sample annealed at 500 ˚C, the existence of neither SnS_2 nor Sn_2S_3 phases was detected. This result confirms the sulfur excess phases such as Sn_2S_3 and SnS_2 are decomposed so that only the orthorhombic SnS phase is left after annealing.

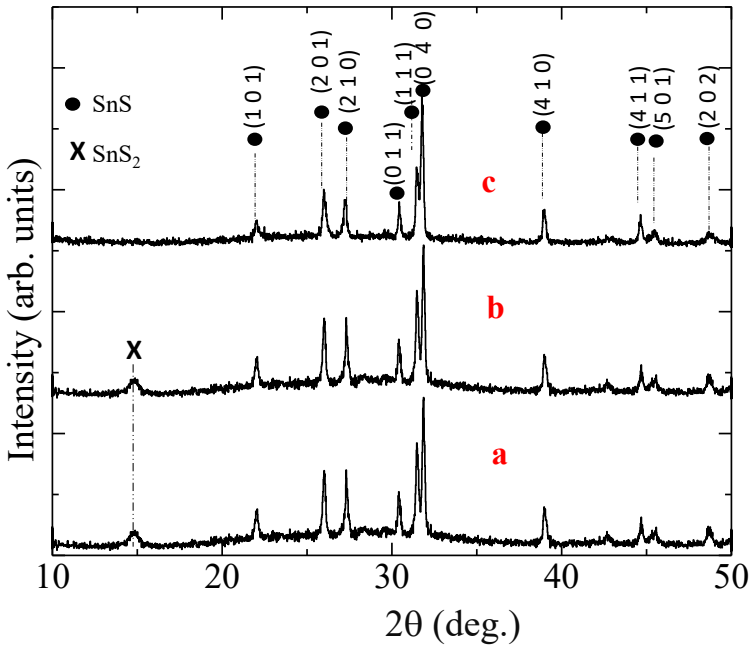

Figure 4-6 XRD spectra of (a) as-grown SnS at 300 ℃, (b) vacuum annealed at 400 ℃, and (c) 500 ℃.

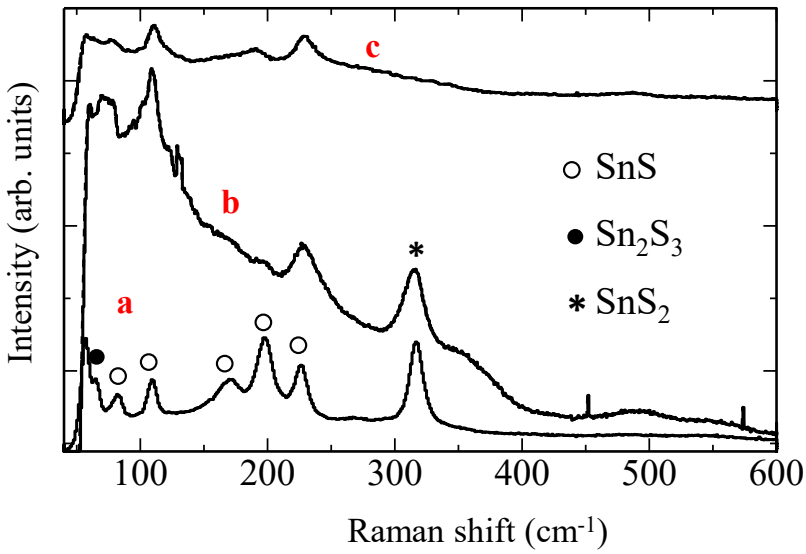

Figure 4-7 Raman spectra of (a) as-grown SnS at 300 ℃, (b) vacuum annealed at 400 ℃, and (c) 500 ℃.

SEM images of as-grown and vacuum annealed samples are shown in Figs. 4-8(a-c). The surface morphology of as-grown and a film annealed at 400 ˚C has a similar appearance. However, when the annealing temperature was increased to 500 ˚C, a thin film composed of closely packed crystal grains was achieved.

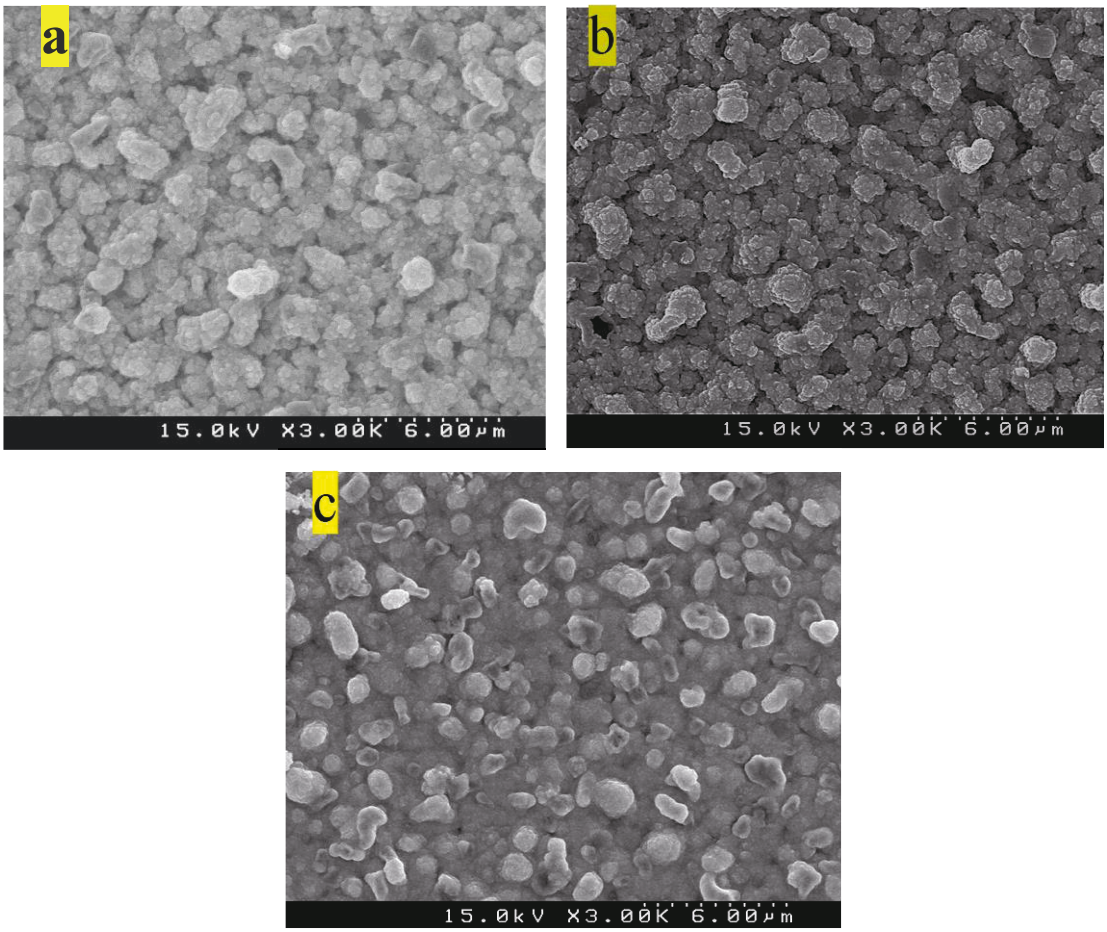

Figure 4- 8 SEM images of (a) as-grown SnS at 300 ˚C, (b) vacuum annealed at 400 ˚C, and (c) 500 ˚C.

Fig. 4-9 shows the S/Sn ratio based on data from EPMA measurement. The S/Sn ratio for the as-grown film was 1.28, and it was decreased to 1.08 after annealing at 500 ˚C. This decrease in the composition of the vacuum annealed samples could be due to the decomposition of sulfur-rich secondary phases such as Sn_2S_3 and SnS_2, which was also confirmed by the XRD and Raman analysis discussed above.

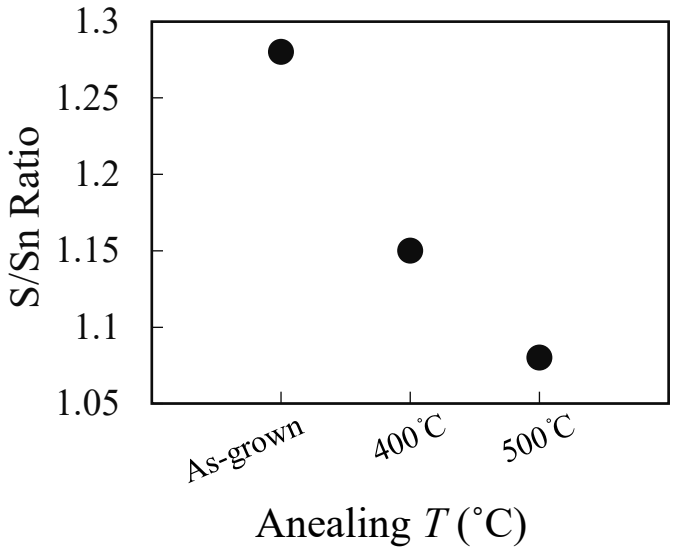

Figure 4-9 S/Sn ratio of as-grown SnS at 300 ̊C, vacuum annealed at 400 ̊C, and vacuum annealed at 500 ̊C.

The electrical resistivity, mobility, and hole concentration of as-grown SnS were 1.1 × 10^2 Ω cm, 13.9 $cm^2V^{-1}s^{-1}$, and 4.09 × 10^{15} $cm^{-3,}$ as shown in Table 4-2. The hole concentration was increased to 1.15 × 10^{18} cm^{-3}, while resistivity was decreased to 3.7 × 10^1 Ω cm after annealing at 500 ˚C. The decrease in resistivity of annealed films could be due to the decomposition of *n*-type conductive secondary phases such as SnS_2 and Sn_2S_3, resulting in the formation of Sn-defect SnS. The mobility of annealed samples was decreased to about 2 $cm^2V^{-1}s^{-1}$, which could be due to the formation of poor crystallinity SnS thin film.

Table 4-2 Hall effect measurement results of as-grown, vacuum annealed at 400 ˚C and 500 ˚C SnS thin films.

Annealing temperature (˚C)	Carrier concentration [cm^{-3}]	Resistivity [Ω·cm]	Mobility [$cm^2V^{-1}s^{-1}$]	Conductivity type
As-grown	4.09 × 10^{15}	1.10 ×10^2	13.87	*p*
400	1.20 × 10^{16}	7.50 × 10^1	1.84	*p*
500	1.15 × 10^{18}	3.70 × 10^1	1.63	*p*

Fig. 4-10 shows activation energy of 0.20 eV for the as-grown and vacuum annealed sample at 400 ˚C evaluated from Arrhenius (Eq.3-8 in chapter 3). This defect level could be attributed to the acceptor states from Sn vacancy. The value of activation energy was slightly increased to 0.21 eV after the as-grown sample was annealed at 500 ˚C. The change in activation energy could be related to the change in carrier density of the samples; however, due to the existence of secondary impurity phases such as n-SnS_2 and n-Sn_2S_3, it is difficult to distinguish its origin clearly. Earlier reports on SnS grown by different deposition techniques also claim the presence of a deep acceptor level in the range 0.20 - 0.65 eV.[14-18] In general, deep acceptor/donor level within the bandgap of a semiconductor material can lead to a recombination effect, while ones that form shallow defect states are leading to relative benignity upon their formation.[19,20]

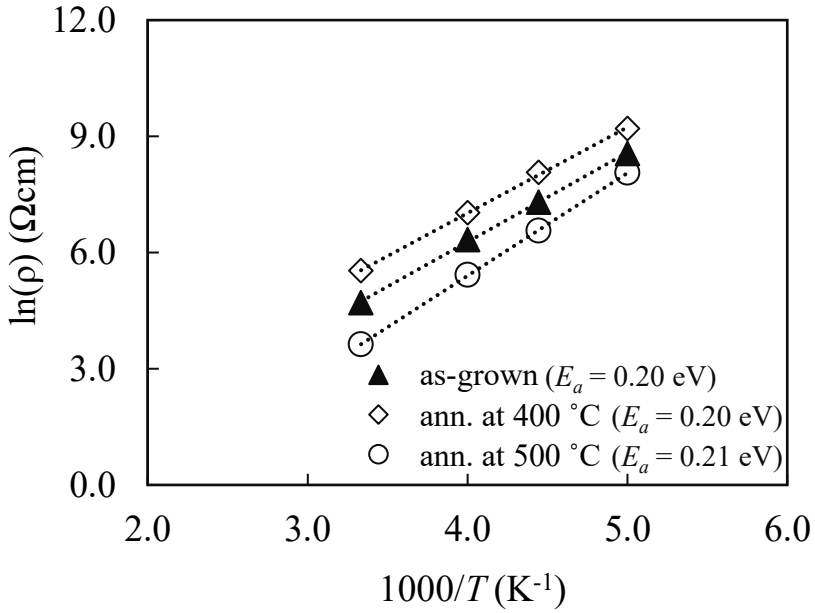

Figure 4-10 Activation energy of as-grown SnS at 300℃, vacuum annealed at 400℃, and vacuum annealed at 500℃.

Fig. 4-11 shows the plot of $(\alpha hv)^2$ against photon energy hv for as-grown and vacuum annealed SnS films. In the as-grown SnS, there are two absorption edges at around 1.2 eV and 1.4 eV, which correspond to SnS and Sn_2S_3, respectively. When the annealing temperature was increased to 500 ˚C, we can estimate the bandgap of the film is about 1.2 eV because the portion of the curve, which is extrapolated to a wide bandgap, is relatively diminishing. This result also supports the decomposition of secondary phases such as Sn_2S_3, consistent with the Raman and XRD analyses.

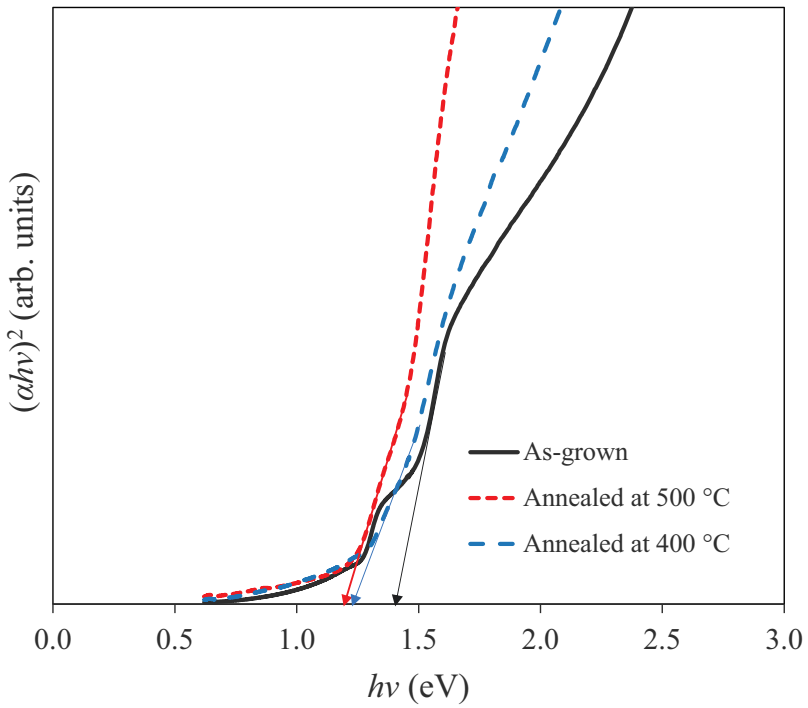

Figure 4-11 $(\alpha hv)^2$ versus hv plots of as-grown SnS at 300 ˚C, vacuum annealed 400 ˚C, and vacuum annealed at 500 ˚C.

4.2.2 Effect of vacuum annealing on SnS grown at 250˚C

The annealing conditions and assignment of the samples for the as-grown SnS thin film at 250 ˚C are given in the following Table 4-3.

Table 4-3. Details of samples grown at different conditions.

Sample	Vacuum annealing temperature (˚C)	Post-air-annealing temperature (˚C)
As-grown	-	-
V550	550	-
V450	450	-
V400	400	-
VA400-150	400	150
VA400-200	400	200
VA400-250	400	250

4.2.3 Effect of annealing temperature

The XRD patterns of the as-grown and vacuum annealed at different temperatures are shown in Fig. 4-12. All the SnS thin films exhibit the diffraction peaks of the orthorhombic SnS structure as indicated by the Miller indexes.[21-23] In Fig. 4-12, the most

prominent peak of the (040) plane is observed at $2\theta = 31.87^{\circ}$ with full width at half maximum (FWHM) of 0.17°. Another main diffraction peak assigned for the (111) plane is detected at $2\theta = 31.51^{\circ}$ with an FWHM of 0.2°. In the case of sample V400, which is vacuum annealed at 400 ˚C, the intensities of all peaks are significantly increased, except that of the (040) plane. The most prominent peak is changed to (111) plane observed at $2\theta = 31.51^{\circ}$, and the FWHM is reduced to 0.12°, indicating crystalline quality improvement. The intensity ratio of (111)/(040) of the as-grown sample is 0.44, while that of V400 is increased to 1.7, which is larger than that of the standard powder diffraction ratio of 1.46. This result indicates that the as-grown film is oriented in the (040) plane, while that of V400 is oriented in the (111) plane. Similarly, the formation of thin films with different orientations such as (040) and (111) planes depending on the preparation techniques and conditions has been reported.[24-27] As vacuum annealing temperature was further increased to 450 ˚C, the peak patterns and intensities were not significantly changed compared to that of V400. However, the FWHM (at $2\theta = 31.51^{\circ}$) of vacuum annealed sample at 550 ˚C is increased to 0.19°, and the intensity of all peaks are decreased, which indicates the deterioration in crystallinity of SnS films. The intensity ratio of (111)/(040) is 0.80, which suggests that the film is oriented in the (040) plane again.

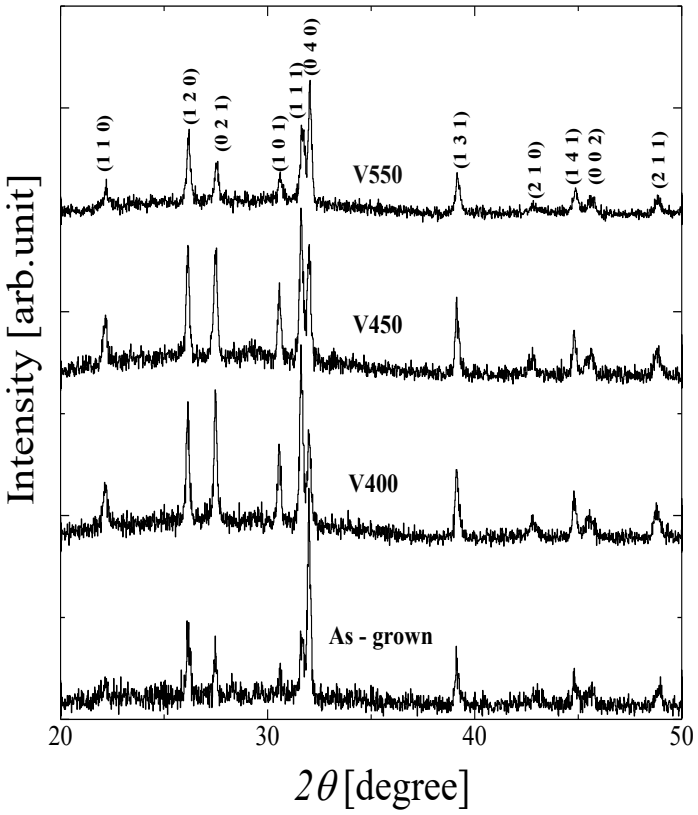

Figure 4-12 XRD patterns of as-grown, vacuum annealed at 400 ˚C (V400), 450 ˚C (V450), and 550 ˚C (V550) SnS thin films.

Fig. 4-13 shows the surface morphologies of the SnS thin films for as-grown, vacuum annealed at 400 ˚C (V400), 450 ˚C (V450), and 550 ˚C (V550) samples. The as-grown sample consists of densely agglomerated small grains. In the case of sample V400, the grain size is dramatically increased to 1.6 μm. The increase in grain size of SnS after vacuum annealing could be due to the recrystallization effect. This makes the film structure dense and compact with better orientation and a good connection between the grains, decreasing the possibility

of pinhole formation. When the annealing temperature is further increased to 450 ˚C (V450), more densely packed grains compared to that of V400 are obtained. This could be due to the grain coalescence and reorganization that could occur at higher annealing temperatures (450 ˚C). However, a decrease in grain size with serious voids across the surface was observed for the sample annealed at 550 ˚C (V550). This formation of voids could be because of the re-evaporation of the SnS phase from the surface at a higher temperature. Therefore, to obtain SnS thin film with large grain size and improved surface morphology, SnS thin films should be vacuum annealed at a temperature range of 400-450 ˚C.

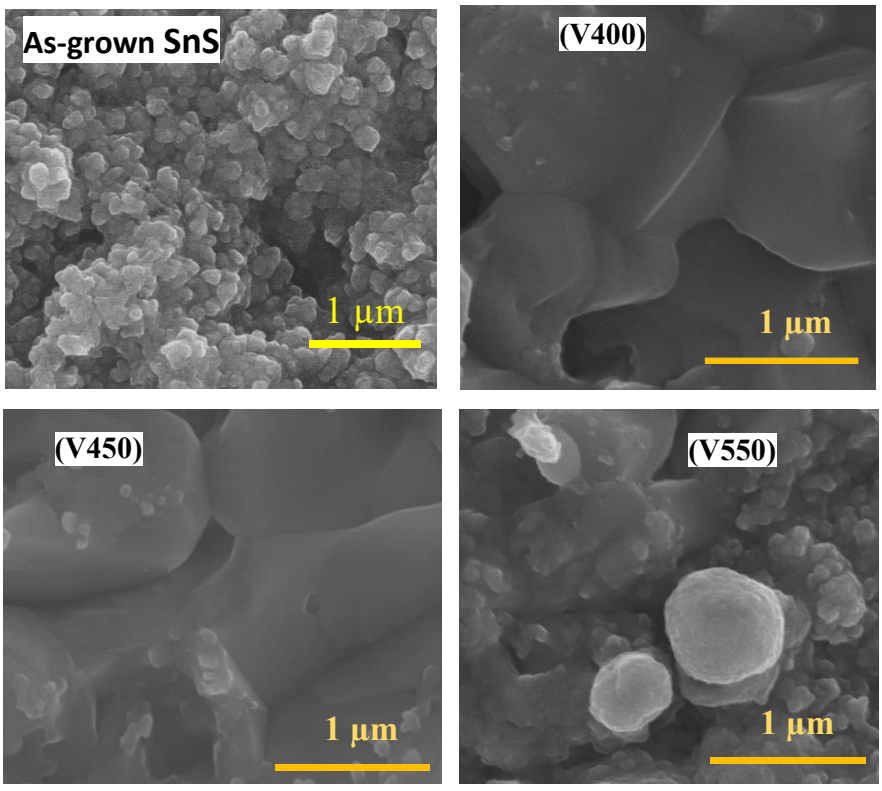

Figure 4-13 SEM images of as-grown, vacuum annealed at 400 ˚C (V400), 450 ˚C (V450), and 550 ˚C (V550) SnS samples.

The bulk and surface chemical composition (S/Sn) of as-grown, vacuum annealing, and post-air annealed samples was investigated by EPMA and XPS, respectively. From the EPMA analysis in Fig. 4-14, the bulk S/Sn ratio of 1.04 is obtained for the as-grown sample. The XPS analysis observed a sulfur-rich surface composition (S/Sn ~ 1.22) in the as-grown sample. The higher S/Sn ratio on the surface of the as-grown sample indicates the existence of sulfur excess phases. 9.31% of oxygen and 19.81% of carbon were also observed at the surface of the as-grown sample, which could be due to unintended ambience contamination. In the case of samples with vacuum annealing, no noticeable change in the bulk S/Sn ratio is observed. On the other hand, the surface S/Sn ratio approaches a stoichiometric value independent of annealing temperatures. This shows that vacuum annealing could effectively eliminate secondary sulfur excess phases near the surface. There is no apparent change in oxygen and carbon compositions compared to the as-grown sample.

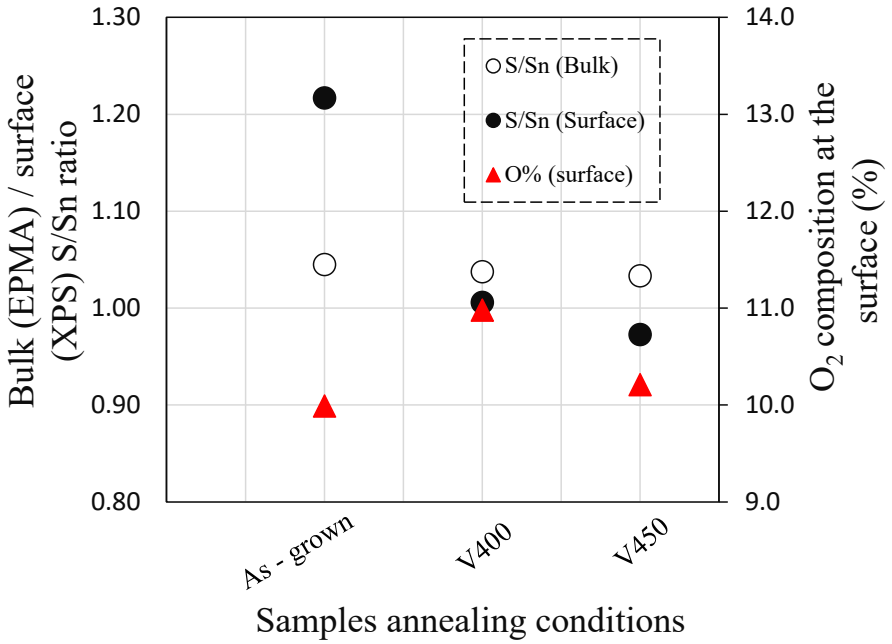

Figure 4-14 Bulk (EPMA) and surface (XPS) chemical composition analysis results of as-grown, vacuum annealed at 400 ℃ (V400), and 450 ℃ (V450 SnS thin films.

Fig. 4-15 (a)-(c) shows the XPS spectra of Sn $3d_{5/2}$, S 2*p*, and O 1*s* of as-grown, vacuum annealed at 400 ˚C (V400), and 450 ˚C (V450) samples. For the as-grown sample, Sn $3d_{5/2}$ (FWHM = 1.38 eV) and S 2*p* peaks are observed at 486.92 eV, and ~ 162.5 eV, respectively. The O 1*s* peak is also observed at 532.3 eV, which arises due to the surface contamination. In the spectrum, Sn $3d_{5/2}$ of sample V400, a significant decrease in the FWHM to 1.12 eV is observed, and the S 2*p* peak of sample V400 is shifted by 0.08 eV to lower binding energy side. The narrowing in FWHM of Sn $3d_{5/2}$ and the shifting of S 2*p* to the lower binding energy side after vacuum annealing could be due to removing sulfur-rich secondary phases such as

SnS_2 and Sn_2S_3 from the surface. The observed Sn 3*d* and S 2*p* are in good agreement with the data reported for SnS.[24)]

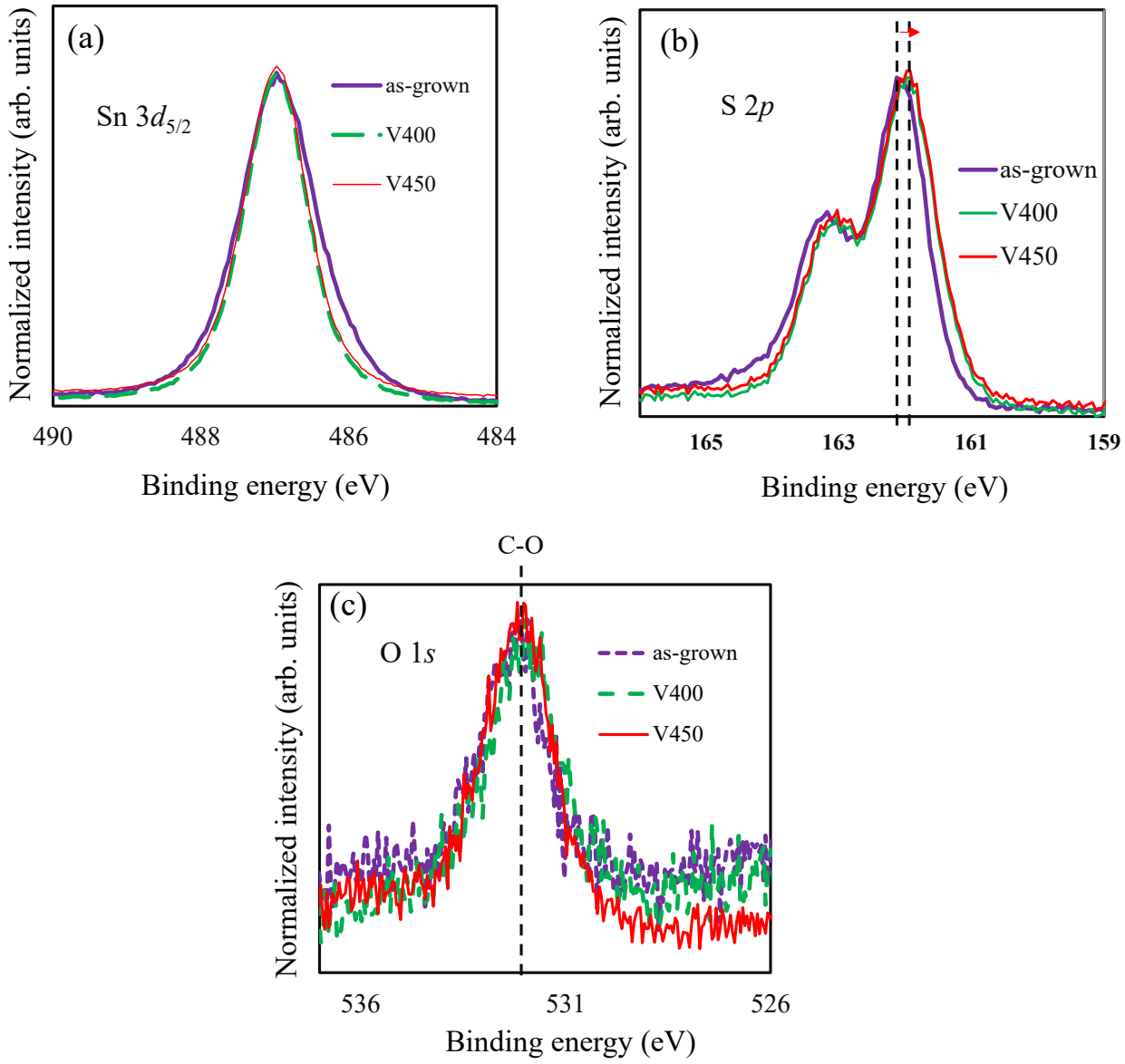

Figure 4-15 XPS spectra of (a) Sn $3d_{5/2}$, (b) S 2p, and (c) O 1s of as-grown, vacuum annealed at 400 ℃ (V400), and at 450 ℃ (V450) SnS sample.

The electrical properties of the films grown at different temperatures are summarized in Table 4-4. All the samples grown exhibit *p*-type conductivity. The as-grown SnS thin films show a resistivity of 9.55×10^{1} Ω cm, the carrier concentration of 1.3×10^{16} cm^{-3}, and hole mobility of 5.02 $cm^2V^{-1}s^{-1}$, respectively. When as-grown SnS is vacuum annealed at 400 ˚C, 120 min, the resistivity decreases to 7.0 Ω cm while carrier concentration and mobility increase to 1.12×10^{17} cm^{-3} and 17.06 $cm^2V^{-1}s^{-1}$, respectively. When the annealing temperature is increased to 450 ˚C, the hole mobility is decreased to 12.26 $cm^2V^{-1}s^{-1,}$ whereas the carrier concentration and resistivity are not significantly changed compared to V400. The increase in carrier concentration after vacuum annealing could be due to eliminating n-type secondary phases such Sn_2S_3 and SnS_2 that could trap free carriers and result in carrier compensation.[28-30] A substantial increase in hole mobility of vacuum annealed samples could be due to the enhancement of crystalline quality and minimization of possible voids between grains.

Table 4-4 Hall effect measurement results of as-grown, vacuum annealed at 400 ℃ (V400) and 450 ℃ (V450) SnS thin films.

Sample	Carrier concentration [cm^{-3}]	Resistivity [Ω·cm]	Mobility [$cm^2V^{-1}s^{-1}$]	Conductivity type
As-grown	1.30×10^{16}	9.55×10^{1}	5.02	*p*
V400	1.12×10^{17}	7.00×10^{0}	17.06	*p*
V450	1.4×10^{17}	1.14×10^{1}	12.26	*p*

4.2.4 Effect of annealing time

The XRD patterns of the as-grown and vacuum annealed at different annealing times are shown in Fig. 4-16. All the SnS thin films exhibit the diffraction peaks of the orthorhombic SnS structure. For the SnS thin films vacuum annealed at 400 ˚C for 30 mins, no noticeable change in diffraction peak is observed compared to that of the as-grown SnS thin film. However, change in prominent peak and decrease in FWHM for peaks at (111) and (040) is observed for the SnS thin-film vacuum annealed at 400 ˚C for a longer time (120 mins) as discussed above in section 4.3.2.1.

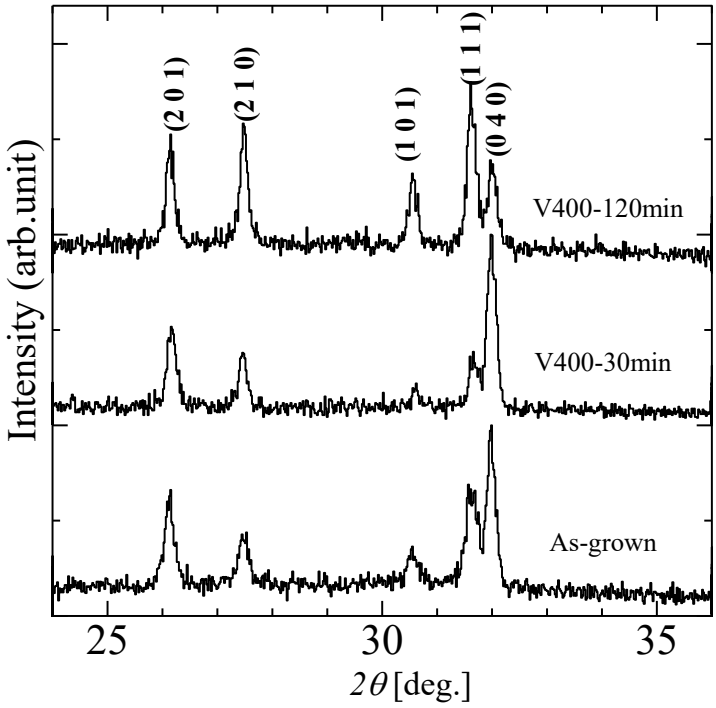

Figure 4-16 XRD patterns of as-grown, vacuum annealed at 400 ˚C, 30 min (V400-30min), and 400 ˚C, 120 min (V400-120min) SnS thin films.

Fig. 4-17 shows the surface morphologies of the SnS thin films for as-grown, vacuum annealed at 400 ˚C, 30 mins (V400-30mins), and vacuum annealed at 400 ˚C, 120 mins (V400-120 min). A slight change in surface morphology is observed when the as-grown sample is vacuum annealed at 400 ˚C, 30 mins. However, smaller grain sizes are kept compared to those annealed longer (120 min). These indicate that a longer annealing time at 120 min is better to complete the recrystallization process to achieve a large grain size.

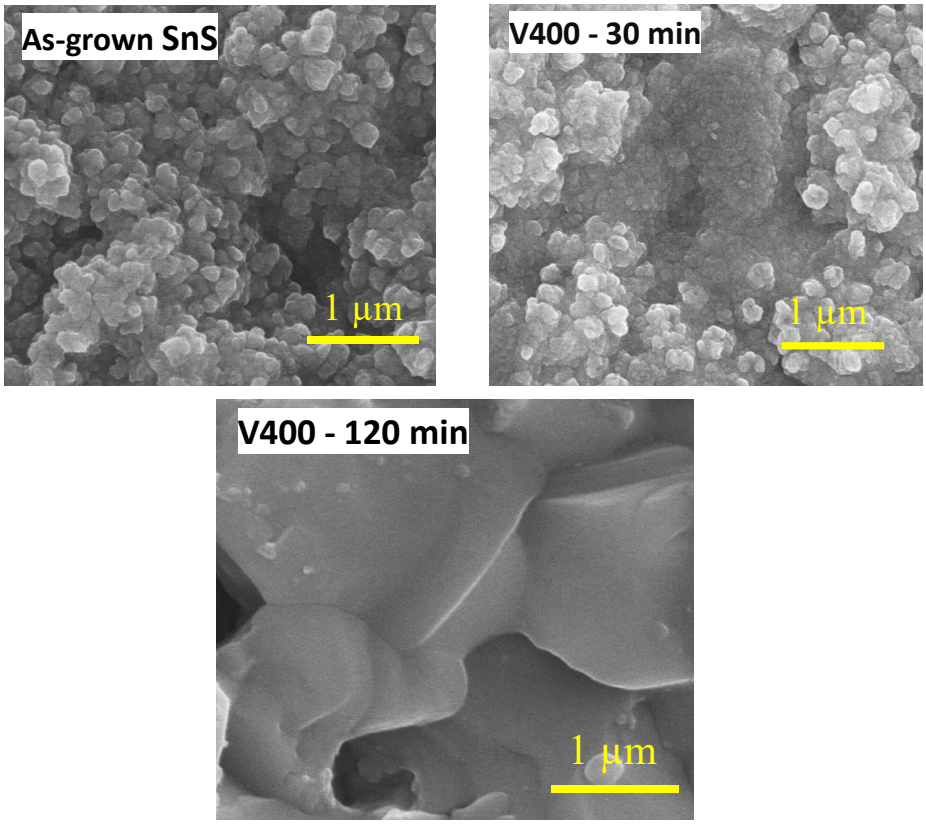

Figure 4-17 SEM images of as-grown, vacuum annealed at 400 ˚C,30 min (V400-30min), and 400 ˚C,120 mins (V400-120min) SnS samples.

Table 4-5 shows the S/Sn ratio of as-grown and vacuum annealed samples at different annealing time. As-grown samples' elemental composition (S/Sn) does not change after vacuum annealing and remains close to stoichiometric composition. This shows that annealing time is not affecting the chemical composition of SnS.

Table 4-5 S/Sn ratio of as-grown, vacuum annealed at 400 ˚C for 30 min (V400-30), 120 min (V400-120).

Sample	S/Sn ratio
As-grown	1.05
V400-30	1.02
V400-120	1.03

The electrical properties of the films grown at different annealing time are shown in Table 4-6. The as-grown SnS thin films show a resistivity of 9.55×10^{1} Ω cm, the carrier concentration of 1.3×10^{16} cm^{-3}, and hole mobility of 5.02 $cm^2V^{-1}s^{-1}$, respectively. When as-grown SnS is vacuum annealed at 400 ˚C, 30 min, the resistivity decreases to 10.86 Ω cm while carrier concentration and mobility increase to 1.68×10^{17} cm^{-3} and 7.64 $cm^2V^{-1}s^{-1}$, respectively. The highest hole mobility of 17.06 $cm^2V^{-1}s^{-1}$ was obtained for the SnS thin film annealed at a longer annealing time of 120 mins. The increase in carrier concentration and

mobility after vacuum annealing could be due to the improvement in crystallinity of SnS, as discussed in section 4.3.3.1.

Table 4-6 Hall effect measurement results of as-grown, vacuum annealed at 400 ℃, 30 min (V400-30min), and 400 ℃,120 min (V400-120min) SnS thin films.

Sample	Carrier concentration [cm^{-3}]	Resistivity [Ω·cm]	Mobility [$cm^2V^{-1}s^{-1}$]	Conductivity type
As-grown	1.30×10^{16}	9.55×10^{1}	5.02	*p*
V400-30min	1.68×10^{17}	1.09×10^{1}	7.64	*p*
V400-120min	1.12×10^{17}	7.00×10^{0}	17.06	*p*

4.3 Effect of post-air-annealing on the vacuum annealed SnS sample grown at 250 ˚C

Fig. 4-18 shows the XRD peaks of vacuum annealed samples at 400 ˚C and post-air-annealed SnS samples at different temperatures. In the case of post-air-annealed samples, which are vacuum annealed at 400 ˚C and followed by air annealing at 150-250 ˚C, no obvious difference in crystallinity is observed compared to that of V400, and no diffraction peaks belong to the impurity phases such as SnO_2 are also detected.

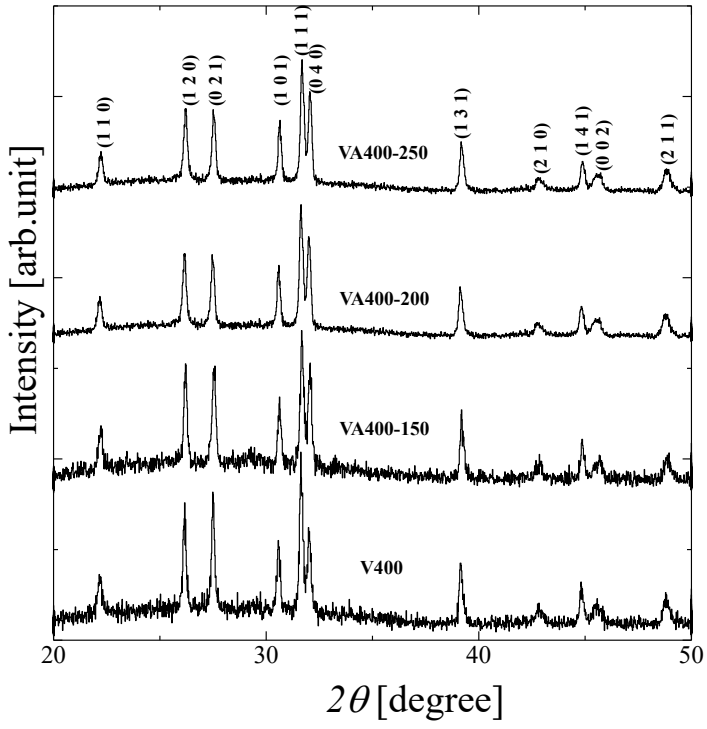

Figure 4-18 XRD patterns of vacuum annealed at 400 ˚C (V400), post-air annealed at 150 ˚C (VA400-150), 200 ˚C (VA400-200), and 250 ˚C (VA400-250) SnS thin films.

Fig. 4-19 shows the SEM images of vacuum annealed and post-air-annealed SnS thin films. No obvious change in morphology and grain size is observed when the vacuum annealed sample is further post-air-annealed independence of annealing temperature.

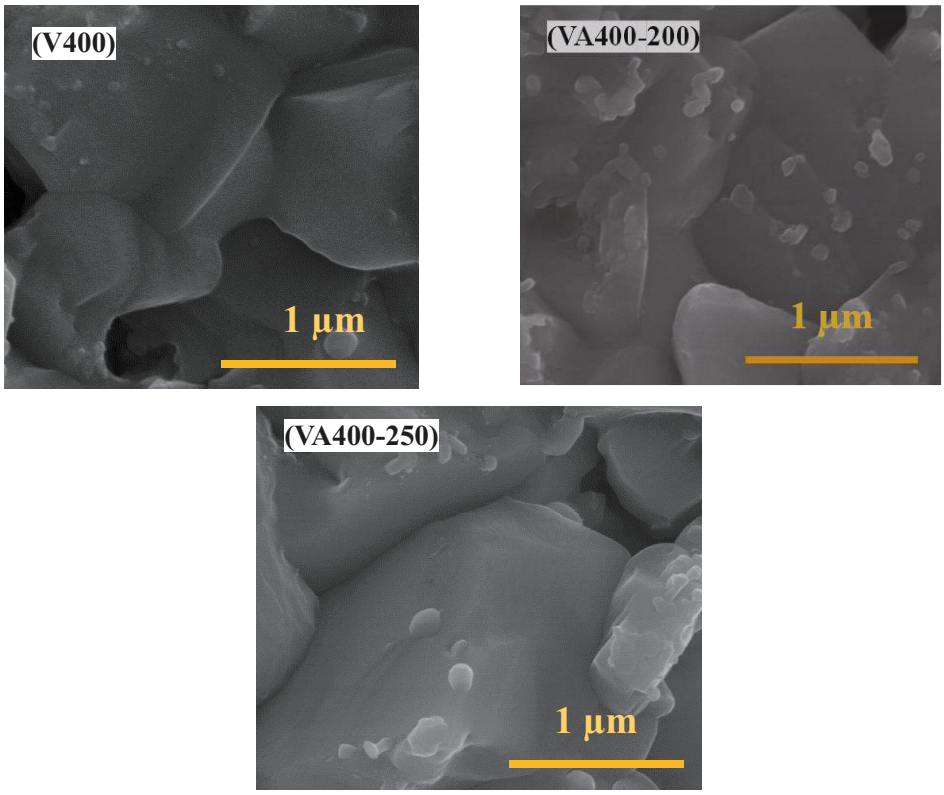

Figure 4-19 SEM images of vacuum annealed at 400 ℃ (V400), post-air-annealed at 200 ℃ (VA400-200) and 250 ℃ (VA400-250) samples.

Fig. 4-20 shows the bulk and surface composition of vacuum annealed samples at 400 ˚C and post-air-annealed samples at 150 - 250 ˚C. In the post-air annealed sample at 150 ˚C, neither bulk nor surface S/Sn ratios were significantly changed compared to that of vacuum annealed sample. The compositions of oxygen and carbon remain the same. The bulk S/Sn ratio of sample post-air annealed at 200 ˚C is not obviously changed, while its surface S/Sn ratio is reduced to ~ 0.93. The composition of carbon remains the same, while that of oxygen is increased to 19.84%, which could be due to the oxidation of the surface.[31, 32] When the post-air-annealing temperature increases to 250 ˚C, the bulk and surface S/Sn ratios decrease to 0.94 and 0.87, respectively. Since the S/Sn ratio of the surface is more significant than that of the bulk, the existence of sulfur defect phases or formations of oxide phases is preferable at the surface. The change in carbon composition is not significant, although the highest oxygen content of 21.94% is observed at the surface. The increase in oxygen content is due to additional oxygen from SnO_x phases, especially near the surface. Very thin amorphous oxide phases could be formed near the surface since oxygen is detected only by XPS but not by XRD. Khan *et al.* also reported the formation of amorphous SnO_2 thin films at oxidation temperature lower than 300 ˚C.[33]

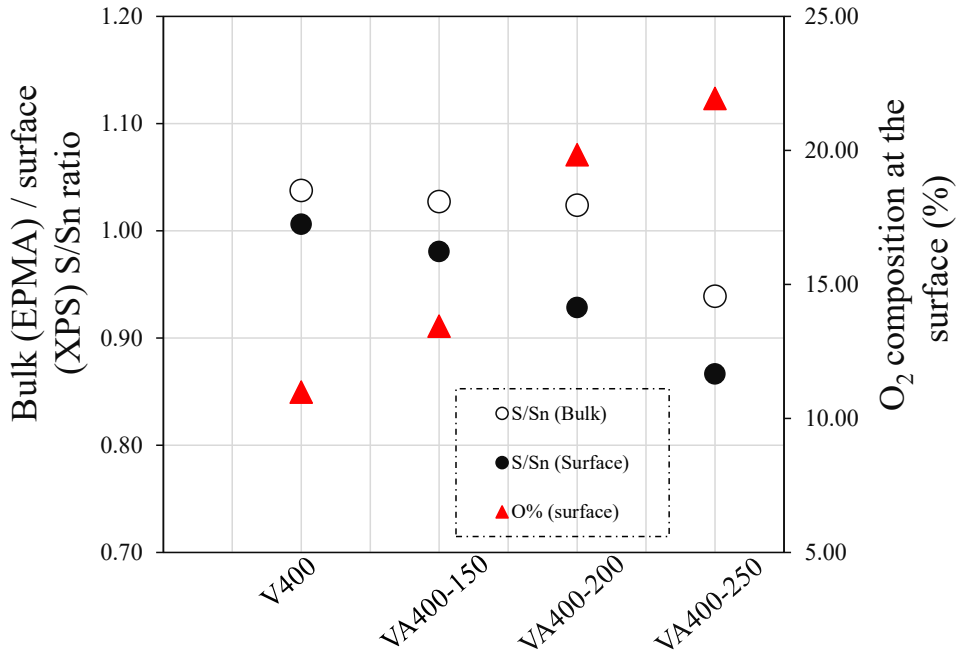

Figure 4-20 Bulk (EPMA) and surface (XPS) chemical composition analysis results of vacuum annealed at 400 ℃ (V400), post-air-annealed at 150 ℃ (VA400-150), 200 ℃ (VA400-200), and 250 ℃ (VA400-250) SnS thin films.

Fig. 4-21 (a)-(c) shows the XPS spectra of Sn $3d_{5/2}$, S 2*p*, and O 1*s* of vacuum annealed at 400 ˚C (V400), post-air-annealed at 150 ˚C (VA400-150), 200 ˚C (VA400-200), and 250 ℃ (VA400-250) samples. The FWHM of the post-air-annealed sample at 150 ˚C is not significantly changed compared to that of the vacuum annealed sample at 400℃. In the case of VA400-200 and VA400-250, the FWHM of Sn $3d_{5/2}$ peak increases to 1.41 eV and 1.47 eV, respectively, while the S 2p peak remains the same compared to that of sample V400. From peak fitting of O 1*s,* as shown in Fig. 4-21 (d), the O 1*s* indicates the presence of an

additional component in the spectrum with a peak at 530.80 eV, which is related to the SnO_2 phase.[34, 35]. The oxygen compositions attributed to the SnO_2 phase and contaminated C-O bonding for the VA400-200 sample are 16.4% and 83.4%, respectively. In the case of sample VA400-250, the composition of oxygen attributed to the SnO_2 phase is increased to 23.2%, while that of the C-O peak is decreased to 76.8%. The broadening in Sn $3d_{5/2}$ peak and increase in oxygen composition attributed to the SnO_2 phase could be due to the surface oxidation by post-air-annealing.

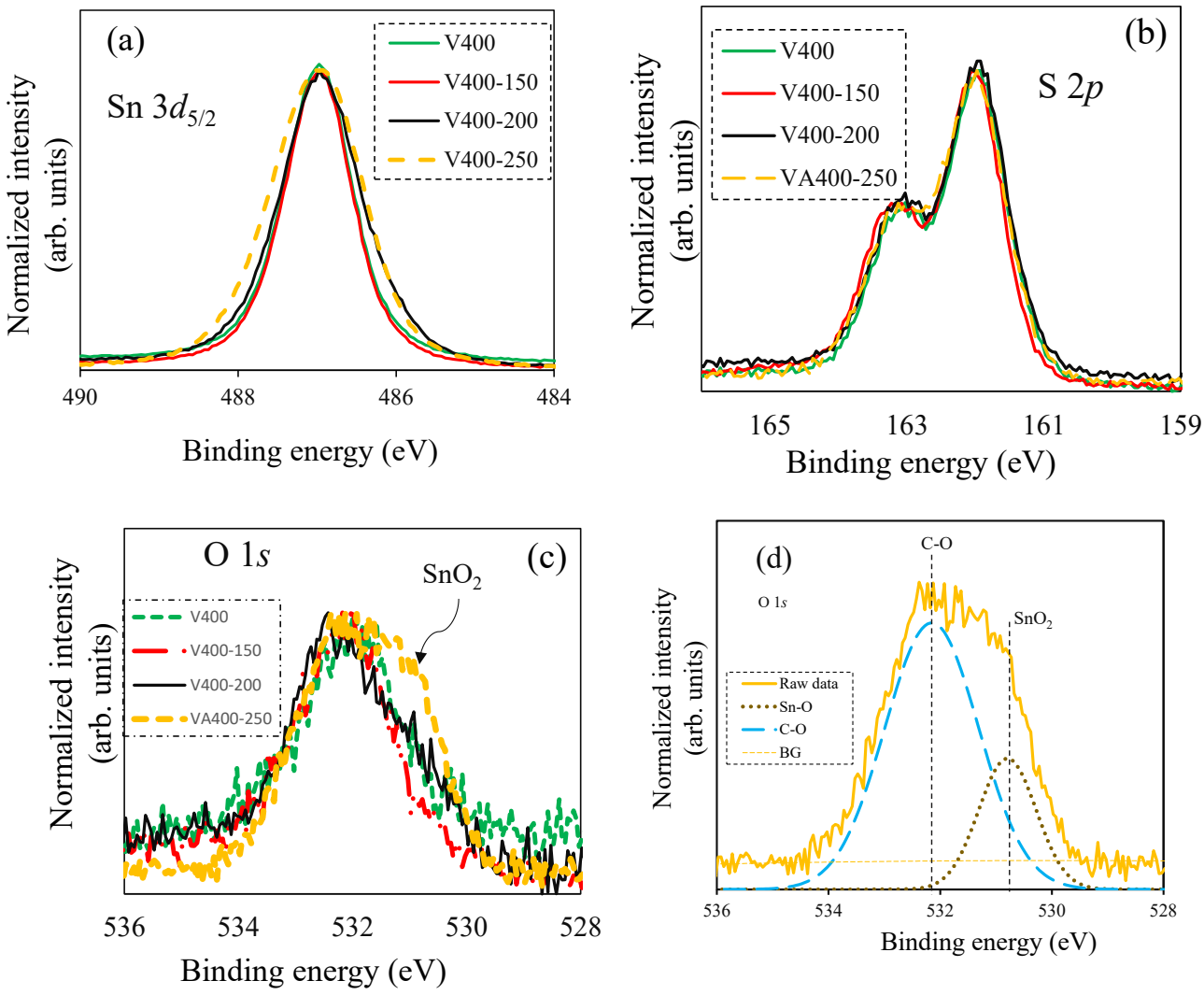

Figure 4-21 XPS spectra of (a) Sn $3d_{5/2}$, (b) S 2p, (c) O 1s of vacuum annealed at 400 ℃ (V400), post-air annealed at 150 ℃ (VA400-150), 200 ℃ (VA400-200), and 250 ℃ (VA400-250) SnS thin films, and (d) peak fitting of O 1s for VA400-250 sample.

The electrical properties of vacuum annealed, and post-air-annealed samples are compared in Table 4-7. All the samples show *p*-type conductivity. The resistivity of post-air-annealed samples increases while carrier concentration decreases compared to the sample with the vacuum annealing only (V400). In the case of the post-air annealed sample at 250 ˚C, the carrier density is reduced to about 61%, and resistivity is increased over 10 times compared to that of the vacuum annealed sample of V400. The possible reason for decreasing the carrier concentration of post-air annealed samples at 150 – 250 ˚C could be that the formation of SnO_{χ} impurity phases near the surface could trap the free carriers and act as a major source of carrier compensation. The decrease in carrier mobility could be due to the SnO_{χ} impurity scattering and/or surface scattering of carriers at the boundaries between the impurity phases and SnS. A similar concept was also reported by Mendis *et al.*[36)]

Table 4-7 Hall effect measurement results of vacuum annealed at 400 ˚C (V400), post-air annealed at 150 ˚C (VA400-150), 200 ˚C (VA400-200), and 250 ˚C (VA400-250) SnS thin films.

Sample	Carrier concentration [cm^{-3}]	Resistivity [Ω·cm]	Mobility [$cm^2V^{-1}s^{-1}$]	Conductivity type
V400	1.12×10^{17}	7.00×10^{0}	17.06	*p*
VA400-150	8.89×10^{16}	5.85×10^{1}	14.10	*p*
VA400-200	7.19×10^{16}	6.89×10^{1}	14.64	*p*
VA400-250	6.81×10^{16}	7.43×10^{1}	12.75	*p*

The plot of $(\alpha hv)^2$ *vs*. *hv* for the SnS thin films prepared at various conditions is shown in Fig. 4-22. The energy bandgap is determined by extrapolating the straight portion of the plot on the energy axis. It is obtained that the optical band gap of about 1.2 eV is not changed after vacuum and post-air-annealing of the as-grown sample.

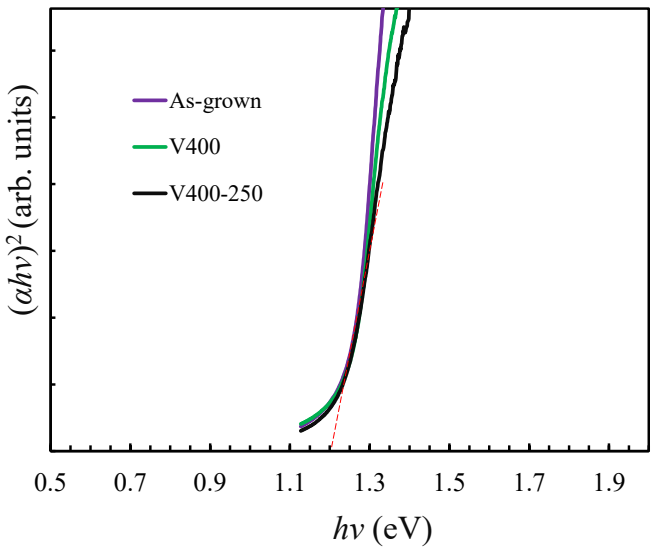

Figure 4-22 $(\alpha hv)^2$ versus hv plots of as-grown, vacuum annealed 400 ℃, and post-air-annealed at 250 ℃ (VA400-250) SnS samples.

Summary

A single-phase SnS and mixed-phase thin films were grown at sulfurization temperatures of 250 ˚C and 300 ˚C, respectively. When the SnS thin film grown at 300 ˚C was vacuum annealed at 500 ˚C, secondary phases were decomposed, resulting in a single-phase SnS thin film. However, no significant change in surface morphology was observed after vacuum annealing. The carrier concentration of the vacuum annealed sample was increased from ~10^{15} cm^{-3} to ~10^{18} cm^{-3}, while the resistivity was decreased from ~10^{2} Ω cm to ~10^{1} Ω cm. When the vacuum annealing was done on the SnS thin film grown at 250℃, the crystallinity of SnS was improved. Sharp and narrow XRD peaks preferably oriented at (111) plane were observed in the sample vacuum-annealed at 400 ˚C. A large average grain size of 1.6 μm was achieved for a vacuum annealed sample at 400 ˚C, while no significant change in morphology was observed for post-air annealed samples. A substantial increase in hole mobility (17 $cm^{2}V^{-1}s^{-1}$) of vacuum annealed samples by over 3 times compared to that of the as-grown sample could be due to the enhancement of crystalline quality and minimization of possible voids between the grains. No apparent changes in the crystallinity of post-air-annealed samples compared to vacuum annealed samples were observed.

Reference

1) V. R. M. Reddy, H. Cho, S. Gedi, K. T. R. Reddy, W. K. Kim, C. Park, *"Effect of sulfurization temperature on the efficiency of SnS solar cells fabricated by sulfurization of sputtered tin precursor layers using effusion cell evaporation"*, J. Alloys Compd. **806**, 410-417(2019).
2) J. Malaquias, P. A. Fernandes, P.M.P. Salomé, and A.F.da Cunh, *"Assessment of the potential of tin sulfide thin films prepared by sulfurization of metallic precursors as cell absorbers"* Thin Solid Films **519,** 7416-7420(2011).
3) T. Raadik, M. Grossberg, J. Raudoja, R. Traksmaa, and J. Krustok, *"Temperature-dependent photoreflectance of SnS crystals",* J. Phys. Chem. Solids **74,** 1683(2013).
4) N. Revathi, S. Bereznev, J. Iljina, M. Safonova, E. Mellikov, and O. Volobujeva, *"PVD grown SnS thin films onto different substrate surfaces",* J Mater Sci: Mater Electron **24,** 4739(2013).
5) O. V. Bilousov, Y. Ren, T. Torndhal, C. Platzer-Björkman, M. Edoff, rndahl, O. Donzel-Gargand, T. Ericson, and C. Ha¨gglund, *"Atomic Layer Deposition of Cubic and Orthorhombic Phase Tin Monosulfide",* Chem. Mater. **29,** 2969(2017).
6) T. Sall, M. Mollar, and B. Mar, *"Substrate influences on the properties of SnS thin films deposited by chemical spray pyrolysis technique for photovoltaic applications",* J Mater Sci. **51**, 7607(2016).
7) L. S. Price, I. P. Parkin, A. M. E. Hardy, and R. J. H. Clark, *"Atmospheric Pressure Chemical Vapor Deposition of Tin Sulfides (SnS, Sn_2S_3, and SnS_2) on Glass",* Chem. Mater. **11,** 1792(1999).

8) V. R. M. Reddy, S. Gedi, C. Park, Miles R.W, and Ramakrishna R. K.T, *"Development of sulfurized SnS thin film solar cells"*, Curr Appl Phys **15**, 588-598(2015).

9) A.Voznyi, V.Kosyak, A.Opanasyuk, N.Tirkusova, L.Grase, A.Medvids, and G.Mezinskis, "*Structural and electrical properties of SnS_2 thin films",* Mater. Chem. Phys. **173**, 52-61(2016).

10) M.N. Amroun and M.Khadraoui, "*Effect of substrate temperature on the properties of SnS_2 thin films"*, Optik 184, 16-27(2019).

11) B. Chen, X. Xu, F. Wang, J. Liu, and J. Ji, *"Electrochemical preparation and characterization of three-dimensional nanostructured Sn_2S_3 semiconductor films with nanorod network",* Mater. Lett. **65,** 400(2011).

12) B. Yang, X. Zuo, H. Xiao, L. Zhou, X. Yang, G. Li, M. Wu, Y. Ma, S. Jin, and X. Che, *"SnS_2 as low-cost counter-electrode materials for dye-sensitized solar cells",* Mater. Lett. **133,** 197(2014).

13) N.G. Deshpande, A.A. Sagade, Y.G. Gudage, C.D. Lokhande, and R.Sharma, *"Growth and characterization of tin disulfide (SnS_2) thin film deposited by successive ionic layer adsorption and reaction (SILAR) technique",* J Alloy Compd. **436**, 421(2007).

14) T. H. Sajeesh, N. Poornima, C. S. Kartha, and K. P. Vijayakumar, *"Unveiling the defect levels in SnS thin films for photovoltaic applications using photoluminescence technique",* Phys. Status Solidi A **207**, 1934–1939 (2010).

15) A. Tanuševski and D. Poelman, *"Optical and photoconductive properties of SnS thin films prepared by electron beam evaporation",* Solar Energy Mater. Solar Cells **80**, 297-303 (2003).

16) M. Ristov, G. Sinadinovski, I. Grozdanov, M. Mitreski, *"Chemical deposition of tin (II) sulfide thin films",* Thin Solid Films **173**, 53-58 (1989).

17) K. T. R. Reddy, P. P. Reddy, P. K. Datta, and R.W.Miles, *"Formation of polycrystalline SnS layers by a two-step process",* Thin Solid Films **403-404**, 116-119 (2002).

18) M. Devika, N. K. Reddy, K. Ramesh, K. R. Gunasekhar, E. S. R. Gopal, and K. T. R. Reddy, *"Influence of annealing on physical properties of evaporated SnS films",* Semicond. Sci. Technol. **21**, 1125–1131 (2006).

19) A. Zakutayev, C. M. Caskey, A. N. Fioretti, D. S. Ginley, J. Vidal, V. Stevanovic, E. Tea, and S. Lany. *"Defect tolerant semiconductors for solar energy conversion",* J Phys Chem Lett. **5**, 1117–25(2014).

20) A. M. Ganose, C. N. Savory, and D. O. Scanlon, *"Beyond methylammonium lead iodide: prospects for the emergent field of ns^2 containing solar absorbers",* Chem Commun. **53**, 20–44 (2017).

21) L. Zhao, Y. Di, C. Yan, F. Liu, Z. Cheng, L. Jiang, X. Hao, Y. Lai, and J. Li, *"In situ growth of SnS absorbing layer by reactive sputtering for thin film solar cells",* RSC Adv. **6**, 4108–4115 (2016).

22) P. Sinsermsuksakul, J. Heo, W. Noh, A. S. Hock, and R. G. Gordon, *"Atomic Layer Deposition of Tin Monosulfide Thin Films",* Adv. Energy Mater. **1**, 1116–1125 (2011).

23) P. D. Antunez, D. A. Torelli, F. Yang, F. A. Rabuffetti, N. S. Lewis, and R. L. Brutchey, *"Low Temperature Solution-Phase Deposition of SnS Thin Films",* Chem. Mater. **26**, 5444 5446 (2014).

24) G.H. Yue, W. Wang, L.S.Wang, X. Wang, P.X. Yan, Y. Chen, and D.L. Peng, *"The effect*

of anneal temperature on physical properties of SnS films", J. Alloys Compd. **474**, 445–449 (2009).

25) F. Jiang, H. Shen, C. Gao, B. Liu, L. Lin, and Z. Shen, *"Preparation and properties of SnS film grown by two-stage process",* Appl. Surf. Sci. **257**, 4901–4905 (2011).

26) S. Sohila, M. Rajalakshmi, C. Ghosh, A.K.Arora, and C. Muthamizhchelvan, *"Optical and Raman scattering studies on SnS nanoparticles",* J. Alloys Compd. **509**, 5843–5847 (2011).

27) M. Devika, N. K. Reddy, D. S. Reddy, S. V. Reddy, K. Ramesh, E. S. R. Gopal, K.R. Gunasekhar, V.Ganesan, and Y. B. Hahn, *"Optimization of the distance between source and substrate for device-grade SnS films grown by the thermal evaporation technique",* J. Phys.: Condens. Matter **19**, 306003 (2007).

28) M. A. Olgar, *"Optimization of sulfurization time and temperature for fabrication of Cu_2ZnSnS_4 (CZTS) thin films",* Superlattices Microstruct. **126**, 32-41(2019).

29) T. Tanaka, T. Sueishi, K. Saito, Q. Guo, M. Nishio, *"Existence and removal of Cu_2Se second phase in coevaporated $Cu_2ZnSnSe_4$ thin films",* J. Appl. Phys. **111**, 053522 (2012).

30) N. Sawada, T. Narita, M. Kanechika, T. Uesugi, T. Kachi, M. Horita, T. Kimoto, and J. Suda *"Sources of carrier compensation in metalorganic vapor phase epitaxy-grown homoepitaxial n-type GaN layers with various doping concentrations"* Appl. Phys. Express **11**, 041001(2018).

31) S. Zhang, L. Fan, D. Yao, J. Wu, H. Guo, H. Wang, and Y. Zhang *"Band alignment tuning at Mo/CZTS back contact interface through surface oxidation states control of Mo substrate"*, Sol. Energy Mater Sol. Cells **229**, 111141 (2021).

32) J. Dar, H. Chung, and M. Chu, *"Post oxidation in improving the Schottky-gate MgZnO/ZnO*

heterojunction field-effect transistors fabricated by RF sputtering", Mater Sci Eng B **266**, 115063 (2021).

33) A. F. Khan, M. Mehmood, M. Aslam, and M. Ashraf, *"Characteristics of electron beam evaporated nanocrystalline SnO_2 thin films annealed in air",* Appl. Surf. Sci. **256**, 2252–2258 (2010).

34) P.M. Korusenko, S.N. Nesov, V.V. Bolotov, S.N. Povoroznyuk, A.I. Pushkarev, and K.E. Ivlev, D.A. Smirnov, *"Formation of tin-tin oxide core–shell nanoparticles in the composite SnO_{2-x}/nitrogen-doped carbon nanotubes by pulsed ion beam irradiation",* Nucl. Instrum. Methods Phys. Res. B **394**, 37–43 (2017).

35) H. Jadhav, S. Suryawanshi, M.A. More, and S. Sinha, *"Pulsed laser deposition of tin oxide thin films for field emission studies",* Appl. Surf. Sci. **419**, 764–769 (2017).

36) B.G. Mendis, M. C. J. Goodman, J. D. Major, A. A. Taylor, K. Durose, and D. P. Halliday, *"The role of secondary phase precipitation on grain boundary electrical activity in Cu_2ZnSnS_4 (CZTS) photovoltaic absorber layer material",* J. Appl. Phys. **112**, 124508 (2012).

Chapter 5

Effect of Sb doping on electrical and physical properties of SnS

Introduction

This chapter discusses the effect of Sb doping on a mixed-phase SnS (as-grown SnS at 300 ˚C) and single-phase SnS (as-grown SnS at 250 ˚C). The effect of Sb doping on the vacuum annealed SnS (as-grown SnS at 250 ˚C => vacuum annealed at 400 ˚C => Sb doping) was also investigated.

5.1 Effect of Sb doping on SnS thin film grown at 300℃ (Mixed phase SnS thin film)

Fig. 5-1 depicts the X-ray diffraction patterns of the grown and Sb doped SnS thin films at 400 ℃ (1.2% Sb), 500 ℃ (2.70% Sb), and 550 ℃ (4.80). In the as-grown SnS film, mixed phases of SnS and SnS_2 are observed. After Sb doping (at all doping temperatures), the SnS_2 phase is decomposed, and a pure orthorhombic phase SnS, preferably oriented along the (040) plane, is obtained. This decomposition of SnS_2 after Sb doping could be due to the effect of temperature, as was also discussed in chapter-4 (Section 4.2.1). The intensity (040) peak for Sb doped SnS increases with doping temperature, which indicates the improvement in crystallinity. The Raman spectra of as-grown SnS thin films and those Sb doped at different Sb content are presented in Fig. 5-2. The Raman patterns of the as-grown SnS thin films show peaks of SnS_2 at 314.5 cm^{-1}, SnS peaks at (80, 105, 170, 195, 225 cm^{-1}), and a

weak peak that belong to Sn_2S_3 at 62 cm^{-1} are observed. It indicates the formation of a mixture of SnS, SnS_2, and Sn_2S_3 at a sulfurization temperature of 300 ˚C, as discussed in chapter 4. However, the secondary phases (Sn_2S_3 and SnS_2) were not observed for the Sb doped samples, consistent with the XRD results.

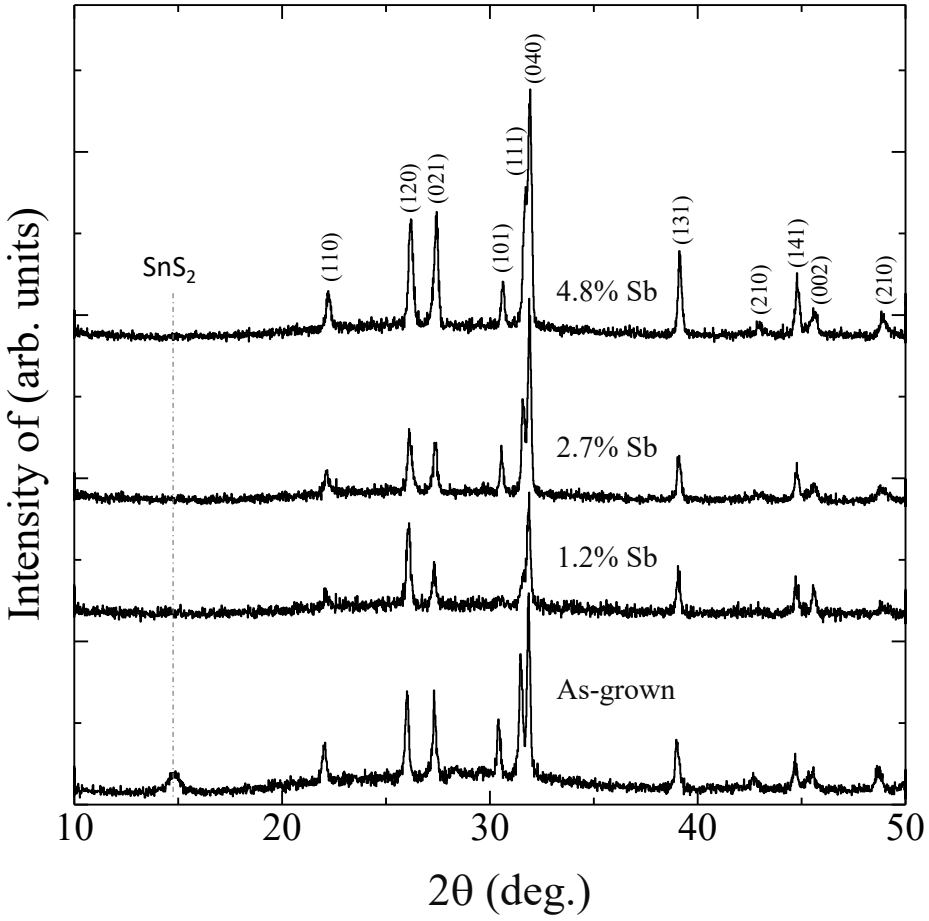

Figure 5-1 XRD spectra of as-grown and Sb doped SnS thin films.

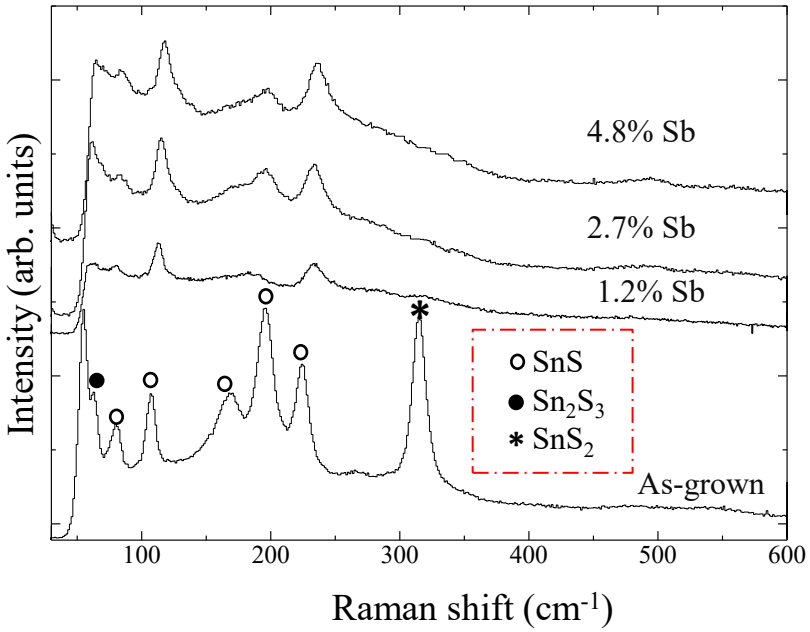

Figure 5-2 Raman patterns of as-grown and Sb doped SnS thin films.

Fig. 5-3 shows the SEM images of as-grown and 4.8% Sb doped samples. There is no significant change in morphology of the as-grown and Sb doped samples at all temperatures, which could be due to the low level of diffused Sb.

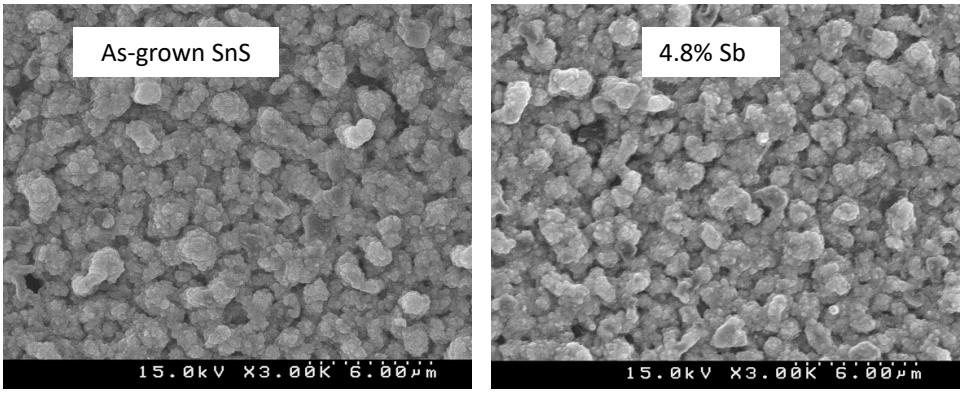

Figure 5-3 SEM images of as-grown and 4.8% Sb doped SnS thin films.

EPMA (Fig. 5-4 and Table-1) analysis shows the S/Sn ratio in the as-grown thin-film is 1.28. In the case of Sb doped samples, the amount of Sb diffused is increased with doping temperature. The samples' S/(Sn+Sb) ratio doped at 400, 500, and 550 ˚C is 1.18, 1.16, and 1.15, respectively. The S/Sn ratio of samples doped at 400 and 500 ˚C is converged near to 1.20. However, in the case of sample doped at 550 ˚C, the S/Sn ratio increases to 1.28, which is the same as that of undoped film. This indicates that the formation of Sn defects, which are the origin of hole carriers, is also favored at higher Sb content due to crystal distortion.

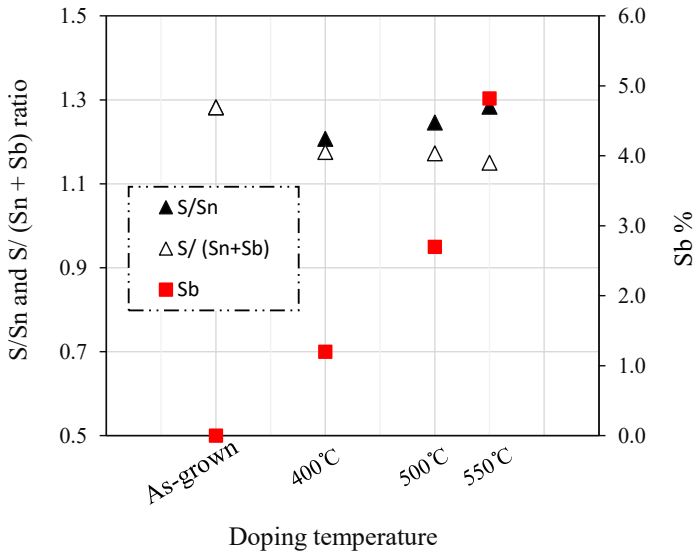

Figure 5-4 S/Sn, S/(Sn+Sb), and Sb% of as-grown and Sb doped SnS thin films at 400℃,500℃, and 550℃.

Table 5-1 S/Sn, Sb%, and S/(Sn+Sb) ratio of as-grown and Sb doped at 400 ̊C (1.2% Sb), 500 ̊C (2.70% Sb), and 550 ̊C (4.80) SnS thin films.

sample	Sb (%)	S/Sn ratio	S/(Sb+Sn) ratio
As-grown	0.00	1.28	1.28
1.2% Sb	1.20	1.21	1.18
2.7% Sb	2.70	1.23	1.16
4.8% Sb	4.80	1.28	1.15

Hall-effect measurement of all doped and undoped films showed *p*-type conductivity. Table 5-2 shows the electrical resistivity, mobility, and carrier density of as-grown and Sb doped SnS thin films. The resistivity is increased from 1.10×10^2 to 4.43×10^5 Ω cm for the sample with 1.2% Sb content, while the carrier density decreases from 4.1×10^{15} to 7.65×10^{12} cm^{-3}. A drastic decrease in hole density and increase in resistivity of the films grown at 1.2% Sb doped SnS could be due to the Sb doping. However, in the case of samples with Sb content larger than 2.7%, the hole density (resistivity) is increased (decreased) again, which could be due to the formation of Sn defects. The mobility of the as-grown sample (13.9 $cm^2V^{-1}s^{-1}$) is reduced to ~ 2.0 $cm^2V^{-1}s^{-1}$ for all Sb doped samples. This decrease in mobility could be due to the impurity (Sb) scattering.

Table 5-2 Hall effect measurement results of as-grown and Sb doped SnS thin films at different Sb content.

Sample	Carrier concentration [cm^{-3}]	Resistivity [Ω·cm]	Mobility [$cm^2V^{-1}s^{-1}$]	Conductivity type
As-grown	4.09×10^{15}	1.10×10^{2}	13.87	p
1.2% Sb	7.65×10^{12}	4.43×10^{5}	1.92	p
2.7% Sb	1.64×10^{14}	2.32×10^{4}	1.71	p
4.8% Sb	4.85×10^{14}	6.54×10^{3}	1.97	p

Fig. 5-5 shows the plot of $(\alpha h\upsilon)^2$ versus $(h\upsilon)$ for the as-grown and Sb doped SnS films. The straight-line portion was extrapolated to the energy axis, and when $(\alpha h\upsilon)^2=0$, the intercept gives the bandgap energy of SnS films. The two absorption edges at 1.2 eV and 1.38 eV for the as-grown film belong to SnS and to that of Sn_2S_3. However, only one linear absorption edge was observed for the Sb doped SnS thin films, confirming the decomposition of the secondary phases.

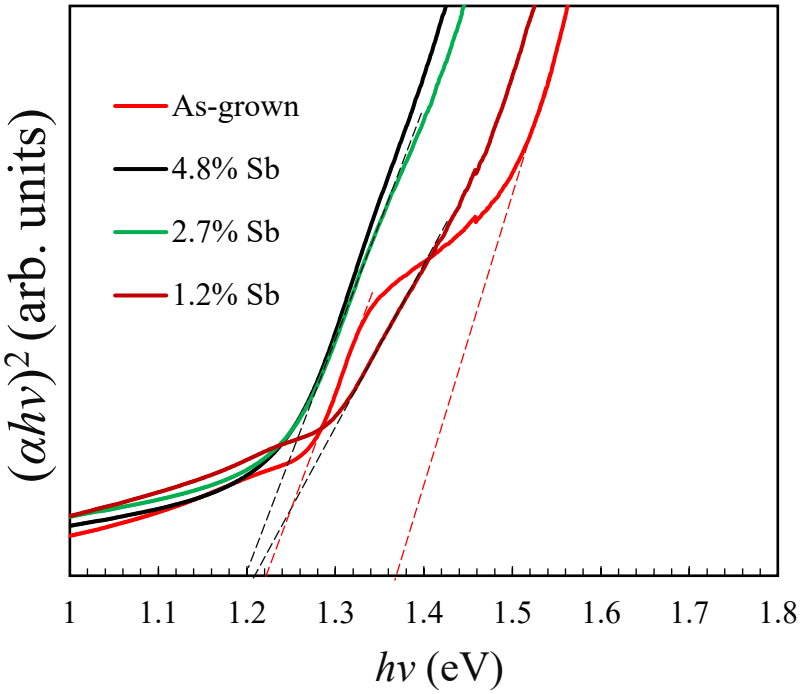

Figure 5-5 $(\alpha h\upsilon)^2$ *versus* $h\upsilon$ plot *of the as-grown and Sb doped SnS thin films*

5.2 Effect of Sb doping on SnS grown at 250℃ (single-phase SnS)

Fig.5-6 shows the XRD patterns of as-grown and Sb doped SnS thin films. A prominent peak at 2θ = 31.7˚ (FWHM = 0.21˚) attributed to the diffraction of (040) planes of orthorhombic SnS was detected in all the samples independent of the Sb content. The intensity of peaks was increased with doping temperature. The FWHM value of (040) peak drops to 0.17˚ and 0.15˚ after doping at 350 ˚C (0.43 % Sb) and 550 ˚C (1.38 % Sb), respectively. No peaks corresponding to Sb and its sulfides were observed for all Sb doping concentrations. The Raman spectra of grown films are shown in Fig. 5-7. The most intense peak at 192 cm^{-1} and others at 95 cm^{-1}, 104 cm^{-1}, 151 cm^{-1}, and 225 cm^{-1} were detected, which are attributed to orthorhombic SnS.[1-4)]

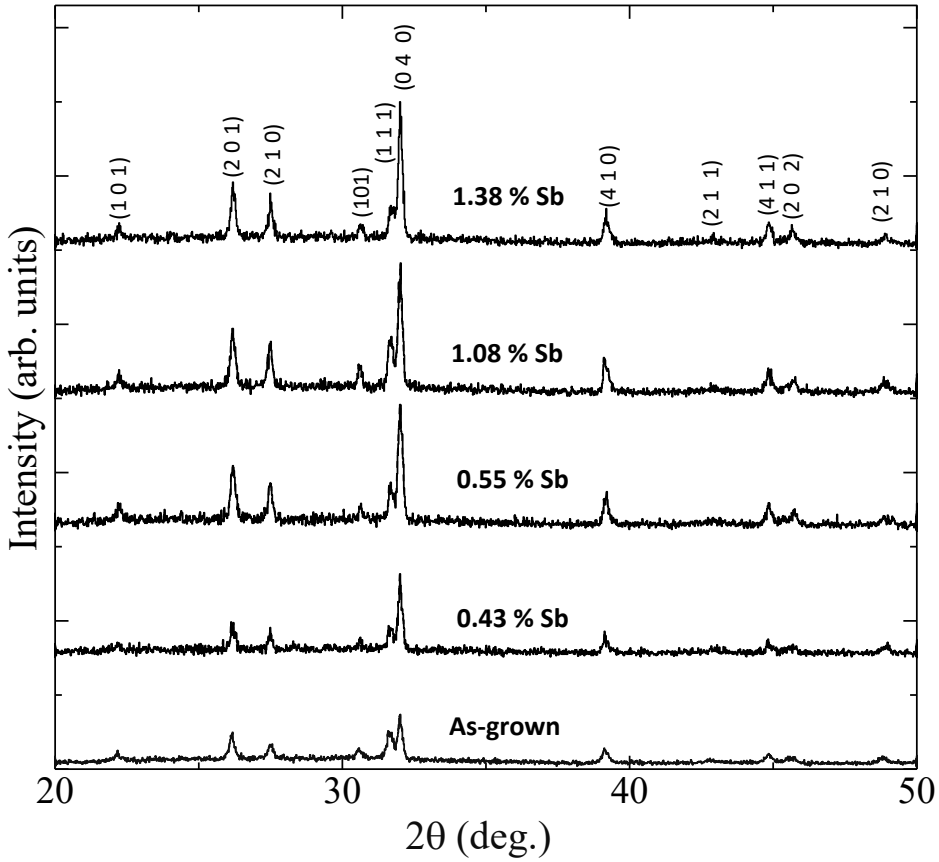

Figure 5-6 XRD spectra of as-grown and Sb doped SnS thin films.

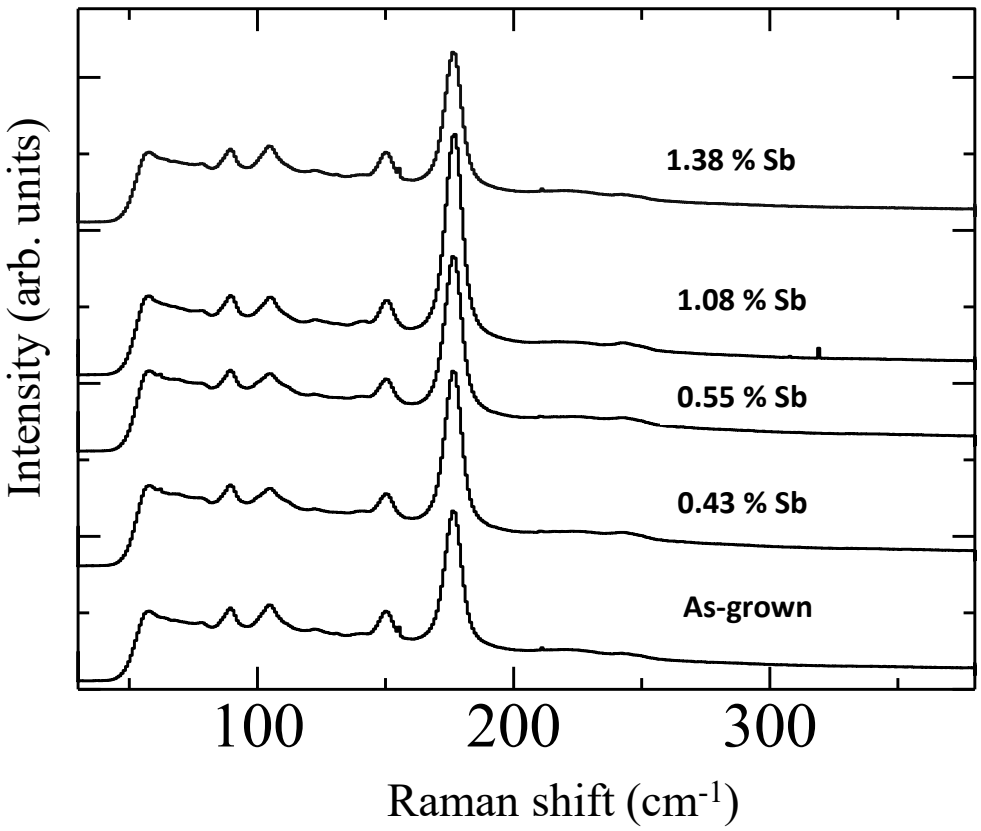

Figure 5-7 Raman patterns of as-grown and Sb doped SnS thin films.

Fig. 5-8 (a) and (b) compares the SEM morphology of both as-grown and 1.3% Sb doped samples. The FWHM value from the XRD results in Fig. 5-6 can also use to determine the grain size of the grown samples by using the Scherrer equation:

$$D = \frac{K\lambda}{\beta\cos\theta} \tag{5-4}$$

where D is the crystallite size, K is the Scherrer constant (K = 0.9), λ is the X-ray wavelength (λ = 1.54 Å) of Cu-Kα1 source, β is the FWHM of the diffraction peak, and θ is the Bragg's angle.[5] The grain size calculated for the as-grown, Sb doped samples at 350 ˚C (0.43 % Sb) and 550 ˚C (1.38 % Sb) are 44.49 nm and 52.28 nm, respectively. This shows that the surface of as-grown SnS is not significantly changed, which could be due to the low level of diffused Sb.

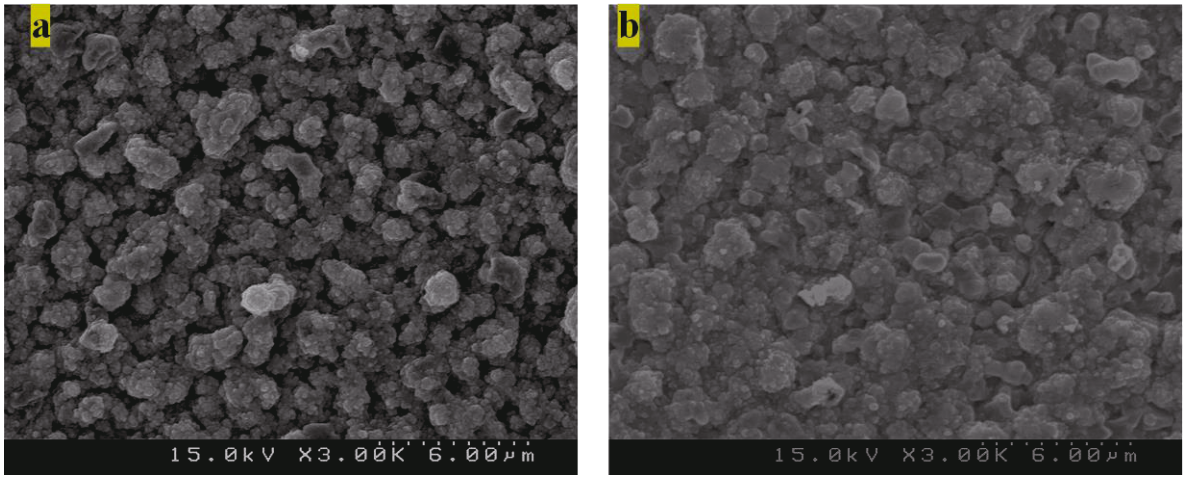

Figure 5-8 SEM images of (a) as-grown and (b) 1.3% Sb doped SnS thin films

Fig. 5-9 and Table 5-3 show the compositional ratio (S/Sn), and the amount of Sb diffused to the film at different doping temperatures. The S/Sn ratio of the as-grown thin-film was 1.03, which is close to stoichiometry. After Sb doping at 350 ˚C, the S/Sn ratio was slightly increased to 1.11. For doping temperature greater than 400 ˚C, the S/Sn ratio is decreased to 1.06 and remains near the stoichiometry composition of SnS for all doping temperatures. The amount of Sb concentration was increased with doping temperature, and 1.38% of Sb was observed at 550 ˚C.

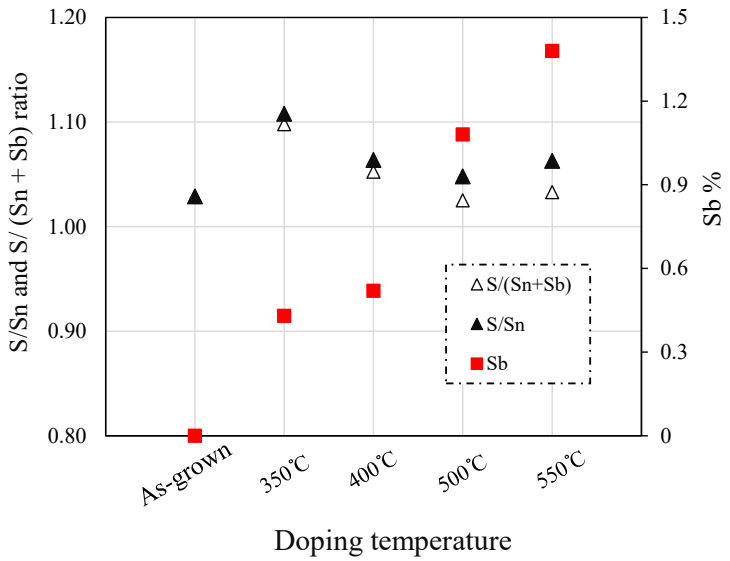

Figure 5-9 S/Sn ratio and amount of diffused Sb for as-grown and Sb doped samples at 350 ˚C, 400 ˚C, 500 ˚C, and 550 ˚C.

Table 5-3 S/Sn, Sb%, and S/(Sn+Sb) ratio of as-grown and Sb doped at 350 ̊C (0.43 % Sb), 400 ̊C (0.55 % Sb), 500 ̊C (1.08% Sb), and 550 ̊C (1.38 % Sb) SnS thin films.

Sample	Sb (%)	S/Sn ratio	S/(Sb+Sn) ratio
As-grown	0.00	1.03	1.03
0.43% Sb	0.43	1.11	1.10
0.55% Sb	0.55	1.06	1.05
1.08% Sb	1.08	1.05	1.03
1.38% Sb	1.38	1.06	1.03

The carrier concentration, mobility, and resistivity of the samples with various Sb contents are shown in Table 5-4. The as-grown films' electrical resistivity and hole density were 95.5 Ω cm and 1.3 × 10^{16} cm^{-3}, respectively. In the sample doped with 0.43% Sb at 350 ˚C, its electrical resistivity decreased to 9.43 Ω cm while hole density was increased to 2.08 × 10^{17} cm^{-3}. This could be due to the Sn vacancy formed as the S/Sn ratio was increased from 1.03 to 1.11, as shown in Fig. 5-9. When Sb concentration was increased to 0.55%, the carrier density decreased, and electrical resistivity increased. For the sample containing 1.38% of Sb, the hole density was reduced to 1.25 × 10^{14} cm^{-3}, and resistivity was increased to 5.65 × 10^{4} Ωcm. The mobility of the samples was increased with Sb content up to 0.55%, and a maximum value of 12.75 $cm^2V^{-1}s^{-1}$was achieved, which is over 2 times larger than that of undoped. Beyond Sb content of 0.55%, the mobility is saturated around 10 $cm^2V^{-1}s^{-1}$, while the carrier concentration is kept decreasing. The increase in hole mobility may be due to the improvement in the crystallinity of the film. The dropping of carrier concentration could be due to the compensation of carriers caused by the substitution of *n*-type Sb impurities into the *p*-type Sn defect sites since the difference of atomic radius between Sn (1.37 Å), and Sb (1.36 Å) is less than 1%.[6, 7] However, atomic radius mismatch between S (1.09 Å) and Sb is about 20%, which is too large so that the substitution of pentavalent Sb into the S site is relatively difficult.[8] The activation energy of as-grown and Sb doped films is described in Fig. 5-10(a). For Sb concentration less than 0.55%, activation energy remains the same and is equal to 0.20 eV. However, the activation energy was increased as Sb concentration was increased above 0.55%, with a maximum value of 0.23 eV at 1.08% Sb. The increase of activation energy at higher Sb doping concentration could be due to the increased Sb

impurities. The $(\alpha hv)^2$ *vs.* (hv) plot of as-grown and Sb doped SnS films are shown in Fig. 5-10(b). A direct bandgap of ~1.22 eV was found for all the films independent of the Sb content.

Table 5-4 Hall effect measurement results of as-grown and Sb doped SnS thin films at different Sb content.

Sample	Carrier concentration [cm^{-3}]	Resistivity [$\Omega \cdot cm$]	Mobility [$cm^2V^{-1}s^{-1}$]	Conductivity type
As-grown	1.30×10^{16}	9.55×10^{1}	5.02	*p*
0.43% Sb	2.08×10^{17}	9.41×10^{0}	6.79	*p*
0.55% Sb	3.81×10^{15}	9.80×10^{2}	12.75	*p*
1.08% Sb	3.92×10^{14}	1.12×10^{3}	11.30	*p*
1.38% Sb	1.25×10^{14}	5.65×10^{4}	10.66	*p*

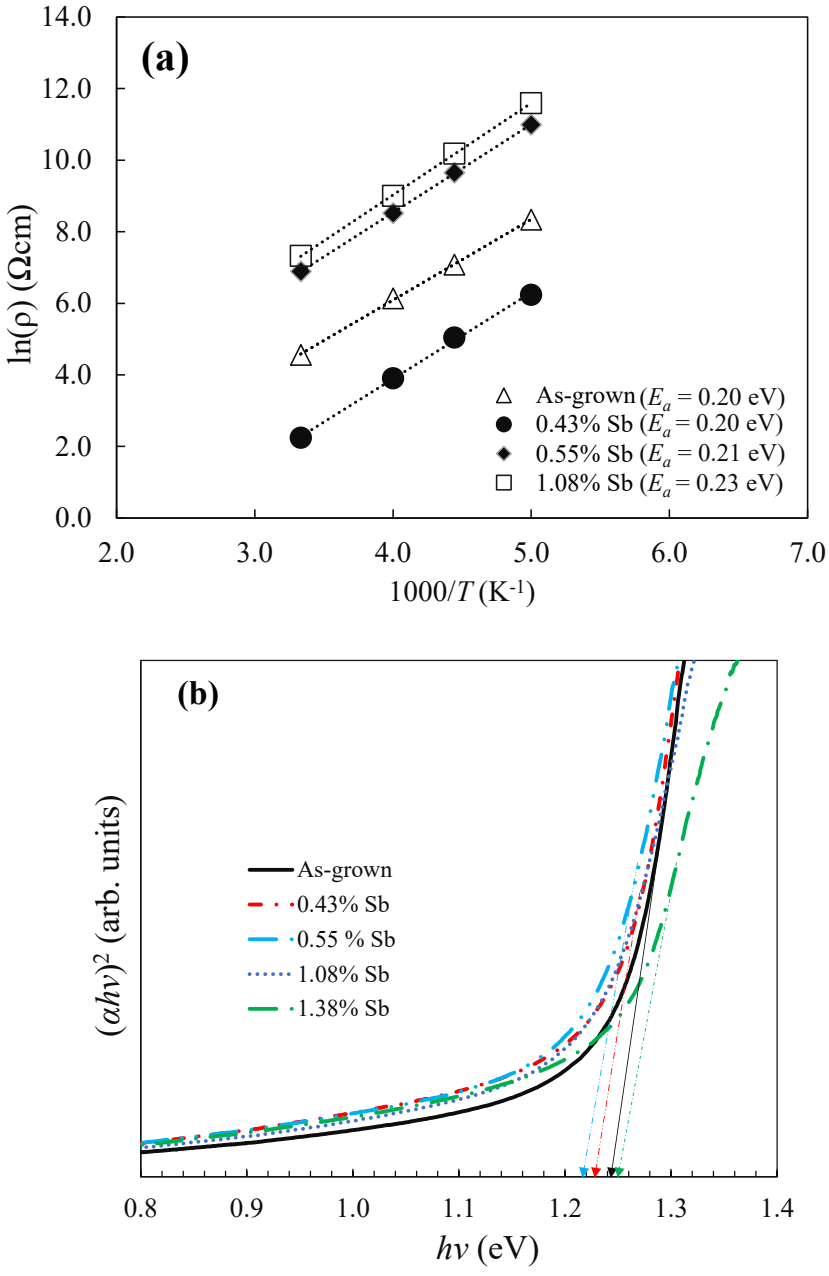

Figure 5-10 (a) activation energy and (b) $(\alpha hv)^2$ versus hv plots of the as-grown and samples with various Sb contents.

5.3 Effect of Sb doping on vacuum annealed SnS

Fig. 5-11 shows the XRD peaks of vacuum annealed and Sb doped SnS thin films. Both vacuum annealed and Sb doped samples are prominently oriented along the (111) plane, a prominent peak for SnS with better crystallinity.

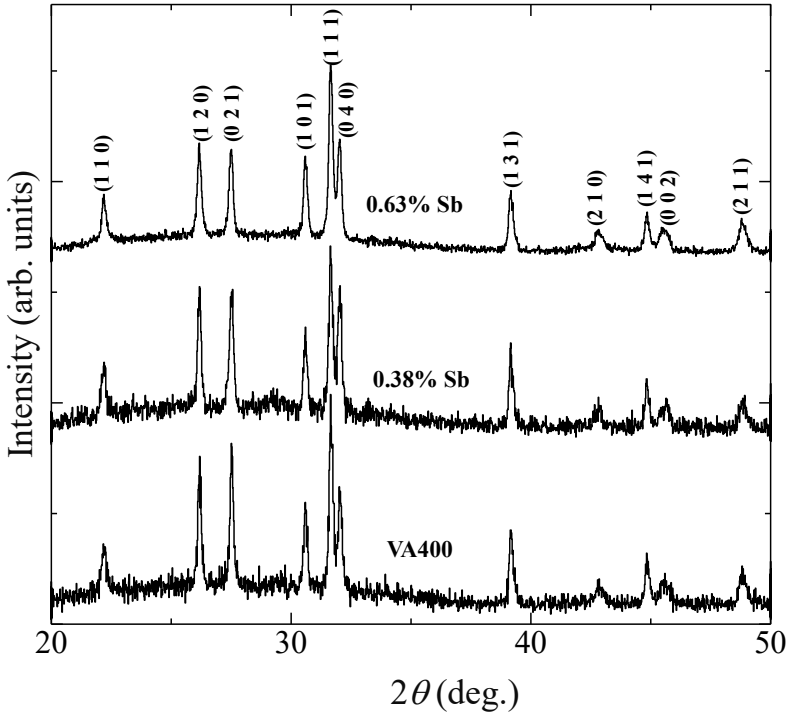

Figure 5-11 XRD peaks of vacuum annealed 400 ℃ (V400), Sb doped at 400 ℃ (0.38% Sb), and 500 ℃ (0.63% Sb) SnS thin films.

Fig. 5-12 shows the SEM images of vacuum annealed SnS at 400 ˚C (SnS grown at 250 ˚C followed by vacuum annealed at 400 ˚C) and Sb doped SnS samples. The grain size of Sb doped samples slightly changed at 0.38% Sb, while a significant decrease in grain size is observed for the sample with a higher amount of Sb (0.63%). This decrease in grain size with Sb doping could be due to the higher doping temperature.

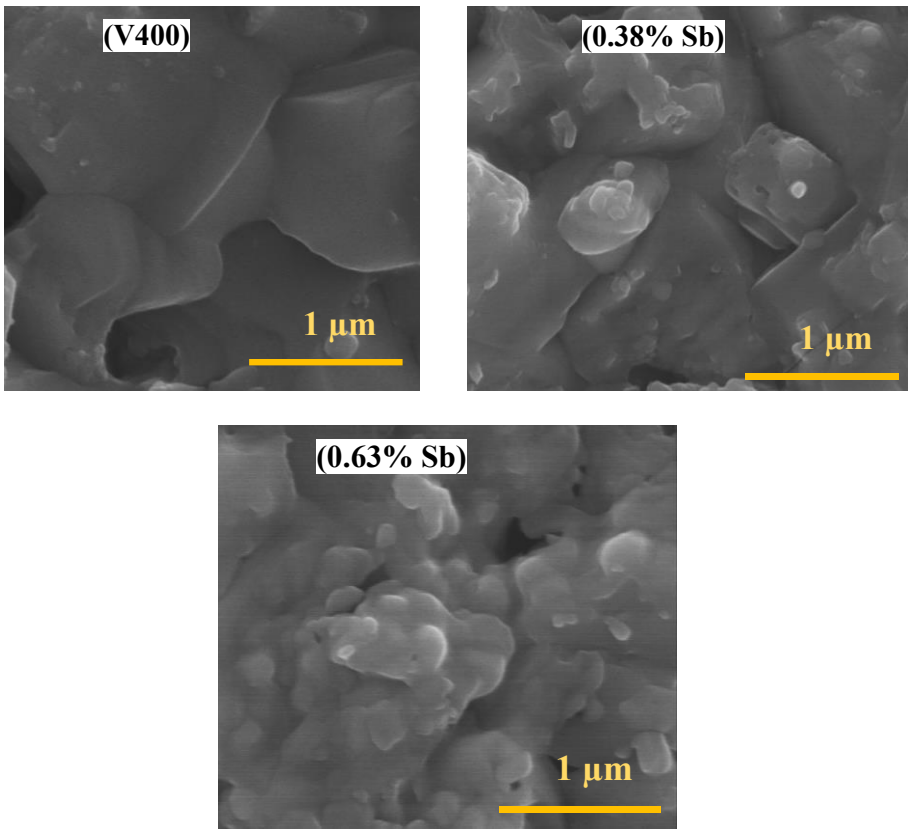

Figure 5-12 SEM images of vacuum annealed 400 ˚C (V400), Sb doped at 400 ˚C (0.38% Sb), and 500 ˚C (0.63% Sb) SnS thin films.

Fig. 5-13 and Table 5-5 show the S/Sn and Sb compositions of the vacuum annealed and Sb doped SnS thin films. 0.38% of Sb is diffused at doing temperature of 400 ˚C and increased to 0.63% as doping temperature increases to 500 ˚C. The S/Sn ratio of vacuum annealed SnS thin film is 1.04 and is slightly decreased to 0.97 and 0.98 for the 0.38% Sb and 0.63% Sb doped SnS samples, respectively. The S/(Sn+Sb) ratio of the Sb doped samples is not significantly changed compared to that of the vacuum annealed sample.

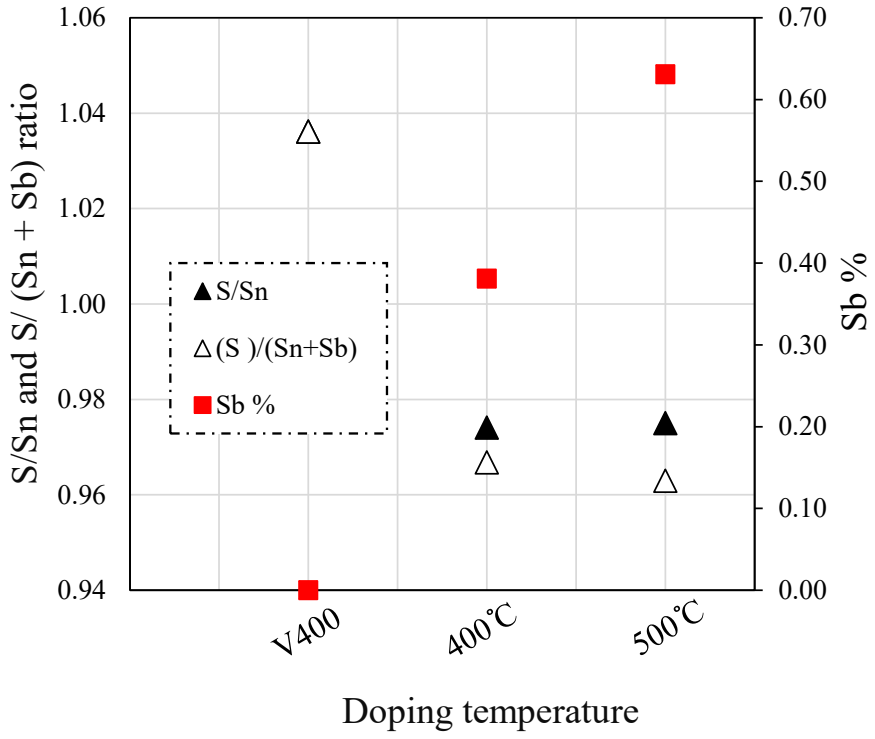

Figure 5-13 S/Sn, Sb%, and S/(Sn+Sb) of SnS thin films vacuum annealed at 400 ˚C (V400), Sb doped at 400 ˚C and 500 ˚C (0.63% Sb).

Table 5-5 S/Sn, Sb%, and S/(Sn+Sb) of SnS thin films vacuum annealed at 400 ℃ (V400), Sb doped at 400 ℃ (0.38% Sb), and 500 ℃ (0.63% Sb).

Sample	Sb (%)	S/Sn ratio	S/(Sb+Sn) ratio
V400	0.00	1.04	-
0.38% Sb	0.38	0.97	0.97
0.63% Sb	0.63	0.98	0.96

Table 5-6 displays the hall measurement results of vacuum annealed and Sb doped samples. The carrier concentration of vacuum annealed samples is decreased from 1.17×10^{17} cm^{-3} to 1.02×10^{16} cm^{-3}, while resistivity is increased from 7.00×10^{0} Ω cm to 1.40×10^{2} Ω cm at 0.38% of Sb doping concentration. The carrier concentration further decreases to 1.80×10^{15} cm^{-3} with the increase of Sb doping concentration to 0.63%. The mobility of the Sb-doped sample at 0.38% Sb is slightly deceased to 15.05 $cm^2V^{-1}s^{-1}$, while a further decrease in mobility to 13.65 $cm^2V^{-1}s^{-1}$ is observed when the amount of Sb has increased to 0.63% Sb. This decrease in mobility could be due to the decrement of grain size. Although the doping of Sb is confirmed, all the doped samples exhibited *p*-type conductivity. Hence, optimization in doping conditions is necessary to realize *n*-type conductivity.

Table 5-6 Carrier concentration, resistivity, and mobility of SnS thin films vacuum annealed at 400 ℃ (V400), Sb doped at 400 ℃ (0.38% Sb), and 500 ℃ (0.63% Sb).

Sample	Carrier concentration [cm^{-3}]	Resistivity [Ω·cm]	Mobility [$cm^2V^{-1}s^{-1}$]	Conductivity type
V400	1.12×10^{17}	7.00×10^{0}	17.06	*p*
0.38% Sb	1.02×10^{16}	1.40×10^{2}	15.05	*p*
0.63% Sb	1.80×10^{15}	2.12×10^{2}	13.65	*p*

Summary

Sb doping was conducted on SnS thin films grown at different conditions. When the Sb doping was done on SnS thin film grown at 300 ˚C (Sb doping on the mixed-phase SnS), the secondary phases (Sn_2S_3, SnS_2) were decomposed. The amount of Sb diffused to the sample is increased with doping temperature, and a maximum value of 4.8% is obtained at 550 ˚C. The S/Sn ratio was varied between 1.28 and 1.21 with doping temperature. The highest resistivity of 5×10^5 Ω cm and a minimum carrier concentration of 7.65×10^{12} cm^{-3} were observed at 1.2% Sb. Upon increasing the amount of Sb up to 2.7%, the carrier concentration was increased again. The optical band gap was varied between 1.2 - 1.4 eV for the as-grown and Sb doped samples. When the SnS thin film was grown at 250℃ (Sb doping on the single-phase SnS), a maximum of 1.38% Sb was obtained at 550 ˚C doing temperature. The crystallinity of Sb doped SnS thin films was improved, and the S/Sn ratio was not altered, which remind near the stoichiometry. A minimum hole concentration of 1.2×10^{14} cm^{-3} and maximum mobility of 12.75 $cm^2V^{-1}s^{-1}$ was observed at 0.55% Sb. No change in optical band gap (1.2 eV) was observed independent of Sb doping temperature. Sb doping was also done on the vacuum annealed SnS thin films (as-grown SnS at 250 ˚C => vacuum annealing=> Sb doping). A maximum of 0.63% Sb was obtained at 500 ˚C doing temperature. The S/Sn ratio was not significantly changed after Sb doping. A minimum carrier concentration of 1.80×10^{15} cm^{-3} was obtained at 0.63% Sb. The conductivity of all Sb doped samples remained *p*-type. In general, the crystallinity of host SnS thin films dramatically determines the effectiveness of Sb doping on SnS thin films

References

1) T. Raadik, M. Grossberg, J. Raudoja, R. Traksmaa, and J. Krustok, *"Temperature-dependent photoreflectance of SnS crystals",* J. Phys. Chem. Solids **74,** 1683 (2013).
2) N. Revathi, S. Bereznev, J. Iljina, M. Safonova, E. Mellikov, and O. Volobujeva, *"PVD grown SnS thin films onto different substrate surfaces",* J. Mater. Sci: Mater Electron **24,** 4739 (2013).
3) O. V. Bilousov, Y. Ren, T. Torndhal, C. Platzer-Björkman, M. Edoff, rndahl, O. Donzel-Gargand, T. Ericson, and C. Ha¨gglund, *"Atomic Layer Deposition of Cubic and Orthorhombic Phase Tin Monosulfide",* Chem. Mater. **29,** 2969 (2017).
4) T. Sall, M. Mollar, and B. Mar, *"Substrate influences on the properties of SnS thin films deposited by chemical spray pyrolysis technique for photovoltaic applications",* J Mater Sci. **51**, 7607 (2016).
5) S. Son, D. Shin, Y. G. Son, C. S. Son, D. R. Kim, J. H. Park, S. Kim, D. Hwang, and P. Song *"Effect of working pressure on the properties of RF sputtered SnS thin films and photovoltaic performance of SnS-based solar cells"* Cryst. Res. Technol. **53**, 1700157 (2018).
6) A. Takeuchi and A. Inoue, *"Classification of Bulk Metallic Glasses by Atomic Size Difference, Heat of Mixing and Period of Constituent Elements and Its Application to Characterization of the Main Alloying Element",* Mater. Trans. **12**, 2817 (2005).
7) M. Fadel, *"The effect of the Sb content on the physical properties of amorphous*

$Se_{0.75}Ge_{0.25-y}$ thin films", Vacuum **52**, 277 (1999).

8) X.H. Wang, S. Liu, P. Chang, and Y. Tang, *"Synthesis of sulfur-doped ZnO nanowires by electrochemical deposition",* Mat. Sci. Semicon Proc**. 10**, 241 (2007).

Chapter 6

Heterojunction properties

Introduction

This chapter details,

1. The comparison of SnS/CdS and SnS/TiO_2 junction properties aims to study the possibility of using these buffer layers for SnS-based solar cell applications.
2. The effect of absorber layer annealing on SnS/CdS junction properties.
3. The measurement of *I-V* characteristics for different In_2O_3/buffer (CdS, TiO_2)/SnS/Mo/SLG devices under dark and bright conditions.

6.1. Preparation of the heterojunctions

Shallow CdS and TiO_2 layers were grown on the SnS absorber layer by chemical bath deposition and sputtering, respectively, to form heterojunction to evaluate band alignment by XPS. The core level difference was determined from the simultaneously detected peaks at SnS/TiO_2 and SnS/CdS junctions. The optical band gap of SnS, CdS, and TiO_2 were also measured and used to determine the band alignments

6.2 Heterojunction properties of SnS/CdS and SnS/TiO_2

In Fig. 6-1, the valance band edge (VBE) of SnS, TiO_2, CdS, SnS/TiO_2, and SnS/CdS measured by XPS are shown. The VBE of SnS, TiO_2, CdS, SnS/TiO_2, and SnS/CdS are observed at 1.05 eV, 1.80 eV, 1.31 eV, -0.80 eV, and 1.2 eV, respectively.

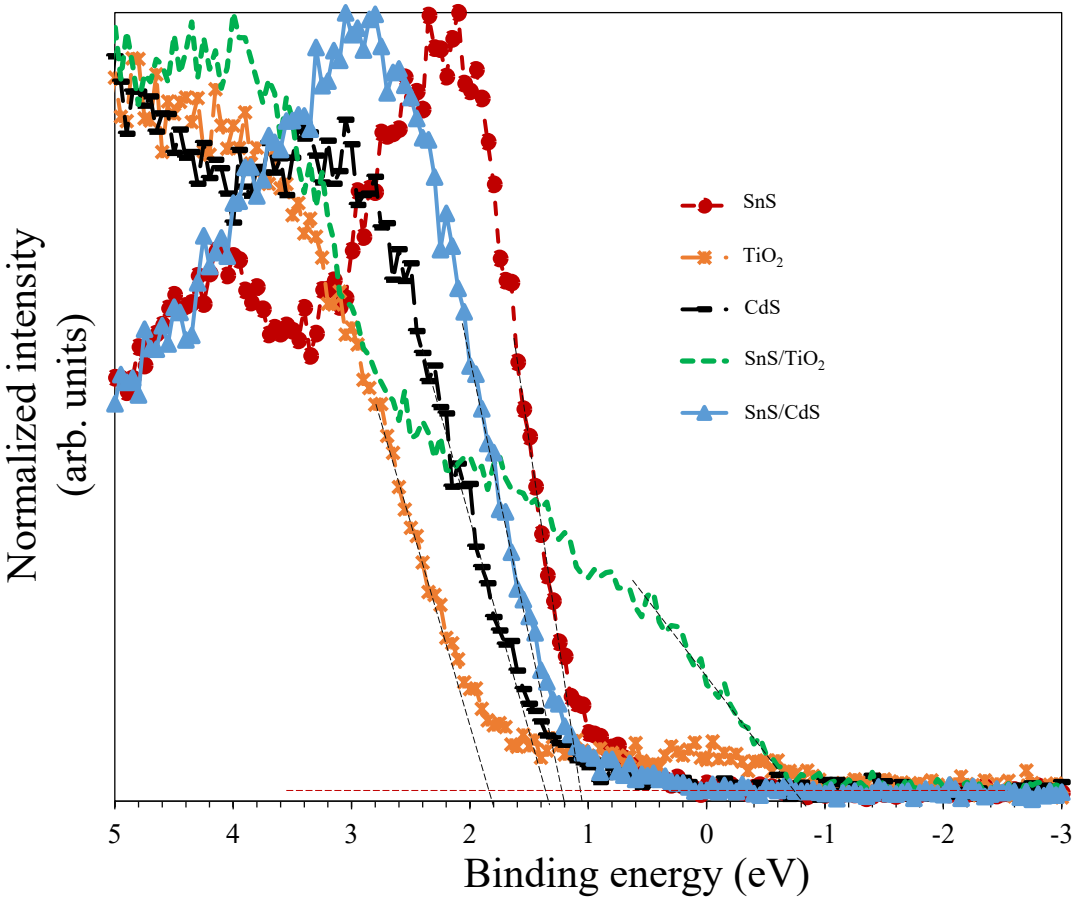

Figure 6-1 Valence band edge (VBE) of SnS, TiO_2, CdS, SnS/TiO_2, and SnS/CdS samples.

The optical band gap of CdS (2.45 eV) and TiO_2 (3.40 eV) are extrapolated from the $(\alpha hv)^2$ versus hv plots in Fig. 6-2. The optical band gap of SnS is 1.2 eV, as is already discussed in chapter 4.

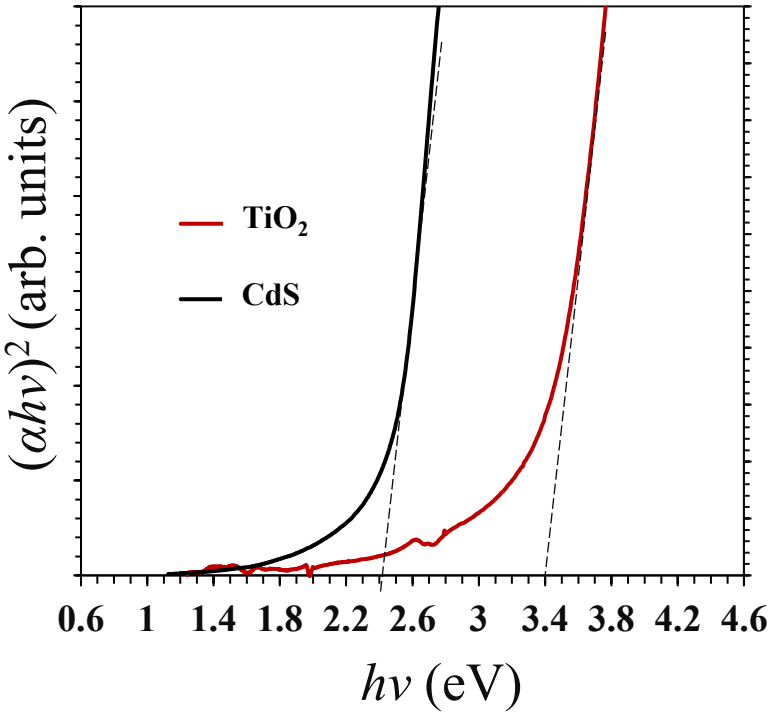

Figure 6-2 $(\alpha hv)^2$ versus hv plots of CdS and TiO_2

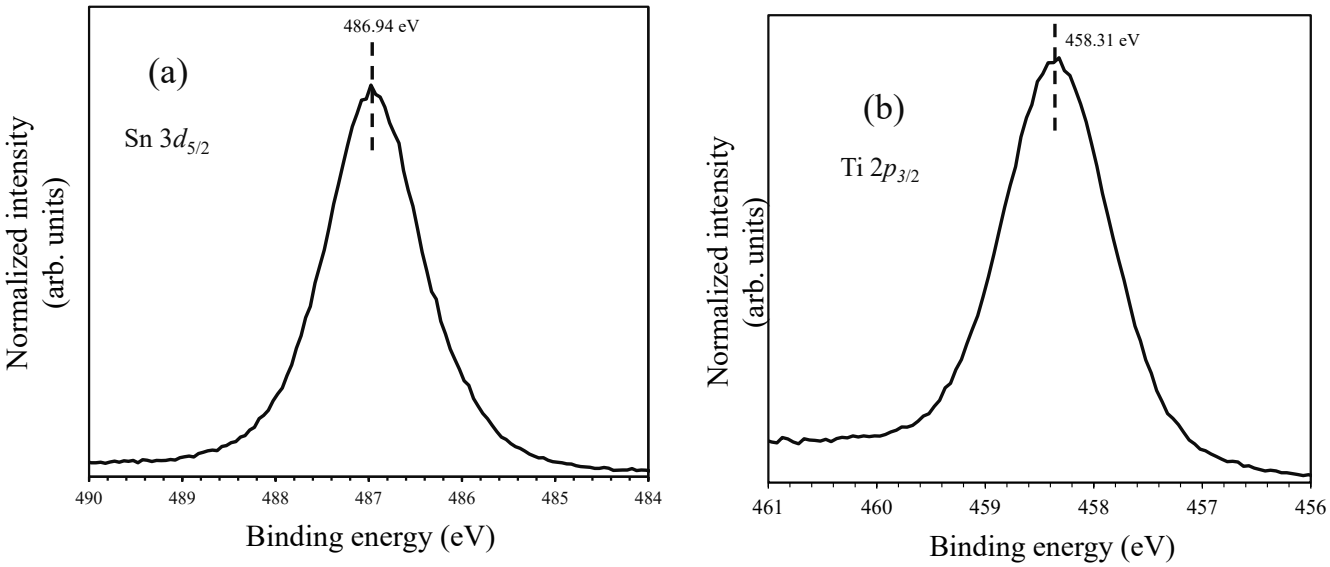

Figure 6-3 XPS spectra of (a) Sn $3d_{5/2}$ in SnS and (b) Ti $2p_{3/2}$ in TiO_2 core levels (CLs) used to determine valence band maximum (VBM) values (energy difference between these core levels and the valence band edge (VBE))

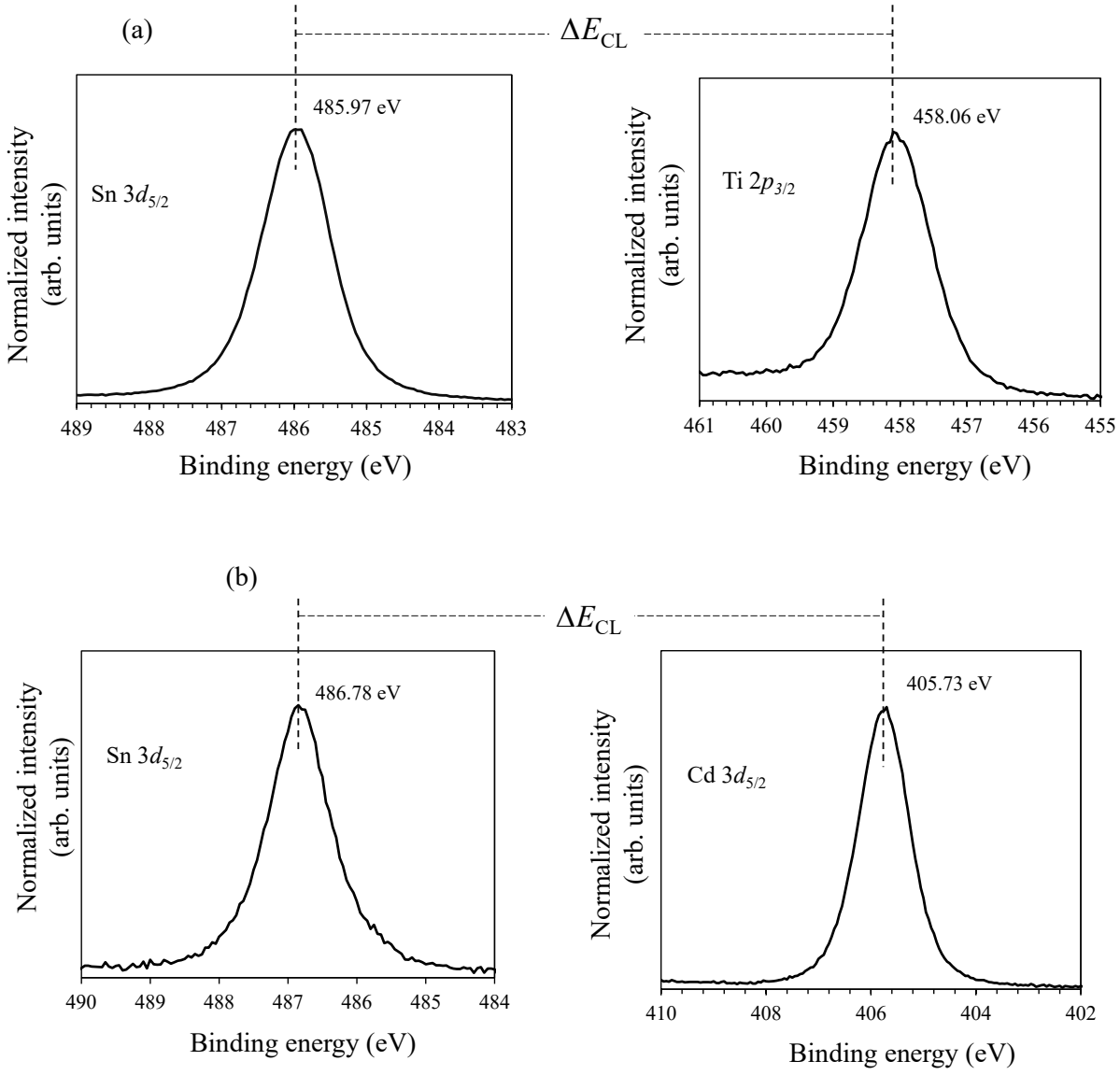

Figure 6-4 XPS spectra of (a) Sn $3d_{5/2}$ and Ti $2p_{3/2}$ in SnS/TiO_2 (b) Sn $3d_{5/2}$ and Cd $3d_{5/2}$ in SnS/CdS heterojunction based on as-grown SnS used to determine the CLs at the junctions.

The valence band offset E_{VBO} at the SnS/TiO_2 junction can be calculated by employing XPS data using the following equation:

$$\Delta E_{\mathrm{VBO}} = \Delta E^{\mathrm{SnS}}_{\mathrm{VBM-Sn}} - \Delta E^{TiO_2}_{\mathrm{VBM-Cd}} - \Delta E^{\mathrm{SnS}}_{\mathrm{CL-SnS/TiO_2}} \quad (6\text{-}1)$$

$$\Delta E_{\mathrm{CBO}} = E_{\mathrm{g}}^{\mathrm{TiO_2}} - \Delta E_{\mathrm{g}}^{\mathrm{SnS}} - \Delta E_{\mathrm{VBO}} \quad (6\text{-}2)$$

Where $\Delta E^{\mathrm{SnS}}_{\mathrm{VBM-Sn}}$ is the energy separation between the VBE and the Sn $3d_{5/2}$ CL in SnS, $\Delta E^{\mathrm{TiO_2}}_{\mathrm{VBM-Ti}}$ is the energy separation between the VBE and Ti $2p_{3/2}$ CL in TiO_2 (Fig. 6-3 and Fig. 6-1), and $\Delta E^{\mathrm{SnS}}_{\mathrm{CL-SnS/TiO_2}}$ is the energy difference between the CLs of Sn $3d_{5/2}$ and Ti $2p_{3/2}$ at the junction (Fig. 6-4 (a)). Using the bandgap energies of TiO_2 3.40 eV (Fig. 6-2) and the bandgap of as-grown SnS thin film 1.2 eV, conduction band offset value for SnS/TiO_2 can be obtained. The valance (ΔEVBO) and conduction (ΔE_{CBO}) band offsets are calculated according to eq. 6-1 and eq. 6-2 for the SnS/TiO_2 heterojunction are obtained to be 1.47 eV and 0.83 eV, respectively.

Similarly, the following equations evaluated the valance band offset (ΔEVBO) of the SnS/CdS heterojunction.

$$\Delta E_{\mathrm{VBO}} = \Delta E^{\mathrm{SnS}}_{\mathrm{VBM-Sn}} - \Delta E^{\mathrm{CdS}}_{\mathrm{VBM-Cd}} - \Delta E^{\mathrm{SnS}}_{\mathrm{CL-SnS/CdS}} \quad (6\text{-}3)$$

$$\Delta E_{\mathrm{CBO}} = E^{\mathrm{CdS}}_{\mathrm{g}} - \Delta E^{\mathrm{SnS}}_{\mathrm{g}} - \Delta E_{\mathrm{VBO}} \quad (6\text{-}4)$$

Where $\Delta E^{\mathrm{SnS}}_{\mathrm{VBM-Sn}}$ is the energy separation between the VBE and the Sn $3d_{5/2}$ CL in SnS, $\Delta E^{\mathrm{CdS}}_{\mathrm{VBM-Cd}}$ is the energy separation between the VBE and Cd $3d_{5/2}$ CL in CdS (Fig. 4-16 (a) and Fig. 6-1), and $\Delta E^{\mathrm{SnS}}_{\mathrm{CL-SnS/CdS}}$ is the energy difference between the CLs of Sn $3d_{5/2}$ and Cd $3d_{5/2}$ at the junction (Fig. 6-4 (b)). Finally, using the eq. 6-2, we evaluated the conduction band offset (ΔE_{CBO}) of the SnS/CdS heterojunction. The bandgap of CdS is 2.45 eV. A ΔE_{VBO} of 0.65 eV and ΔE_{CBO} 0.60 eV are obtained for the heterojunction based on CdS buffer. The measured values for both SnS/CdS and SnS/TiO_2 heterojunctions are summarized in Table 6-1. We have also drawn their (SnS/TiO_2 heterojunctions and SnS/CdS) band alignment diagram In Fig. 6-5, and both junctions are aligned in type-I (“spike-type”) alignment.

Table 6-1 Results of band alignment measurement.

Sample	VBE (eV)	$\Delta E^{SnS}_{CL-SnS/CdS}$ (eV)	$\Delta E^{SnS}_{CL-SnS/TiO_2}$ (eV)	VBO (eV)	CBO (eV)
SnS	1.05	81.05	27.91		
CdS	1.31	-	-	0.65	0.60
TiO_2	1.80	-	-	1.47	0.83

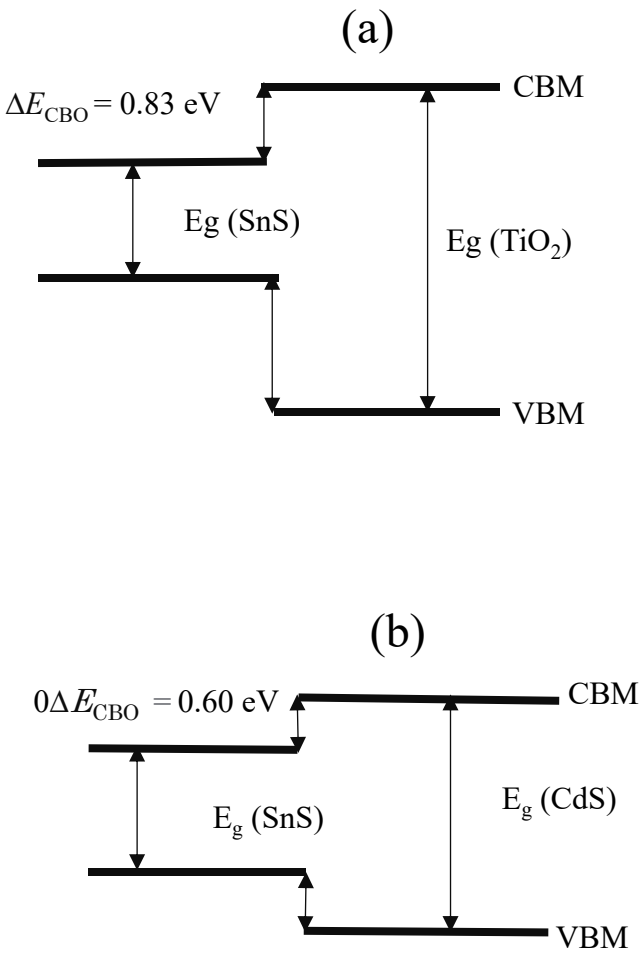

Figure 6-5 Possible band alignment diagram of (a) SnS/TiO_2 and (b) SnS/CdS.

Fig. 6-6 represents the *I-V* characteristics for In_2O_3/buffer (TiO_2,CdS)/SnS/Mo/SLG devices under dark and light conditions. Both fabricated devices based on TiO_2 and CdS buffer layers show a rectifying behavior with a rectification ratio (*V/I at V = 0.5* V) of 0.09 and 2.10, respectively. Under the light condition, the reduction in resistance is observed, indicating the generation of photocarriers in all the devices. A larger decrease in resistance is observed for the device based on CdS buffer, which could be due to the lower CBO barrier at SnS/CdS heterojunction than SnS/TiO_2. By considering the SnS/CdS junction as an ideal diode, the experimental dark current data was fitted to the following equation.

$$I = I_o[\exp(\frac{qV}{nKT} - 1)] \quad (6\text{-}5)$$

Here I_0 is the reverse saturation current, 'q' is the electron's charge, 'n' is the diode quality factor, and 'k' is Boltzmann's constant. The reverse saturation current of 2.2×10^{-3} A is obtained for the device based on CdS buffer (SnS/CdS). A larger saturation current of 5.0×10^{-3} A is obtained for the device based on the TiO_2 buffer layer, which is two times higher than that of the device based on SnS/CdS heterojunction. The observation of this larger reverse saturation current for the diode device based on the TiO_2 buffer layer could indicate the existence of a higher density of defects at the SnS/TiO_2 interface. Despite the rectification, the property is observed for devices based on CdS and TiO_2 buffer layers; no PV effect is observed. This could be due to the significant "spike-type" barriers formed at the SnS/buffer (CdS, TiO_2) interface, which could impede photo-generated carriers in addition to the existence of high-density interface defects. Generally, the CBO barrier based on TiO_2 buffer

at SnS/TiO_2 heterojunction is too large (0.83 eV) to be used for solar cell devices. Therefore, we further consider CdS to investigate the effect of absorber layer annealing on SnS/buffer heterojunction in the following section.

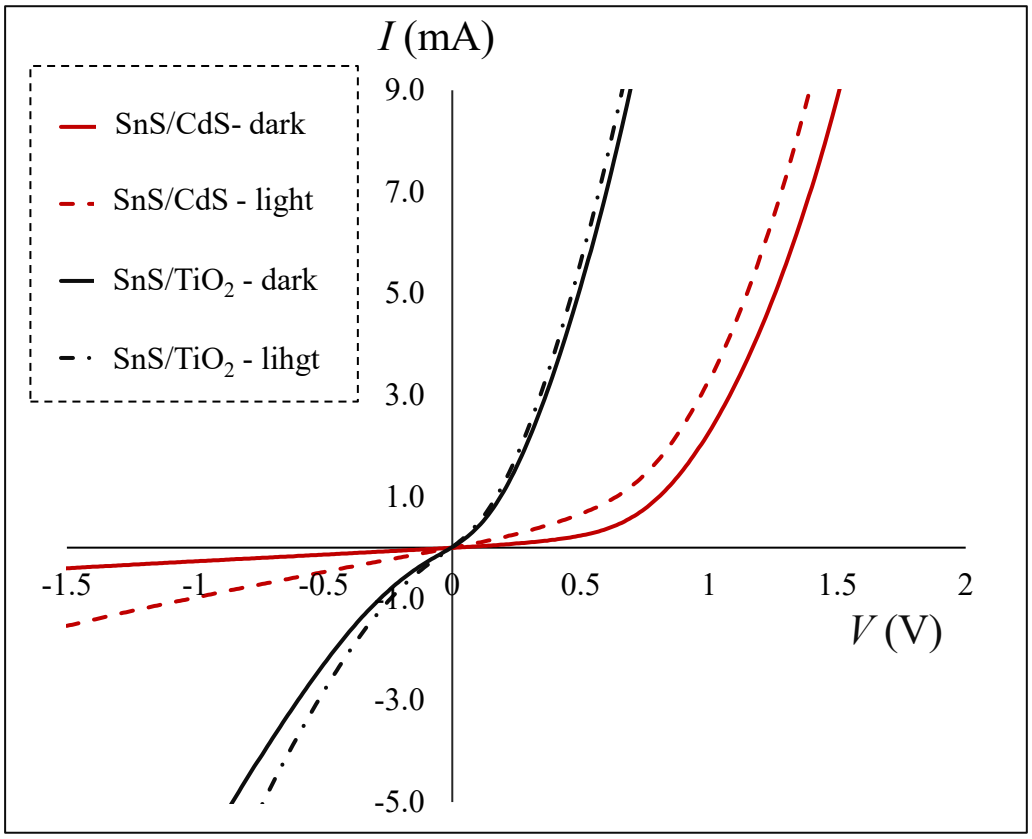

Figure 6-6 Dark/light I-V characteristics of SnS/TiO_2 and SnS/CdS heterojunctions.

6.3 Annealing effect of absorber layer on SnS/CdS heterojunction band alignment

6.3.1 Effect of vacuum annealing temperature

In Fig. 6-7, the valance band edge (VBE) of as-grown, vacuum annealed at 400 ˚C (V400), 450 ˚C (V450) SnS thin films and CdS samples measured by XPS are compared. The VBE of vacuum annealed sample at 400℃ is observed at the shallower energy side (0.79 eV) than that of the as-grown (1.05 eV). However, no further shifting is observed as vacuum annealing temperature increases to 450℃. This shift in VBE of vacuum annealed sample at 400 ˚C to lower binding energy could eliminate sulfur-rich secondary phases at the surface.[1)] The VBE of SnS/CdS heterojunctions based on the V400 and V450 samples are observed at 1.85 eV. The VBE of CdS is observed at 1.31 eV. The valance band offset (ΔE_{VBO}) and conduction band offsets (ΔE_{CBO}) of the SnS/CdS heterojunction are evaluated using eq. 6-3 and eq. 6-4 given above, respectively. The spectra used to determine the valence band maximum and the difference in CLs at the SnS/CdS junction are given in (Fig. 4-16 (a), Fig. 6-7) and in (Fig. 6-8), respectively. The bandgap of as-grown SnS at 250 ˚C is 1.2 eV, and it was not changed after vacuum annealing as it was discussed in section 4.2.3 (Fig. 4-24). The results of valance band and conduction band offsets are shown in Table 6-2. A ΔE_{VBO} and ΔE_{CBO} of 0.65 eV and 0.60 eV are obtained for the as-grown sample, respectively. In the vacuum annealed samples, the ΔE_{VBO} is increased to 0.94 eV while the ΔE_{CBO} is reduced to 0.30 eV. When the vacuum annealed temperature was increased to 450 ˚C, the change in ΔE_{VBO} and ΔE_{CBO} is 0.01 eV which is less than the resolution of the XPS measurement.

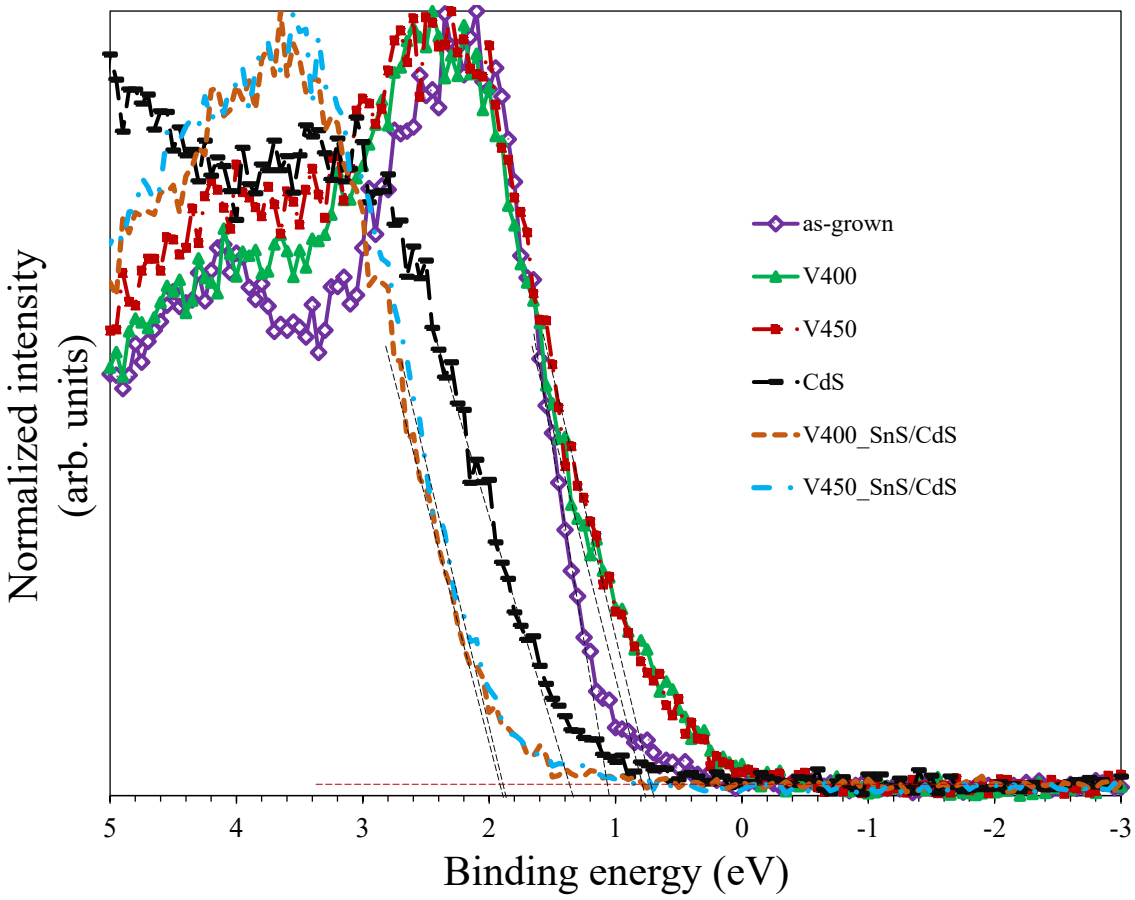

Figure 6-7 Valence band edge (VBE) as-grown, vacuum annealed at 400 ℃ (V400), 450 ℃ (V450) SnS thin films, and CdS. The V400_SnS/CdS and V450_SnS/CdS spectra are the VBE of SnS/CdS heterojunctions based on V400 and V450 samples, respectively.

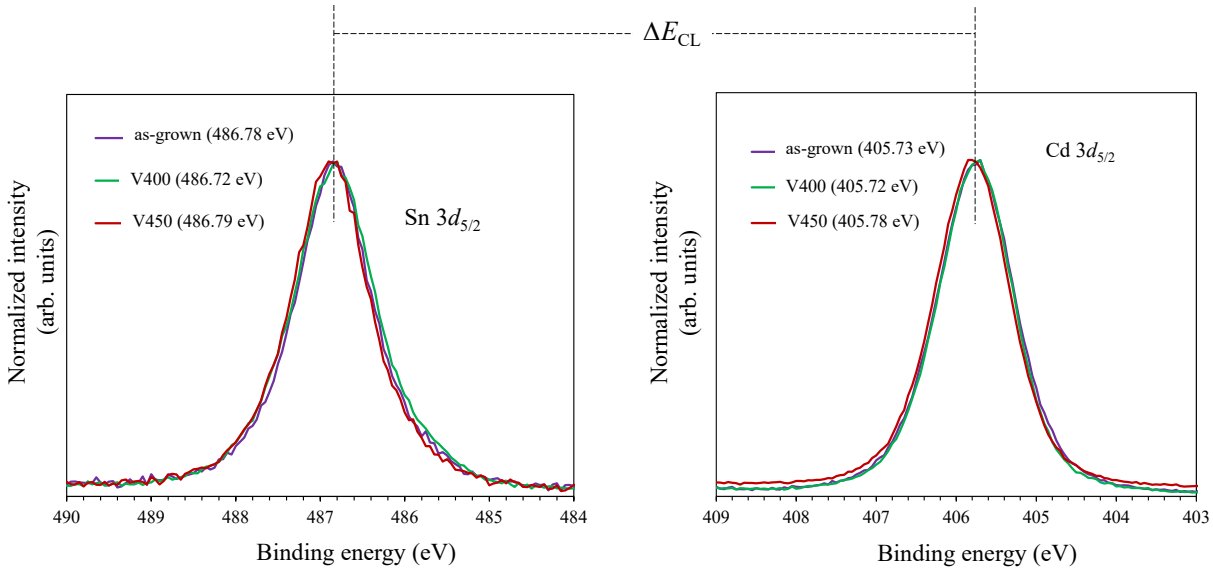

Figure 6-8 XPS spectra of Sn $3d_{5/2}$ and Cd $3d_{5/2}$ in SnS/CdS heterojunction based on as-grown, vacuum annealed at 400 ℃ (V400), and 450 ℃ (V450) SnS thin films which are used to determine the CLs at the junctions.

Table 6-2 Results of band alignment measurement

Sample	VBE (eV)	$\Delta E_{CL-SnS/CdS}^{SnS}$ (eV)	VBO (eV)	CBO (eV)
as-grown	1.05	81.05	0.65	0.60
V400	0.79	81.00	0.94	0.30
V450	0.74	81.01	0.95	0.29
CdS	1.31	-	-	-

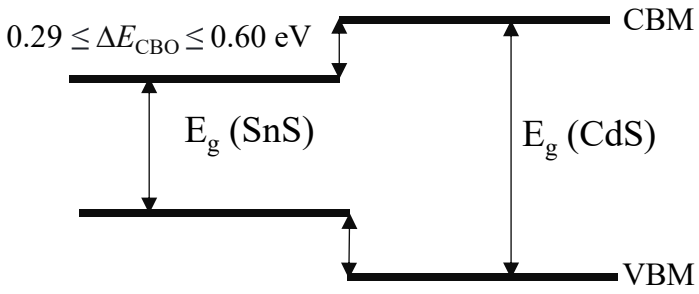

Figure 6-9 Possible band alignment diagram of 400 ℃ (V400), 450 ℃ (V450) SnS thin films with CdS buffer layer.

6.3.2 Effect of post-air-annealing

In Fig. 6-10, valence band edge spectra of vacuum annealed and post-air-annealed SnS thin films are shown. The valence band edge of a sample that is post-air-annealed at 150℃ (VA400-150) is observed at a slightly shallower energy side (0.75 eV) than the vacuum annealed sample at 400 ˚C (V400) (0.79 eV). For samples VA400-200 and VA400-250, the VBE is observed at 0.01 eV and -0.31 eV, respectively. The VBE of SnS/CdS heterojunctions based on post-air-annealed samples are also included in Fig. 6-10 for comparison. The VBE of heterojunctions based on VA400-150 and VA400-200 samples is observed at 1.85 eV, while the VBE based on VA400-250 is at 1.75 eV. No apparent changes in ΔE_{CBO} and ΔE_{VBO} are obtained for the post-air annealed sample at 150 ℃ compared to that of the vacuum annealed samples. In the case of samples VA400-200 and VA400-250, an ΔE_{VBO} of 1.70 eV and 1.90 eV are obtained, while the ΔE_{CBO} is -0.45 eV and -0.65 eV, respectively. The spectra used to determine the valence band maximum and the difference in CLs at the SnS/CdS junction are given in (Fig. 4-23 (a), Fig. 6-10) and in (Fig. 6-11), respectively. The valance and conduction band offsets are plotted in Figures 6-12 and Table 6-3. From eq.6-4, the positive ΔE_{CBO} value represents the energy band alignment when the conduction band minimum (CBM) of SnS is higher than that of CdS, whereas the negative value describes the opposite alignment. Accordingly, the SnS/CdS heterojunctions of as-grown, vacuum annealed, and VA150 samples are aligned in type-I ("spike") alignment as shown in Fig. 6-13(a), while SnS/CdS heterojunctions of samples VA400-200 and VA400-250 are aligned in type-II ("cliff") structure (Fig. 6-13(b)). This change in band alignment from "spike" to "cliff"

at higher post-annealing temperature could be due to the formation of SnO_x, as we have discussed above.

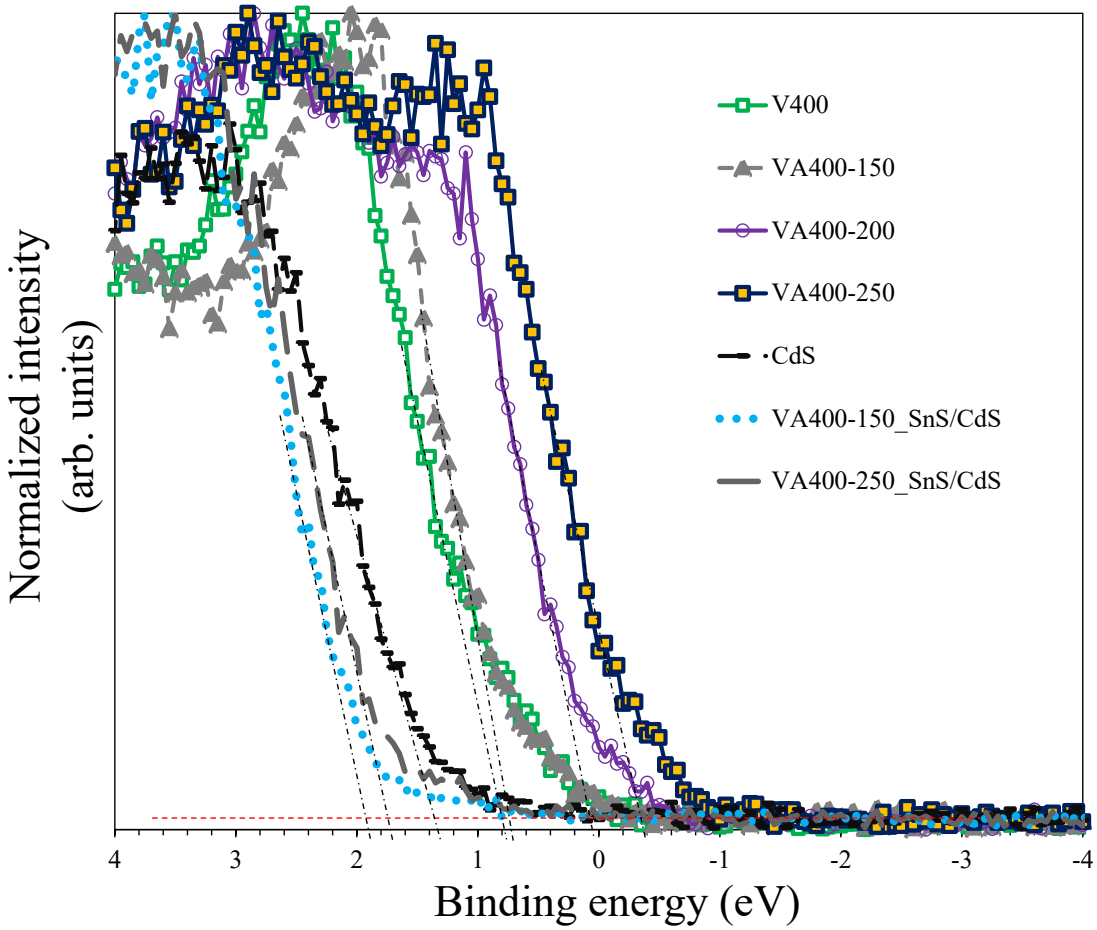

Figure 6-10 Valence band edge (VBE) spectra of SnS thin films vacuum annealed at 400 ℃ (V400), post-air-annealed at 150 ℃ (VA150), 200 ℃ (VA200), 250 ℃ (VA250), and CdS. The VA400-150_SnS/CdS and VA400-250_SnS/CdS are the VBE spectra of SnS/CdS heterojunctions based on the VA400-150 and VA400-250 samples, respectively.

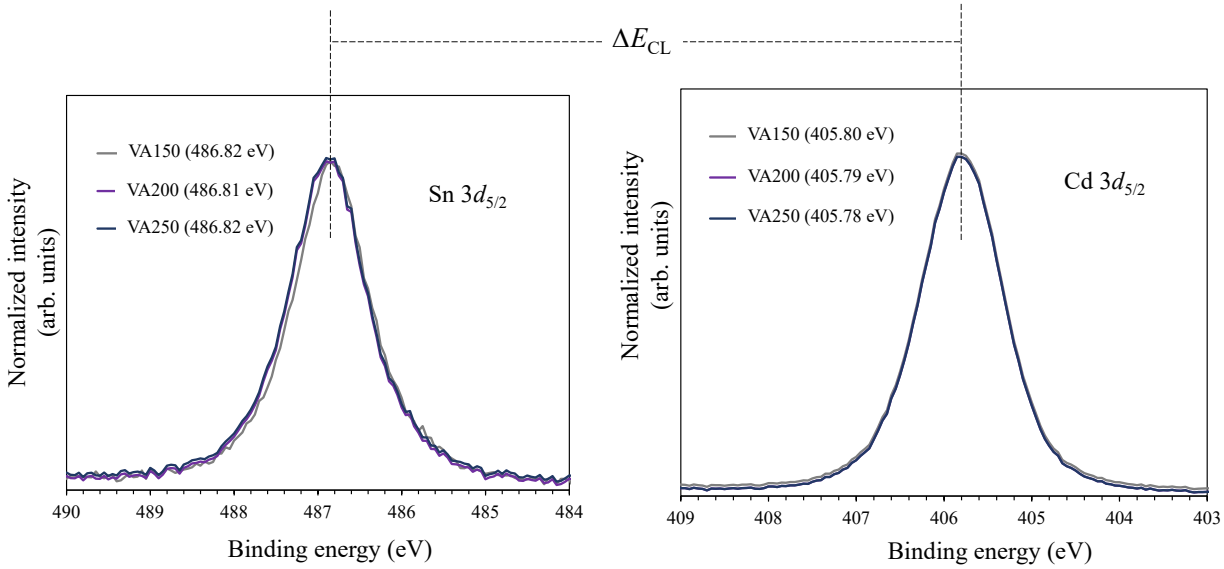

Figure 6-11 XPS spectra of Sn $3d_{5/2}$ and Cd $3d_{5/2}$ in SnS/CdS heterojunction based on SnS thin films post-air-annealed at 150 ℃ (VA150), 200 ℃ (VA200), and 250 ℃ (VA250) that are used to determine the CLs at the junctions.

Table 6-3 Band alignment measurement results of vacuum and post-air-annealed samples.

Sample	VBE (eV)	$\Delta E^{SnS}_{CL-SnS/CdS}$ (eV)	VBO (eV)	CBO (eV)
V400	0.79	81.01	0.94	0.30
VA400-150	0.75	81.02	0.97	0.28
VA400-200	0.01	81.03	1.70	-0.45
VA400-250	-0.31	81.04	1.90	-0.65
CdS	1.31	-	-	-

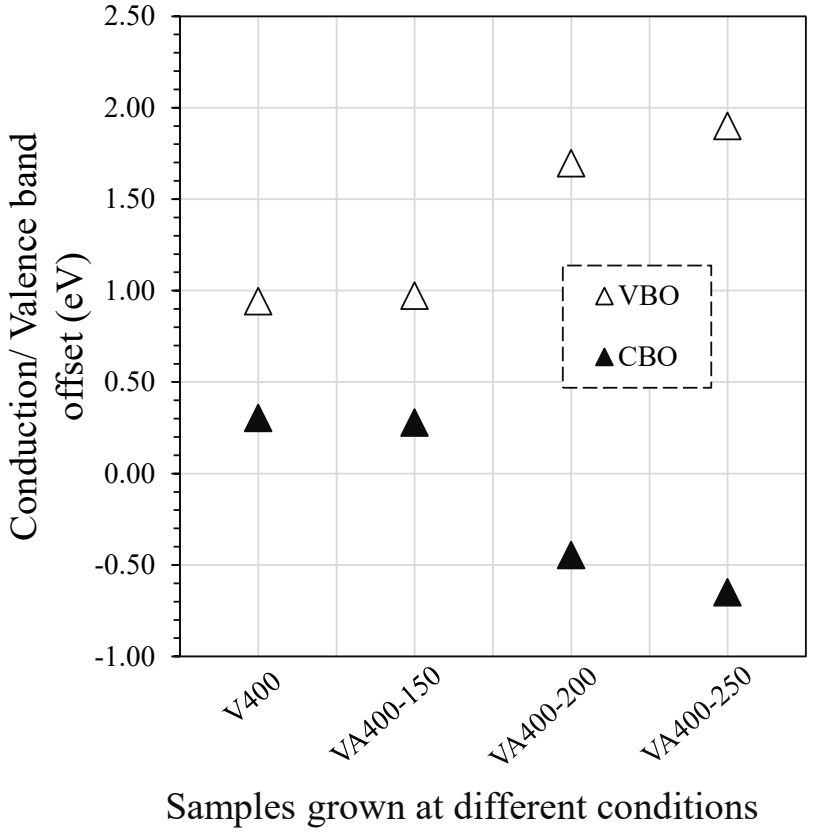

Figure 6-12 Conduction band offset (ΔE_{CBO}) and valence band offset (ΔE_{VBO}) values of SnS thin films vacuum annealed at 400 ℃ (V400), post-air-annealed at 150 ℃ (VA400-150), 200 ℃ (VA400-200), and 250 ℃ (VA400-250).

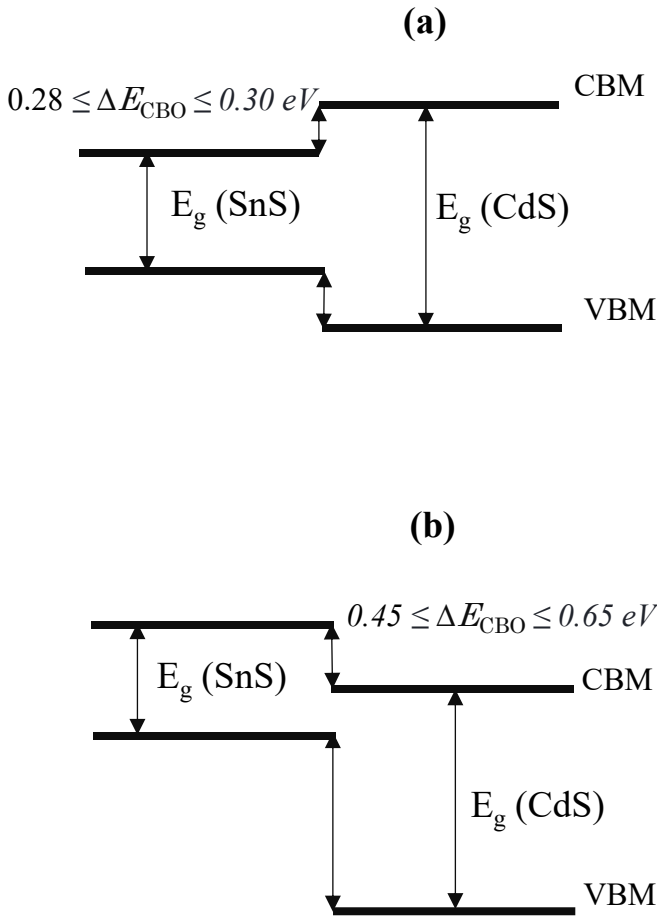

Figure 6-13 Possible band alignment diagrams of SnS thin films (a) vacuum annealed at 400 ℃ (V400) and post-air-annealed at 150 ℃ (VA400-150) (b) post-air-annealed at 200 ℃ (VA400-200) and post-air-annealed at 250 ℃ (VA400-250).

6.3.3 Effect of Sb doping

The valence band edge spectra of vacuum annealed and Sb doped SnS thin films are shown in Fig. 6-14. The *VBE* of Sb doped SnS is observed at slightly shallower energy (0.76 eV) than vacuum annealed sample at 400 ˚C (0.79 eV). The VBE of 0.63% Sb_SnS/CdS (VBE of SnS/CdS based on 0.63% Sb) observed at 1.85 eV. A ΔE_{CBO} of 0.29 eV was obtained for the Sb doped SnS thin films, which is not significantly changed compared to the vacuum annealed SnS thin film. The ΔE_{CBO} and ΔE_{VBO} measurement results are also given in Table-4.

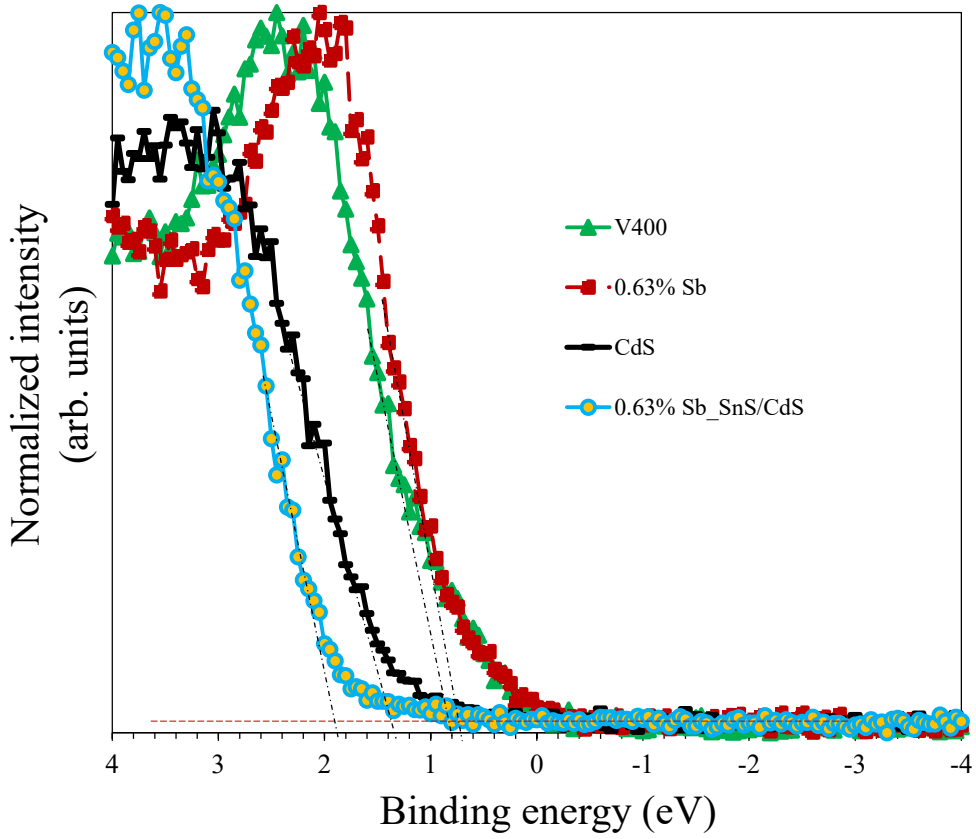

Figure 6-14 Valence band edge spectra of SnS thin films vacuum annealed at 400 ℃ (V400), Sb doped at 400 ℃ (0.63% Sb), and CdS. The 0.63% Sb_SnS/CdS spectra is the VBE of SnS/CdS heterojunctions based on the 0.63% Sb sample.

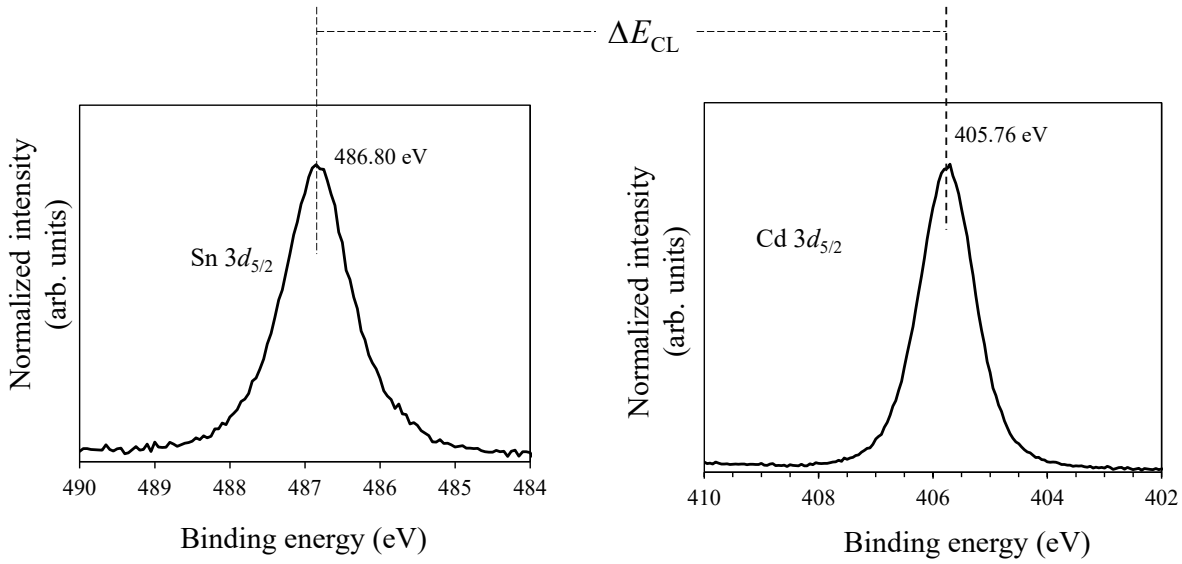

Figure 6-15 XPS spectra of Sn $3d_{5/2}$ and Cd $3d_{5/2}$ in SnS/CdS based on Sb doped SnS used to determine the CLs at the junctions.

Table 6-4 Results of band alignment measurement for vacuum and Sb doped SnS thin films.

Sample	VBE (eV)	$\Delta E^{\mathrm{SnS}}_{\mathrm{CL-SnS/CdS}}$ (eV)	VBO (eV)	CBO (eV)
V400	0.79	81.00	0.94	0.30
VA400-0.63% Sb	0.76	81.04	0.92	0.29
CdS	1.31	-	-	-

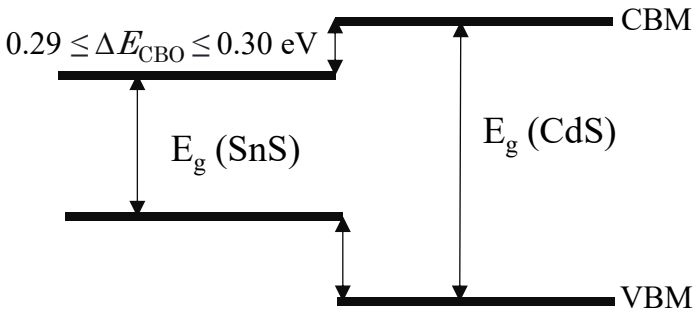

Figure 6-16 Possible band alignment diagrams of SnS thin films vacuum annealed at 400 ℃ (V400) and doped Sb at 400 ℃ (0.63% Sb).

Fig. 6-17 represents the *I-V* characteristics for different In_2O_3/CdS/SnS/Mo/SLG devices under dark and light conditions. All fabricated devices show a rectifying behavior. Under light conditions, the reduction in resistance is observed, which indicates the generation of photocarriers in all the samples. By considering the SnS/CdS junction as an ideal diode, the experimental dark current data was fitted to the eq. 6-5 above.

The reverse saturation current of 2.2×10^{-3} A is obtained for the device based on an as-grown SnS absorber. The saturation current is decreased to 1.1×10^{-3} A, 3.0×10^{-4} A, and 2.3×10^{-4} A for the Sb doped, vacuum annealed, and post-air-annealed samples, respectively. Observation of larger reverse saturation current in the as-grown and vacuum annealed samples could indicate the existence of a higher density of defects at the interface. On the other hand, the forward bias threshold voltage of the post-air-annealed sample (VA400-250) measured under dark conditions is the largest, which appears to be the best ratification. However, this is mainly due to the existence of a large cliff-shape barrier of about 0.65 eV at the SnS/CdS junction as shown in Fig. 6-13 (b) above, which will block the injected electrons with energy less than the cliff barrier height and built-in potential to flow from CdS to SnS by external forward bias under dark condition. This might result in a larger threshold voltage ($V_{threshold} = V_{b1} + V_{b2} + V_{CBO}$) for forward current to flow (Fig. 6-18). The explanation for how the electron transport in "cliff-type" under different bias voltage is shown in Fig. 6-18. Even though the rectification is improved for both the vacuum annealed and post-air-annealed

samples compared to that of the as-grown sample, no PV effect was observed. In the devices with vacuum annealed and as-grown samples, the collection of photo-generated carriers could be impeded by the large spike formed at the SnS/CdS interface in addition to the existence of high-density interface defects. In the case of post-air-annealed samples with the large cliff type discontinuity, where the formation of large built-in potential needed for the separation of photogenerated carriers is not favored, it could annihilate the photogenerated carriers. By optimizing the post-air-annealing temperatures in the range of 200 ˚C – 250 ˚C, the band discontinuity at SnS/CdS heterojunction can be tuned in the future.

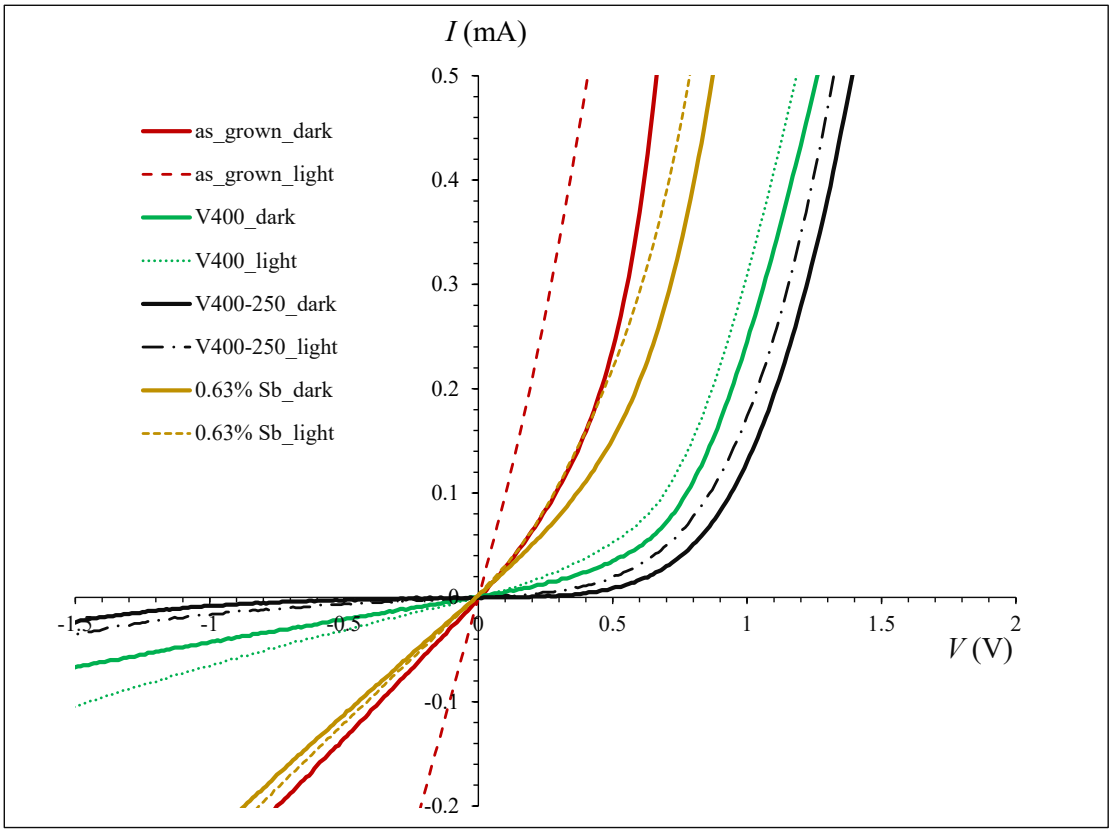

Figure 6-17 Dark/light I-V characteristics of SnS/CdS heterojunction for the as-grown, vacuum annealed at 400 ℃ (V400), post-air annealed at 250 ℃ (VA400-250), and Sb doped at 400 ℃ (0.63% Sb) SnS thin films.

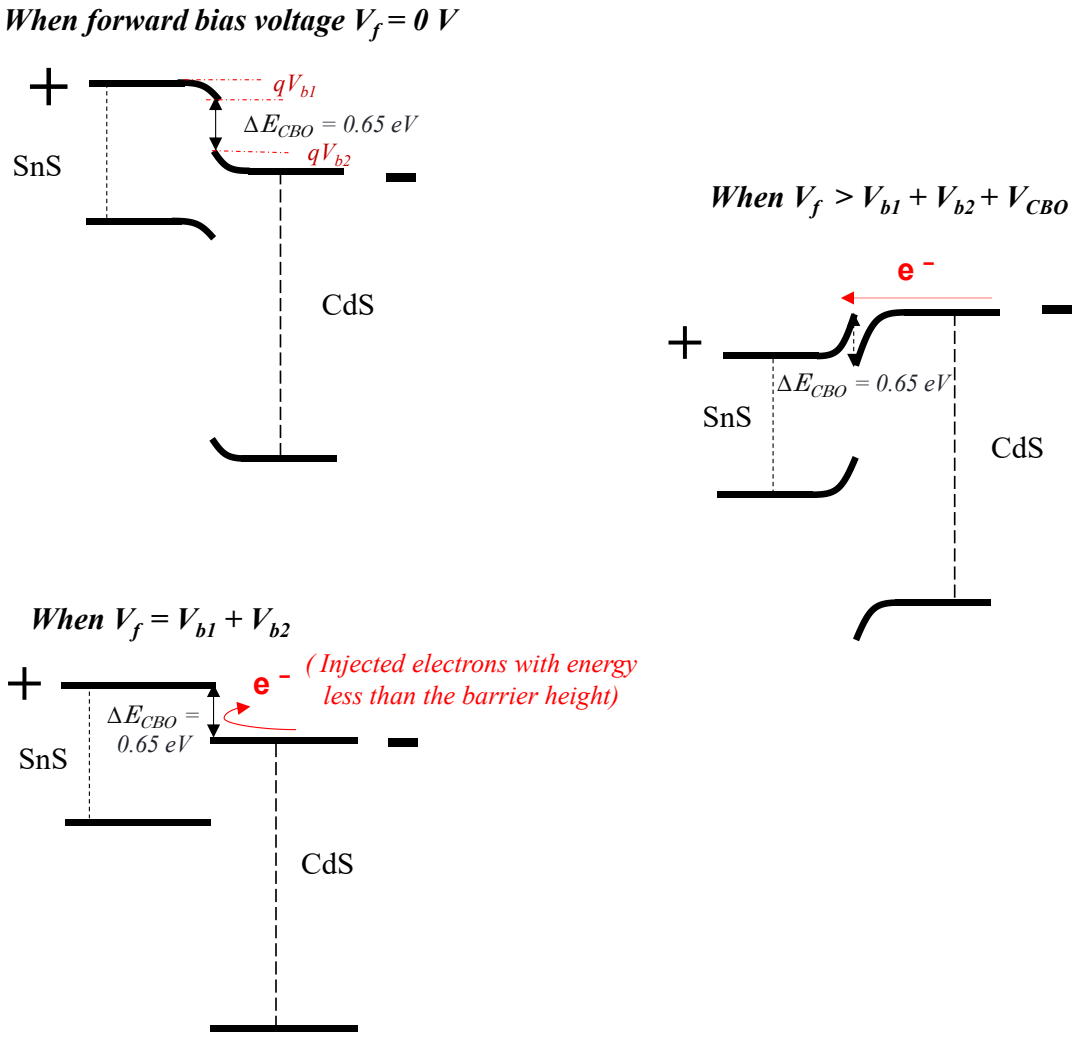

Figure 6-18 Pictorial explanation of electron transport in the "cliff-type" SnS/CdS heterojunction

Summary

The conduction band (ΔE_{CBO}) offsets values of 0.60 eV and 0.83 eV aligned in "spike-type" were obtained for the SnS/CdS and SnS/TiO_2 heterojunctions, respectively. The *I-V* characteristics of a device based on both CdS and TiO_2 buffer layers showed a rectifying behavior. A reverse saturation current of 8×10^{-3} A was obtained for the device based on SnS/TiO_2, which is two times higher than that of the device based on SnS/CdS heterojunction. The effect of vacuum annealing, post-air-annealing, and Sb doping on SnS/CdS was investigated. A "spike-type" alignment was obtained for all SnS/CdS heterojunctions based on vacuum annealed and Sb doped SnS absorber layers. A change from "spike" to "cliff" type heterojunction was observed for the post-air-annealed samples at a temperature higher than 200 ˚C. The *I-V* characteristics of SnS/CdS heterojunction diode devices exhibited a rectification behavior although no PV effect was observed due to improper band alignment.

References

1. T. J. Whittles, L. A. Burton, J.M. Skelton, A. Walsh, T. D. Veal, and V. R. Dhanak, "*Band Alignments, Valence Bands, and Core Levels in the Tin Sulfides SnS, SnS_2, and Sn_2S_3: Experiment and Theory",* Chem. Mater. **28**, 3718−3726 (2016).
2. T. Minemoto, T. Matsui, H. Takakura, Y. Hamakawa, T. Negami, Y. Hashimoto, T. Uenoyama, M. Kitagawa, *"Theoretical analysis of the effect of conduction band offset of window/CIS layers on performance of CIS solar cells using device simulation",* Sol. Energy Mater Sol., **67**, 83-88 (2001).
3. K. Ito, *Copper Zinc Tin Sulfide-Based Thin-Film Solar Cells* (Wiley, United Kingdom, 2015) 1st ed., p. 19.

Chapter 7

Introduction

This chapter summarizes the work done during this study with suggestions for further work to develop SnS thin-film solar cells into a more efficient technology.

7.1 Thesis summary

This thesis details the growth conditions, post-growth annealing, Sb doping of SnS, and the effect of SnS post-air-annealing on SnS/CdS junction properties. The effect of sulfurization temperature on the physical properties of SnS thin films was discussed at different temperatures. In addition, emphasis was also placed on promoting further recrystallization in the SnS thin films via post-annealing treatments and Sb doping.

In chapter 4, SnS thin films (~1 μm) were successfully deposited at a growth temperature of 200-400 ˚C. For sulfurization temperature at 200 ℃, unreacted Sn metal is detected by XRD, while the formation of secondary phases was detected for sulfurization temperature greater than 300 ℃. A single-phase SnS could be fabricated at a sulfurization temperature of 250 ˚C. To understand the effect of vacuum annealing on mixed and single phases of SnS thin films, the two as-grown SnS samples at 250 ˚C and 300 ˚C were annealed at different temperatures. When the as-grown SnS sample at 300 ˚C was vacuum annealed at an annealing temperature of greater than 400 ˚C, sulfur excess phases such as Sn_2S_3 and SnS_2 were decomposed single-phase SnS is obtained. All the as-grown and vacuum annealed

samples are prominently oriented along the (040) plane. The hole concentration of as-grown thin film was increased from 4.09 × 10^{15} cm^{-3} to 1.15 × 10^{18} cm^{-3}, while resistivity was decreased from 1.1 × 10^{2} Ω cm to 3.7 × 10^{1} Ω cm after it was vacuum annealed at 500 ˚C. The diminishing of the absorption edge at higher bandgap energy (1.4 eV) which belongs to the secondary phases (SnS_2, Sn_2S_3), was observed after vacuum annealing, and the bandgap converges to 1.2 eV, which belong to single-phase SnS thin film. However, no change in grain size was observed for all vacuum annealed samples. In the case of vacuum annealed single-phase SnS (as-grown SnS at 250 ˚C) at 400 ˚C, larger grains were formed for a longer annealing time for 120 min. It is observed that the grain boundaries are reduced, and the crystal grain size is noticeably improved by vacuum annealing. Very intense and sharp XRD peaks are also confirmed for vacuum-annealed samples at 400 ˚C for 120 min. The as-grown SnS thin films exhibited strong (040) preferred orientation, while the vacuum annealed samples at 400 for 120 min showed (111) preferred orientation. No secondary phases were detected for all as-grown and vacuum annealed samples. The as-grown sample's bulk and surface S/Sn ratio were 1.04 and 1.22, respectively. Elimination of sulfur-rich secondary phases was observed after vacuum annealing. The resistivity of the annealed film is decreased to 7.0 Ω cm, while the carrier density and Hall mobility is increased to 1.2 × 10^{17} cm^{-3} and 17.06 $cm^2V^{-1}s^{-1}$, respectively. The increase in mobility and decrease in resistivity could be related to the improvement of grain size and considerable reduction of grain boundaries from the SnS thin film after annealing. The Hall-effect measurement of all as-grown and annealed films showed *p*-type conductivity. However, the increase in annealing temperature to 450 ˚C added no impact on the grain size of SnS, while a deterioration in

crystallinity was observed for annealing temperature at 550 ˚C. There were no apparent changes on the crystallinity of post-air-annealed samples, while a decrease in carrier density and increase in resistivity was observed compared to that of vacuum annealed samples.

In chapter 5, the effect of Sb doping on the mixed-phase SnS (as-grown SnS at 300 ˚C) and single-phase SnS (SnS grown at 250 ˚C) were discussed. When the as-grown SnS at 300 ˚C was doped with Sb at doping temperature greater than 400 ˚C, the secondary phases such as SnS_2 and Sn_2S_3 were decomposed and a single-phase SnS was obtained. The amount of Sb diffused to the sample increases with doping temperature with a maximum value of 4.8% at 550 ˚C. The S/Sn ratio was varied between 1.28 and 1.21 with doping temperature. The highest resistivity of 5×10^5 Ω cm and a minimum carrier concentration of 7.65×10^{12} cm^{-3} were observed at 1.2% Sb. The carrier concentration was increased again upon increasing the amount of Sb up to 2.7%. The optical band gap was varied between 1.2 - 1.4 eV for the as-grown and Sb doped samples. On the other side, when the single-phase SnS (as-grown SnS at 250 ˚C) was vacuum annealed at a temperature greater than 400 ˚C, the thin films' crystallinity was improved S/Sn ratio was not altered, which remind near the stoichiometry. Under the controlled S/Sn ratio, the effect of Sb concentration on the electrical and optical properties of SnS was investigated. By doping a small amount of Sb, the film's resistivity was increased, while the carrier concentration was lowered due to the doping effect. A minimum hole concentration of 1.2×10^{14} cm^{-3} and maximum mobility of 12.75 $cm^2V^{-1}s^{-1}$ was observed at 0.55% Sb content. The optical bandgap was observed to be 1.2 eV independent of Sb content. Low-level Sb (0.55% Sb) doping under controlled S/Sn ratio was an effective way of fabricating compensated SnS. However, the conductivity type of all

grown films remained *p*-type. By further increasing the Sb concentration under a controlled S/Sn ratio, *n*-type SnS may be possible in the future.

In chapter 6, the heterojunction properties of SnS/TiO_2 and SnS/CdS were compared. The conduction band (ΔE_{CBO}) offsets values of 0.60 eV and 0.83 eV aligned in "spike-type" were obtained for the SnS/CdS and SnS/TiO_2 heterojunctions, respectively. A reverse saturation current of 8×10^{-3} A was obtained for the device based on SnS/TiO_2, which is two times higher than that of the device based on SnS/CdS heterojunction. Chapter 6 is also focused on the effect of vacuum, post-air annealing, and Sb doping on the SnS/CdS heterojunction properties. A change from "spike" to "cliff" type heterojunction was observed for the post-air-annealed samples at a temperature higher than 200 ˚C. The *I-V* characteristics of SnS/CdS heterojunction diode devices exhibited a rectification behavior, although no PV effect was observed due to improper band alignment. Our experimental results suggest that annealing at an optimal temperature under a suitable ambience could be a possible approach to achieving a proper SnS/CdS heterojunction alignment for PV applications.

7.2 Suggestions for the future works

Following the work presented in this thesis, many research challenges remain, and more investigation is required to improve further the quality and performance of SnS thin films devices. The following experiments can be further explored:

- ✓ Develop suitable surface etching for the SnS solar absorber layer to pass the surface and reduce interface and surface recombination effects in SnS solar cells.
- ✓ Further post-annealing studies in the antimony environment are needed to optimize carrier compensation and fully realize *n*-type SnS.
- ✓ Air annealing led to variation in SnS/CdS band alignment; however, further investigation should be carried out to optimize the band alignment.